

IN # 64241

NASA CR-182254



ADVANCED ELECTRIC PROPULSION RESEARCH - 1988

Prepared for
LEWIS RESEARCH CENTER
NATIONAL AERONAUTICS AND SPACE ADMINISTRATION
Grant NGR-06-002-112

Annual Report

February 1989

Paul J. Wilbur
Department of Mechanical Engineering
Colorado State University
Fort Collins, Colorado 80523

LIBRARY COPY

APR 28 1989

LANGLEY RESEARCH CENTER
LIBRARY NASA
HAMPTON, VIRGINIA

(NASA-CR-182254) ADVANCED ELECTRIC
PROPULSION RESEARCH, 1988 Annual Report, 1
Jan. 1988 - 1 Jan. 1989 (Colorado State
Univ.) 89 p

N92-70506

Unclas
29/20 0064241

Report Documentation Page

1. Report No. NASA CR-182254		2. Government Accession No.		3. Recipient's Catalog No.	
4. Title and Subtitle ADVANCED ELECTRIC PROPULSION RESEARCH - 1988				5. Report Date Feb. 1989	
				6. Performing Organization Code	
7. Author(s) Paul J. Wilbur				8. Performing Organization Report No.	
				10. Work Unit No.	
9. Performing Organization Name and Address Department of Mechanical Engineering Colorado State University Fort Collins, CO 80523				11. Contract or Grant No. NGR-06-002-112	
				13. Type of Report and Period Covered Annual Jan. 1, 1988-Jan. 1, 1989	
12. Sponsoring Agency Name and Address National Aeronautics and Space Administration Washington, D.C. 20546				14. Sponsoring Agency Code	
15. Supplementary Notes Grant Monitor - Vincent K. Rawlin, NASA Lewis Research Center Cleveland, Ohio 44135					
16. Abstract Results of an experimental study into the effects of changes in hollow cathode, anode and magnet positions on the performance of a ring cusp discharge chamber are described. A methodology that can be applied to determine the physical constraints that limit the performance of ion thrusters are limiting under various operational and design conditions is presented. Results obtained in an experimental study of high current hollow cathodes are presented. The existence of a region of high plasma potential induced by a high rate of ionization immediately downstream of hollow cathode orifices is postulated. It is pointed out that such a region could explain the high erosion rates that have been observed on surfaces downstream of hollow cathodes operating at high current levels. Experimental evidence confirming the existence of such regions is presented.					
17. Key Words (Suggested by Author(s)) Electrostatic Ion Thruster Arcjet Thruster Hollow Cathode Ion Optics				18. Distribution Statement Unclassified-Unlimited	
19. Security Classif. (of this report) Unclassified		20. Security Classif. (of this page) Unclassified		21. No of pages 84	
22. Price*					

TABLE OF CONTENTS

<u>Section</u>	<u>Page</u>
ABSTRACT.....	1
LIST OF FIGURES.....	11
CHARACTERIZATION OF HOLLOW CATHODE, RING CUSP DISCHARGE CHAMBERS.....	1
AN APPROACH TO THE PARAMETRIC DESIGN OF ION THRUSTERS.....	1
HIGH CURRENT HOLLOW CATHODE RESEARCH.....	3
INTRODUCTION.....	3
APPARATUS AND PROCEDURE.....	4
RESULTS.....	14
Plasma Properties.....	17
Retarding Potential Analyzer Data.....	22
A Theory of High Energy Ion Production.....	25
The Effects of Discharge Current on Cathode Temperature and Pressure.....	31
CONCLUSIONS.....	37
INVESTIGATION OF A HOLLOW CATHODE FAILURE.....	39
REFERENCES.....	44
APPENDICES.....	46
Appendix A: Ring Cusp/Hollow Cathode Discharge Chamber Performance Studies.....	46
Appendix B: An Approach to the Parametric Design of Ion Thrusters.....	57
Appendix C: A Fourier Series Technique for Differentiating Experimental Data.....	67
DISTRIBUTION LIST.....	80

LIST OF FIGURES

<u>Figure</u>		<u>Page</u>
1	Schematic of Test Apparatus.....	5
2	Downstream Langmuir Probe Circuit.....	9
3	Retarding Potential Analyzer.....	12
4	Discharge and Keeper Voltage Characteristics.....	15
5	Photograph of a Hollow Cathode Operating at 50 A Discharge Current.....	16
6	Effect of Discharge Current on Plasma Properties Downstream of the Orifice.....	18
7	Effect of Flowrate on Plasma Properties Downstream of the Orifice.....	20
8	Typical Plasma Properties Upstream and Downstream of a Hollow Cathode Orifice.....	21
9	Direct and Differentiated Retarding Potential Analyzer Data.....	23
10	Plasma Potential Profiles Measured Using an Emissive Probe.....	28
11	Plasma Density Profiles and Corresponding Emissive Probe Operating Limits.....	30
12	Effect of Discharge Current and Flowrate on Cathode Temperature and Interior Pressure.....	32
13	Interior Pressure Correlations.....	35
14	Failed Hollow Cathode Diagram.....	39
15	Scanning Electron Micrographs of Materials from Failed Cathode.....	41
C1	Idealized Retarding Potential Analyzer Trace.....	68
C2	Standard Fourier Series Approximation of RPA Trace with No Convergence Factor.....	74
C3	Fourier Series Approximation of RPA Trace with Lanczos Convergence Factor.....	75
C4	Fourier Series Representation of Beam Ion Energy Distribution with No Convergence Factor.....	77

<u>Figure</u>		<u>Page</u>
C5	Fourier Series Representation of Beam Ion Energy Distribution Using First Power of Lanczos Convergence Factor.....	78
C6	Fourier Series Representation of Beam Ion Energy Distribution Using the Square of the Lanczos Convergence Factor.....	79

CHARACTERIZATION OF HOLLOW CATHODE, RING CUSP DISCHARGE CHAMBERS

An experimental study into the effects of changes in such physical design parameters as hollow cathode position, anode position and ring cusp magnetic field configuration and strength on discharge chamber performance was conducted during the grant period. This work showed that 1) the rate of primary electron loss to the anode decreases as the anode is moved downstream of the ring cusp toward the screen grid, 2) the loss rate of ions to hollow cathode surfaces becomes excessive if the cathode is located upstream of a point of peak magnetic flux density on the discharge chamber centerline, and 3) the fraction of the ions produced that are lost to discharge chamber walls and ring magnet surfaces is reduced by positioning the magnet rings so the plasma density is uniform over the grid surface and adjusting their strength to a level where it is sufficient to prevent excessive ion losses by Bohm diffusion. The performance of a discharge chamber operating with a hollow cathode is the same as that operating with a filament cathode located at the position of the hollow cathode orifice provided the baseline plasma ion energy cost parameter is adjusted to reflect the operating power requirement for the hollow cathode. This work is described in a report¹ and a paper² completed during the grant period. A copy of the paper is included as Appendix A to this report.

AN APPROACH TO THE PARAMETRIC DESIGN OF ION THRUSTERS

A methodology that can be used to determine which of several physical constraints limits the output power and thrust of an ion

thruster under various design and operating conditions was developed during the grant period. The methodology was exercised to demonstrate typical limitations imposed by grid system span-to-gap ratio, intra-grid electric field, discharge chamber power per unit beam area, screen grid lifetime and accelerator grid lifetime constraints for a typical discharge chamber designed to operate at maximum thrust-to-power. The possibility of using other operational constraints, of applying the the technique to evaluate the potential payoff of design changes and of incorporating the methodology into mission analysis programs was considered. A paper³ was prepared to describe this work and it was supported in part by the grant being reported upon so a copy of the paper is included as Appendix B to this report.

HIGH CURRENT HOLLOW CATHODE RESEARCH

Verlin Friedly

INTRODUCTION

Presently, there is an interest in developing high power thrusters and high current electrodynamic tethers that utilize hollow cathodes operating at high discharge currents (> 20 A). In order to realize reliable, long term operation at such current levels it is important for a designer to understand both the phenomena associated with hollow cathode operation and the manner in which they will affect cathode operation at high current levels. If phenomenological trends associated with high current operation are not understood, then it is likely that problems such as the baffle erosion observed in some high current cathode systems^{4,5} will continue to evade prediction and correction.

In an effort to gain additional understanding of high-current hollow cathode operation, basic tests were conducted on a hollow cathode of standard design⁶ to determine its operating characteristics and the nature of the plasma created within and downstream of it as a function of discharge current (up to 60 A). Cathode internal pressure and orifice plate temperature measurements were both found to exhibit a strong dependence on discharge current. In fact the particular cathode used in these tests had not been designed for high current operation and both internal pressure and temperature reached values during testing that suggest it would have a short lifetime.

A retarding potential analyzer was used to measure ion energies downstream of the cathode orifice plate and ions with energies substantially greater than the difference between the anode and the cathode potentials were detected. Langmuir probes were used to determine the plasma properties upstream and downstream of the cathode orifice and an emissive probe was used to measure plasma potential potentials downstream of the orifice. Evidence was found that the emissive probe begins to indicate erroneous plasma potentials as it is moved close to the cathode orifice. Difficulties were encountered in making the measurements upstream of the orifice plate because of the harsh environment there and as a result plasma properties were measured only through the discharge current range up to 9 A.

APPARATUS AND PROCEDURE

The schematic diagram in Fig. 1 illustrates the test apparatus used to conduct the experiments described in this report. This apparatus was installed in a 30 cm dia by 45 cm high vacuum chamber. A 6.4 mm outside dia hollow cathode equipped with a 0.71 mm dia orifice (d_o) in a thoriated tungsten orifice plate was used for the tests. It contained an insert (low work function emitter) that was constructed from 0.03 mm thick tantalum foil rolled into a 20 mm long cylindrical shape and coated with Chemical R-500*. The copper cylindrical anode used was 1.7 mm thick, 100 mm in length and 64 mm in

* Chemical R-500 is a double carbonate (BaCO_3 , SrCO_3) mixture that has been manufactured by the J. R. Baker Chemical Co., Phillipsburg, NJ, but is no longer being made.

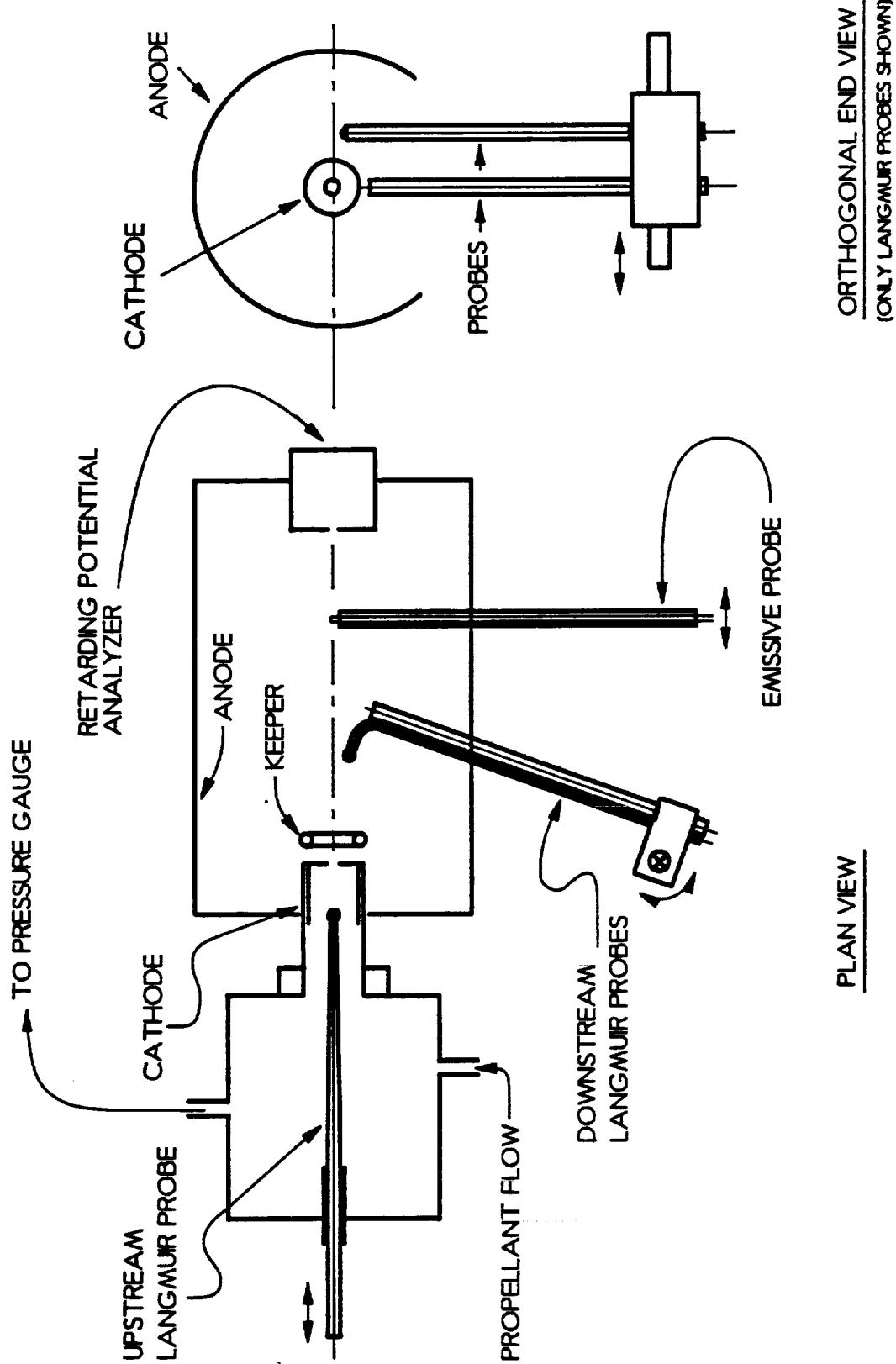


Fig. 1. Schematic of Test Apparatus

dia with a 25 mm wide slot in one side to allow for probing of the plasma within it. The anode was water cooled so it would not melt at the high discharge current levels where tests were to be conducted. A tantalum torus with a 1.5 mm minor diameter and a 5 mm major diameter was used as the keeper and it was positioned 1 mm downstream of the cathode orifice plate. The axes of the cathode, anode and keeper were all colinear. To assist in startup a resistive heater covered with a tantalum foil radiation shield was placed on the cathode at the location of the insert. The internal pressure of the cathode was measured using a capacitance gauge, accurate to within ± 1 Torr. Because these pressure measurements were made in the plenum chamber upstream of the cathode tube as suggested in Fig. 1 and because the flowrates involved were low, it is argued that the measured pressure is close to the stagnation pressure at the cathode orifice. Cathode wall temperatures were measured by viewing the interface of the orifice plate and cathode tube using a micro-optical pyrometer located outside the glass bell jar. Measurements were then corrected for surface emissivity errors and absorption losses through the glass using a calibration curve developed by making simultaneous temperature measurements on a heated tantalum surface using a thermocouple and the optical pyrometer. After the calibration had been completed, significant coating of the bell jar could have changed the calibration curve, but no evidence of a coating was seen and it is assumed the initial calibration has remained valid.

The upstream Langmuir probe shown in Fig. 1 was constructed from a 0.25 mm diameter tungsten wire that had been melted in a helium atmosphere so a 0.8 mm dia sphere formed at one of its ends. This relatively large spherical probe was used because probe data taken

upstream of the cathode involved collection of currents proportional to the ion current density in the plasma (i.e. in the potential region below floating potential) and this implies a very small current unless the probe surface is large. Attempts to collect data at higher potentials in the high density plasma within the hollow cathode were not successful because the probe either perturbed the plasma excessively or melted. It was found in fact that the probe could melt even though its potential was raised only slightly above local floating potential, if the discharge current was above about 9 A. The quartz insulator used on the probe had an outside dia of 2.2 mm and was reduced in size near the spherical collector to minimize the perturbations the probe induced in both the plasma conditions and the neutral atom flow pattern. A tantalum foil shield was placed around the quartz tube near the spherical collector to reduce the rate at which the insulator was coated by material from the insert.

The two Langmuir probes shown downstream of the orifice plate in Fig. 1 were used to collect plasma property data in this region. Two probes were required so data could be collected over the complete range of densities found there. The 0.8 mm dia spherical probe was used to take data near the orifice where the densities are on the order of 10^{13} to 10^{14} cm^{-3} . It was constructed and operated to collect data in the same manner as the probe used upstream of the orifice. The cylindrical probe shown in Fig. 1 was used to collect data further from the orifice where the densities were lower ($< 10^{13}$ cm^{-3}). The cylindrical probe utilized a 0.8 mm dia tantalum wire that protruded 0.5 mm from the end of the 2.2 mm outside dia quartz tube insulator. Figure 1 illustrates the orientation of the two downstream probes with respect to the cathode. Either probe can be positioned along a

10.4 cm radius arc that terminates at the cathode orifice. Typically the spherical probe was swept to within about 1.8 mm of the orifice plate. Attempts to move it closer resulted in sufficient blockage of the orifice so the operating conditions of the cathode were perturbed significantly. It should be noted that while one probe was being used the other probe was allowed to float so its perturbing effect on the plasma would be minimized.

The circuit used to drive the upstream Langmuir probe was the same as that used by Siegfried.⁷ Using this circuit, the probe voltage could be swept electrically from -15 V to +15 V with respect to the potential of the cathode. The circuit made it possible to sweep the probe voltage at a sufficiently rapid rate so probe contamination effects were acceptably small; the peak sweep rate was limited by the response time of the X-Y plotter used to record the data. The upstream probe was cleaned before data were collected by applying a -38 V bias to it to induce ion sputtering by cathode plasma ions.

The voltages on the two downstream probes were swept manually using the simple circuit shown in Fig. 2. A high-quality, 3 k Ω potentiometer, used with the voltage regulator shown, was required in this circuit to produce a smooth and consistent voltage ramp signal to the probe. The voltage/current traces generated were recorded on an X-Y plotter. The circuit shown in Fig. 2 can be ramped from -10 V to 30 V with respect to cathode potential. The 10 V battery shown serves to bias the circuit and probe 10 V negative of the cathode so complete Langmuir probe traces can be collected. Both circuits are powered using batteries because they represent a stable and relatively noise-free voltage source.

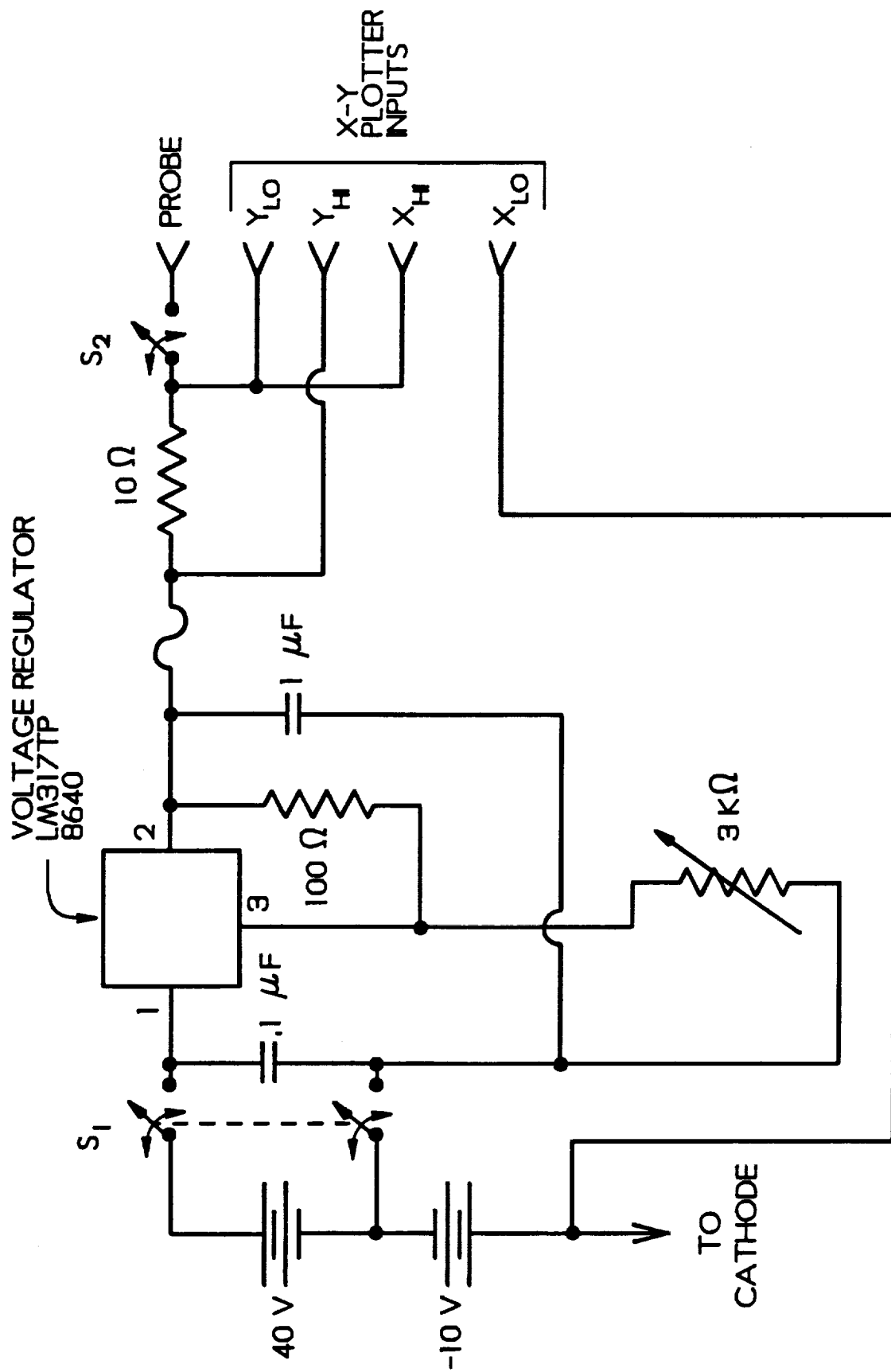


Fig. 2. Downstream Langmuir Probe Circuit

Langmuir probe data were obtained over two different potential ranges in this study (some taken over a potential range from low values to above plasma potential--complete traces--and some taken only up to about floating potential--partial traces). Different analysis techniques had to be used to analyze these different data sets. The partial traces (obtained using the spherical probes) were analyzed using the method applied by Siegfried.⁸ This method involves direct calculation of the electron temperature, determination of the plasma density from the ion saturation current and estimation of plasma potential using these results and the measured magnitude of the floating potential. Where complete traces were taken using the cylindrical probe, the method developed by Beattie⁹ was used. Both analysis techniques were applied by digitizing data that had been recorded on the X-Y plotter and then analyzing it using a routine written for an IBM-compatible personal computer.

The emissive probe shown in Fig. 1 was used to measure plasma potentials in the region downstream of the orifice plate. The active emitter surface used in this probe was a 0.08 mm dia, 6 mm long tungsten wire. This fine wire was spot welded between two 0.2 mm dia nickel wires which were insulated from the plasma and supported by a 3 mm dia alumina double-bore tube. The end of the alumina tube at which the emitter was located was covered with a castable ceramic that insulated the nickel leads from the plasma thus leaving only the tungsten wire exposed. This probe design and the circuit used to drive it are essentially the same as those used by Aston.¹⁰ The emissive probe is designed so it can be swept axially along the common centerline of the hollow cathode and anode. It is also designed so it

can be rotated off of the centerline and out of the interelectrode plasma when it is not being used to make a measurement.

The retarding potential analyzer (RPA), which is also shown in Fig. 1, is located 10 cm downstream of the hollow cathode on the cathode/anode centerline. A drawing of the RPA illustrating some of its key features is shown in Fig. 3. Because this probe must operate in a moderately high plasma density environment, special attention had to be paid to the problem of shielding the ion collector so plasma electrons could not reach it. This was accomplished by careful attention to sealing at joints so plasma/collector coupling could occur only through the two screens shown in Fig. 3. The first barrier to electron leakage into the probe is the outer body (0.25 mm thick stainless steel) and screen 1 which is connected to it. The second barrier is the inner body and the screen connected to it (screen 2). These body/screen pairs are isolated from each other using Kapton film and from the collector, which is mounted on an iso-mica plate, so these three components can be biased relative to each other. Connections to the collector and the inner body are made using, respectively, the center and outer conductors of a coaxial cable. Careful attention was paid to obtain a tight fit at the point of cable entry into the device so plasma contact with either point of cable connection or with the collector would be prevented. The electromesh nickel screens used to cover the orifices in front of the collector have an 85% optical open area and square openings 0.24 mm on a side. Visual examination of the screens showed that they are not aligned and as a result, the ion current impinges on both screens. They are held planar on 0.25 mm thick stainless steel support plates so uniform, axial electric fields can be maintained throughout the probe aperture

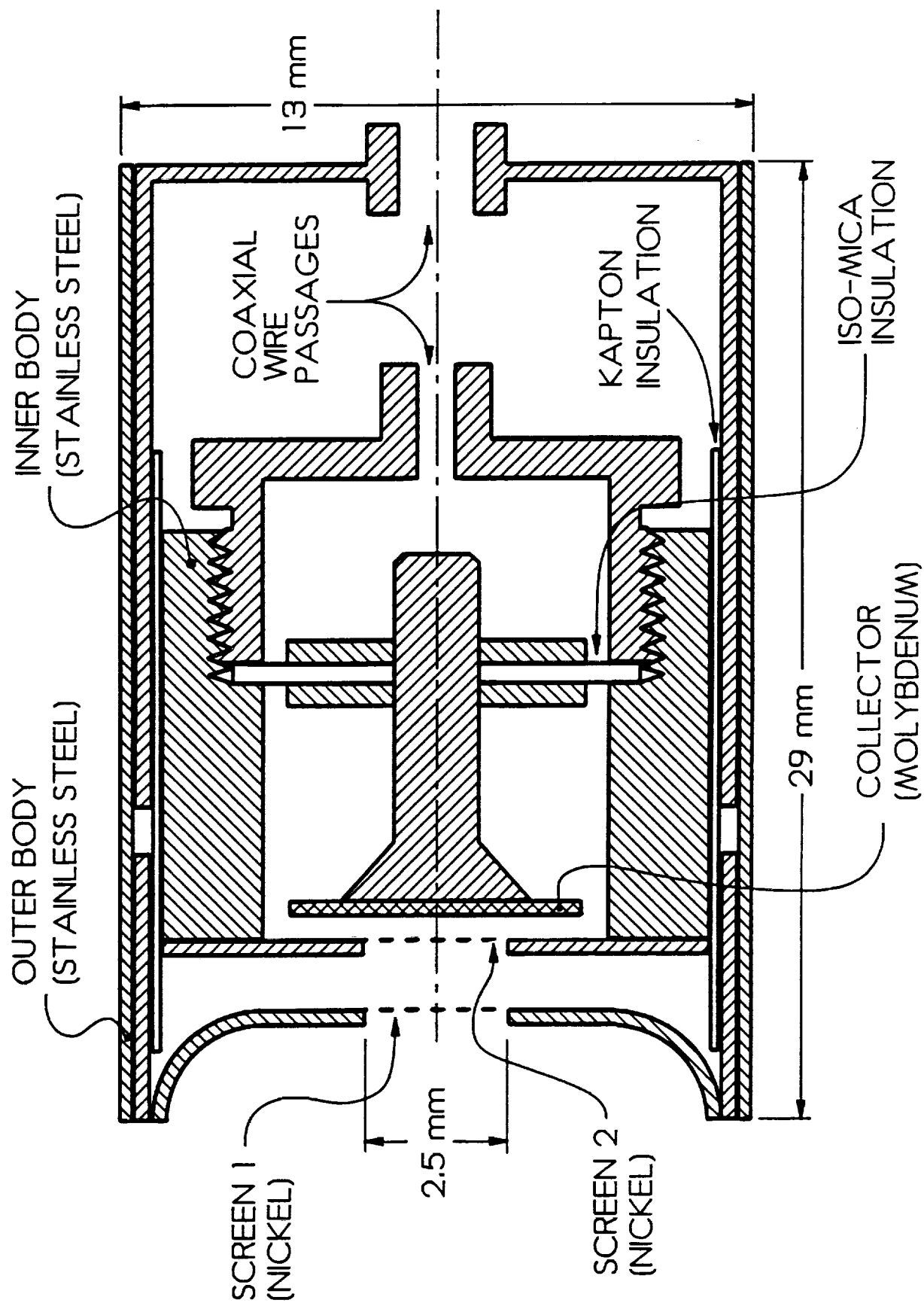


Fig. 3. Retarding Potential Analyzer

region. The voltages applied to screen 1, screen 2 and the collector were measured and designated respectively V_{s1} , V_{s2} and V_C . The current to the collector (J_C) was also recorded. Experiments were usually conducted with screen 1 floating (at about -3 V relative to the cathode), screen 2 biased sufficiently negative to repel electrons (at about -33 V (again relative to the cathode) while the collector potential was ramped from a few tens of volts below hollow cathode potential to a few tens of volts above it while corresponding collector current (J_C) and voltage (V_C) data were recorded with an X-Y plotter. Once these data had been recorded, the current/voltage curves were fitted using a Fourier series and this series was then differentiated to determine the energy distribution of the ions falling on the probe. The curve fitting and differentiating procedure used to do this work was developed by Anderson¹¹ and is described in Appendix C.

The circuit used to operate the hollow cathode included two 35 A, 60 V power supplies connected in parallel with each other so they would have the high amperage capability required. These high quality, transistorized power supplies were selected for this application because they operate stably when they are driving a plasma discharge (noisy) load. The 2 A, 160 V keeper power supply has a sufficiently high output voltage so the keeper discharge can be initiated easily. The heater power supply was capable of supplying up to 10 A. All potentials were measured with respect to cathode potential and the cathode itself was allowed to float with respect to earth ground.

Tests were conducted by first evacuating the vacuum chamber to $\sim 7 \times 10^{-5}$ Torr. The cathode was then heated with the resistive heater for 30 minutes before 160 V was applied between the keeper and cathode

and xenon gas was supplied through the cathode at a rate that ranged as high as 12 sccm but was generally ~5 sccm for a brief time to initiate the keeper discharge. Once the discharge had started the flow was reduced and the anode power supply voltage was increased until a discharge (anode) current of ~3 A was established. The keeper supply would then be reduced to ~0.5 A and the heater would be turned off. The discharge was allowed to stabilize for ~1 hr before tests were conducted. During typical tests, the bell jar (ambient) pressure was of order 1×10^{-3} Torr. This pressure is probably somewhat higher than typical ion thruster discharge chamber pressures, but may be close to values observed in the keeper discharge region of a cathode that employs a baffle.

RESULTS

Typical test measurements showing the effects of hollow cathode discharge current (J_D ranging to ~60 A) on discharge (anode) and keeper voltages (V_D and V_K) at two different cathode flowrates (\dot{m}_g) and a constant keeper current (J_K) of 0.5 A are given in Fig. 4. At both flowrates the trend of decreasing voltages with increasing discharge current up to about 20 A and slight increases in the voltages with current beyond that are observed. Voltages are observed to be slightly lower at the higher flowrate with keeper and discharge voltages being about 6 V and 12 V, respectively, at discharge current levels beyond about 20 A.

At high discharge current levels, a very intense, luminous plasma jet extending from the cathode and curving upward until it contacted the anode was observed. Figure 5 is a photograph of such a jet. This

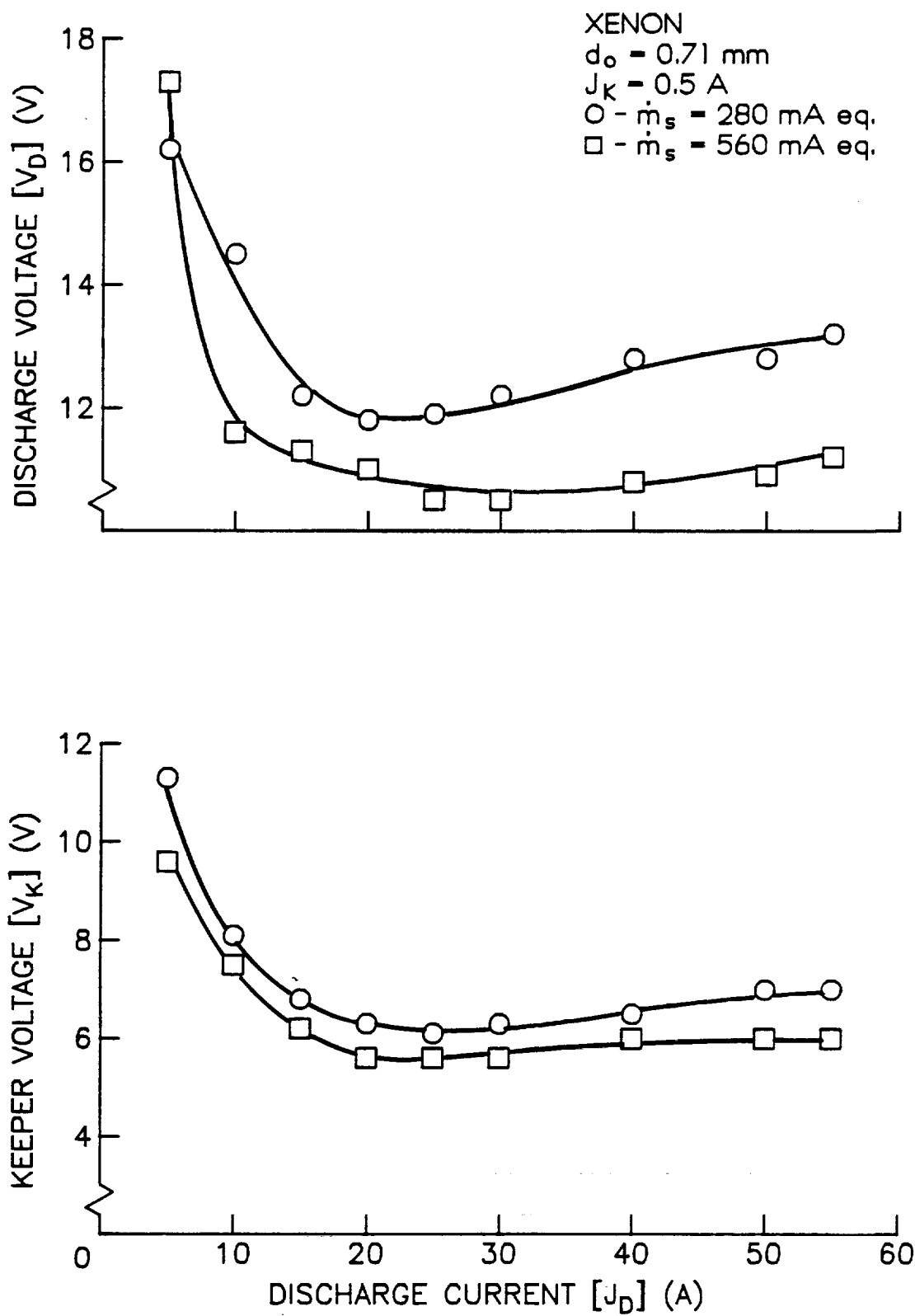


Fig. 4. Discharge and Keeper Voltage Characteristics

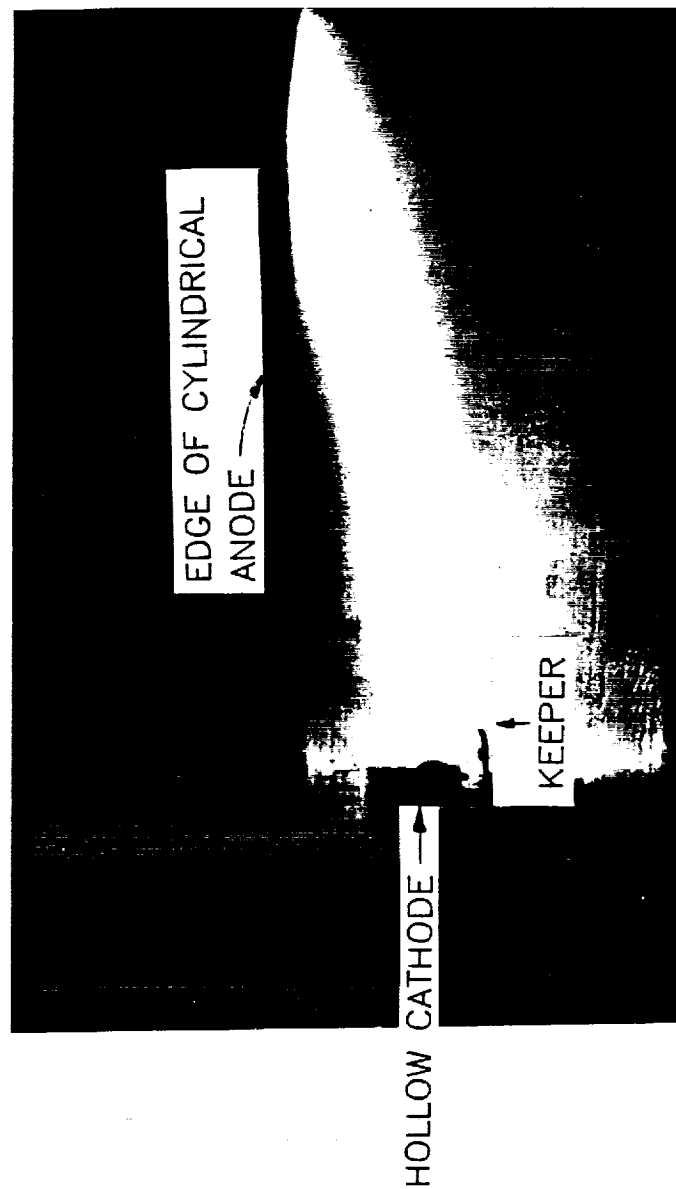


Fig. 5. Photograph of a Hollow Cathode Operating at 50 A Discharge Current

particular jet, observed when the hollow cathode was operating at ~50 A discharge current and ~20 V discharge voltage with a mass flowrate of ~320 mA eq. extended about 8 cm downstream of the cathode and was ~6 mm in diameter. Jets like the one in Fig. 5 are most apparent at high current levels, but they can also be seen at lower currents. For example, the jet observed at a 20 A discharge current was less intense, was ~4 cm long and did not exhibit the curvature seen in the jet for the 50 A case (Fig. 5).

Plasma Properties

Typical plasma property profiles measured downstream of the orifice plate along the cathode/anode centerline using a Langmuir probe are shown in Fig. 6. The discharge currents in this figure cover the range over which the jet shown in Fig. 5 was readily visible (40 A) and not apparent (10 A). The upper set of plots in Fig. 6 shows that plasma potentials, which are typically several volts below anode potential, generally decrease with axial distance from the orifice plate and that the general level of the plasma potentials increases with discharge current. The fact that plasma potentials are highest near the cathode orifice plate, especially at the higher currents, is particularly noteworthy and it will be discussed later in this report after additional data have been considered.

The axial, centerline profiles of Maxwellian electron temperature and density, which are also shown in Fig. 6, indicate that the general temperature and density levels increase with discharge current. The temperature is axially uniform over the axial range shown, however, while the density decreases rapidly with axial distance from the cathode. The observed increases in temperature and density with discharge current are considered to be due to the increased rate of

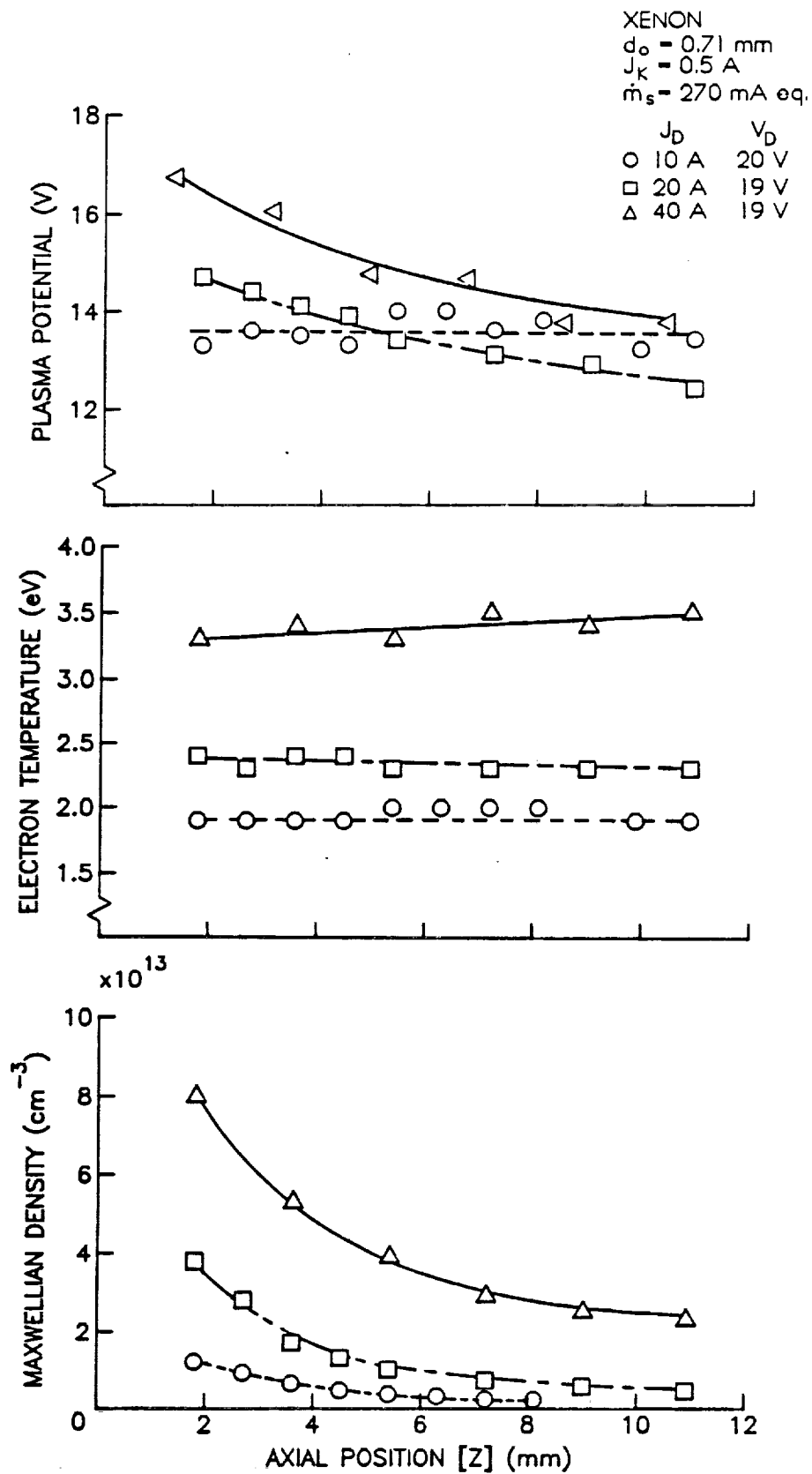


Fig. 6. Effect of Discharge Current on Plasma Properties Downstream of the Orifice

ionization that accompanies increased current flow. Primary electrons were also detected in the Langmuir probe data collected downstream of the cathode orifice but the associated densities were typically only a few percent of the Maxwellian densities. As a result it was difficult to distinguish them and quantify their properties, especially when data were being collected close to the cathode and probe traces only extended only to floating potential.

The effects of cathode flowrate on axial plasma property profiles at a discharge current of 20 A are shown in Fig. 7. These data indicate that plasma potential and electron temperature are relatively insensitive to flowrate over the range tested, but plasma densities are higher at the higher flowrate especially near the cathode orifice plate. As the legend suggests, this relative insensitivity of the plasma potential and temperature to changes in flowrate occurred under conditions where the discharge voltage changed by 5 V.

Making Langmuir probe measurements in the region upstream of the orifice plate became increasingly difficult as discharge current was increased because the plasma environment there became increasingly hostile (cathode interior plasma densities and temperatures increased). It was possible to collect data both upstream and downstream of the cathode orifice when the discharge currents were kept below 9 A and such data are shown in Fig. 8. Negative axial positions in these plots represent positions upstream of the orifice plate. These data show the plasma potential upstream of the orifice increases to a maximum value of -6 V near the orifice and then there is a -7 V voltage rise across the orifice to a 13 V plasma potential downstream of it. They also show the electron temperature increases as the orifice is approached from the upstream side and that there is

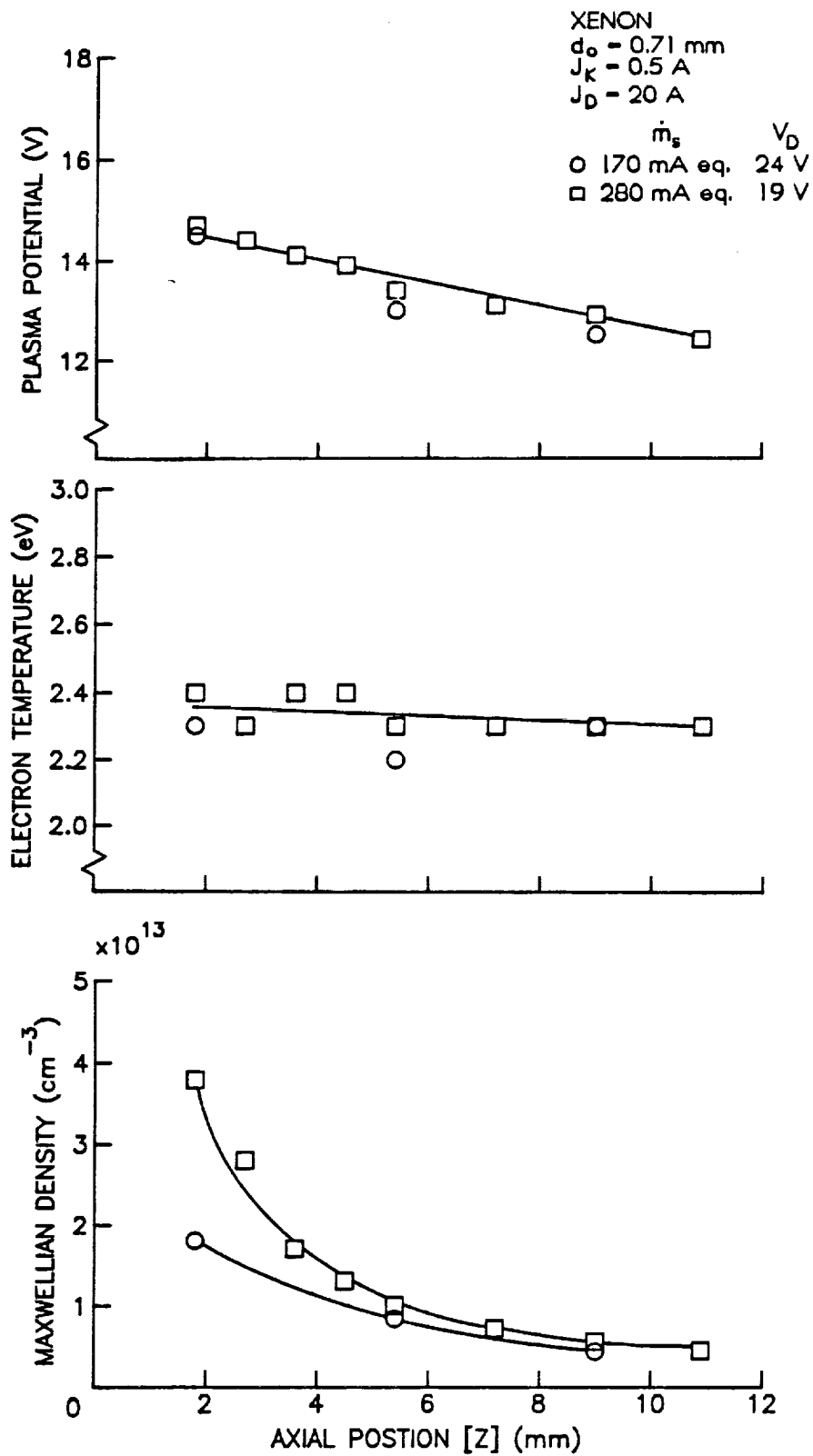


Fig. 7. Effect of Flowrate on Plasma Properties Downstream of the Orifice

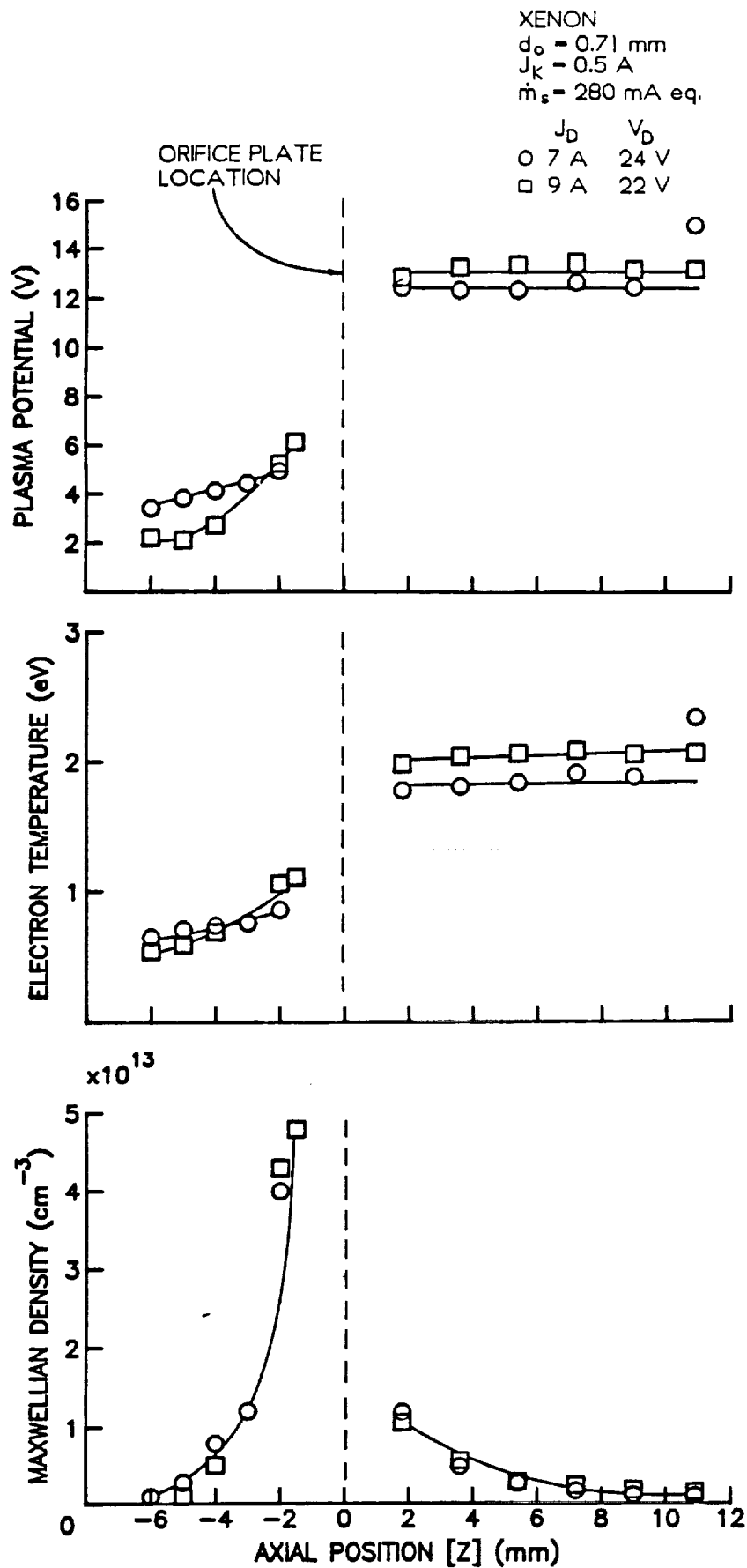


Fig. 8. Typical Plasma Properties Upstream and Downstream of a Hollow Cathode Orifice

an increase in temperature across the orifice. The most dramatic property change is seen to occur in Maxwellian electron density which rises to a very high level just upstream of the orifice and then drops through the orifice. Because the difference in the two discharge current levels for which data were collected is small, it is difficult to see significant changes in plasma properties induced by changes in discharge current.

Retarding Potential Analyzer Data

Rapid erosion of the baffles and other cathode potential surfaces downstream of hollow cathodes operating at high discharge currents has been observed by Rawlin⁴ and by Brophy and Garner.⁵ These examples of erosion are believed to have been caused by ion bombardment-induced sputtering but a source of ions with the energy needed to cause such damage is not apparent. Specifically, ions produced in the plasma downstream of a hollow cathode could acquire a kinetic energy equal to the plasma-to-baffle potential difference (about 20 V) as they approach the baffle. Ions (including doubly charged ones) falling through this potential difference would not be expected to induce sufficient sputtering to cause the observed erosion rates. Because it was considered likely that the ions had a higher kinetic energy than that associated with acceleration through the anode-to-baffle potential difference, evidence of higher energy ions was sought using the retarding potential analyzer (RPA).

Figure 9 presents typical RPA traces measured at discharge currents of 10 and 15 A using an analyzer located 10 cm downstream of the cathode orifice on the cathode centerline and sighted on the orifice. The upper plot in Fig. 9 shows the actual ion current collected as a function of collector potential measured relative to

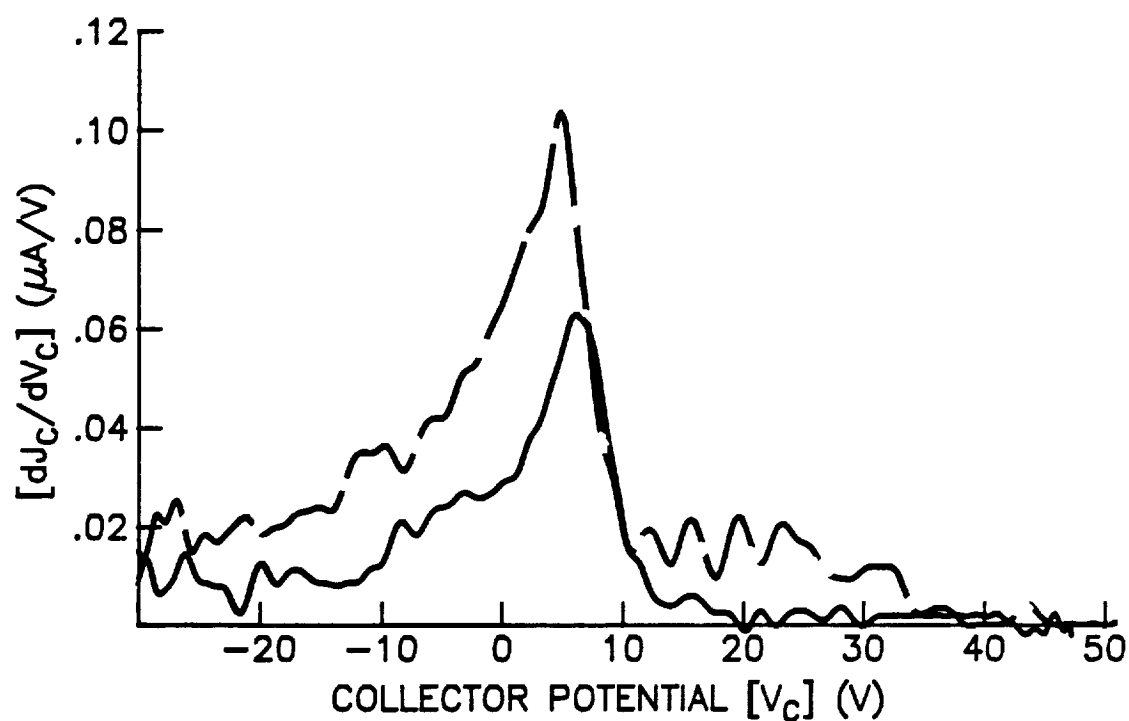
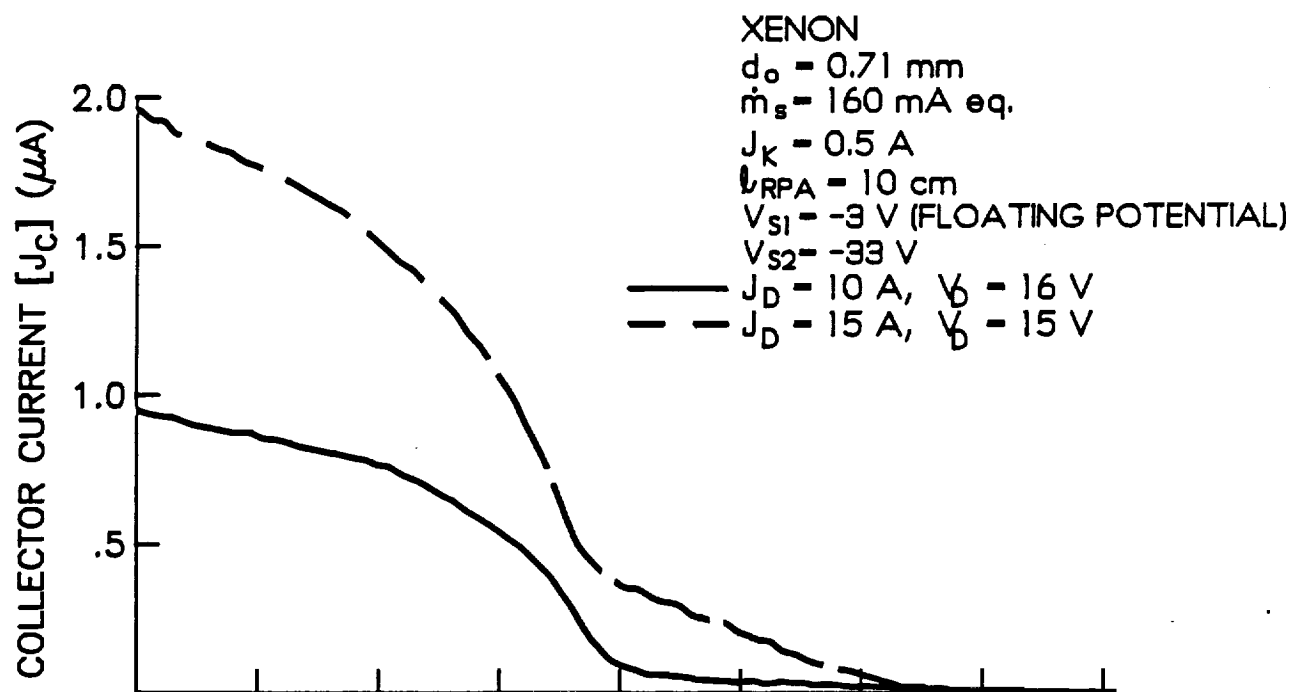


Fig. 9. Direct and Differentiated Retarding Potential Analyzer Data

cathode potential. The lower plot displays the corresponding derivatives of the collector currents with respect to collector potential determined using the procedure described in Appendix C. The data shown in these lower plots are proportional to the distribution functions of the ions incident on the RPA. The numbers on the horizontal axis are numerically equal to the energies (in eV) that singly-charged ions striking a cathode potential surface would have. Doubly-charged ions would have energies equal to twice the indicated horizontal axis voltages. Singly and doubly-charged ions cannot be distinguished from RPA data, however, so the relative current densities of these two species are not indicated. In light of these facts, the figure suggests that most singly-charged ions striking a cathode potential surface such as a baffle would have energies near 5 or 6 eV and doubly-charged ones would have twice this energy at both the 10 A and 15 A discharge current operating conditions. At the 10 A operating condition the solid line data indicate very few singly-charged ions would have energies beyond 10 or 12 eV. At the 15 A operating condition, on the other hand, the broken curve in the lower plot of Fig. 9 suggests significant numbers of singly-charged ions with energies ranging to 35 eV (and/or 70 eV doubly-charged ions) could be expected to bombard a cathode potential surface such as a baffle. This preliminary result is considered particularly significant because it represents the first direct evidence that increasing numbers of high energy ions are generated by a hollow cathode discharge as discharge current is increased and that the energy of these ions can exceed the energy associated with the plasma-to-cathode potential difference (approximately the 15 volt anode-to-cathode potential difference in the 15 A discharge current case).

It should be noted that there are irregularities associated with the data presented in Fig. 9. Specifically, the data in the lower plots show a substantial non-zero derivative at collector potentials below zero. This result implies significant numbers of ions with negative kinetic energies are present in the plasma and this is a physical impossibility. It indicates that the RPA is not operating properly as it is presently configured even at the relatively low discharge current levels where the data of Fig. 9 were obtained. The design deficiencies appear to be due to either small electron currents that reach the collector or nonuniform electric fields that develop in the vicinities of the screens and the collector. While the probe appears to be working properly at positive collector potentials (the ion energy range of interest), more work is needed to improve its design and performance and to extend its useful range of operation to higher cathode discharge current levels.

A Theory of High Energy Ion Production

The ion current data of Fig. 9 and the evidence of rapid baffle erosion observed at high hollow cathode current levels both suggest the existence of a population of ions with energies and current densities that increase with cathode current. It is not obvious, however, how such ions could be created in plasma environment where the maximum potentials measured in the plasma and on the anode are about 15 V. It would be expected that ions created in this environment would achieve a maximum kinetic energy of 15 eV as they were accelerated to a cathode potential surface. Higher ion kinetic energies could develop only if the ions were created at a location where the plasma potential was substantially greater than the discharge voltage. Langmuir has pointed out that this condition can

develop when high energy electrons are injected into neutral gas¹² and such a region of high potential was observed to develop immediately downstream of a hollow cathode emitting electrons in a hollow cathode plasma contactor experiment by Williams.¹³ The potential hill observed by Williams was measured at a low emission current (< 1 A) but the fact that it was observed at all demonstrates that potentials above anode potential can and do develop immediately downstream of a hollow cathode.

The physical mechanisms by which a region of high potential could develop can be understood by considering a jet of electrons being ejected out of a hollow cathode orifice through a plume of relatively high density neutral gas also coming through the orifice. It is postulated that electrons are accelerated to substantial kinetic energies as they pass through a double sheath¹² located at the downstream edge of the hollow cathode orifice. The data of Figs. 6 and 8 suggest a substantial potential difference that could sustain a double sheath does develop across the orifice plate. Electrons accelerated through such a double sheath would be likely to ionize some of the neutral gas through which they were passing. If one presumes the electrons had kinetic energies significantly in excess of the ionization energy of the gas atoms, then the secondary and primary electrons coming out of the ionization event would also tend to have substantial kinetic energies. These electrons would therefore tend to escape from the region rapidly, leaving behind the less-mobile ions that were a product of the ionization. The net result of this sequence of events would be the accumulation of net positive charge which would induce the increase in plasma potential (i.e. the potential hill) observed by Williams just downstream of the cathode

orifice. This potential hill in turn provides the mechanism whereby forces could be exerted that would accelerate the ions out of the ionization region (to the high energies observed using the RPA) and retard the electron loss rate by a plasma seeking to maintain charge neutrality.

In order to determine if the potential hill suggested by the preceeding argument was present, the emissive probe was used to measure plasma potential profiles along the downstream centerline of a hollow cathode operating at various, high discharge currents.

Figure 10 shows plots of plasma potential as a function of axial position measured at three different discharge current levels in these tests. For a discharge current (J_D) of 3 A, the discharge voltage (V_D) is 22 V but the data indicate the plasma potential reaches only a -16 V peak at a location about 5 cm downstream of the orifice.

Although this peak potential does not surpass the discharge voltage, it does indicate a potential hill can develop just downstream of the cathode. The emissive probe data of Fig. 10 show, however, that the potential hill disappears when the discharge current is increased to 10 A and that a potential depression develops at 20 A. The Langmuir probe data presented previously (Figs. 6, 7 and 8) had shown just the opposite trends (the development of a potential hill that became more substantial as discharge current was increased) so both sets of data were called into question.

In an effort to resolve differences between various measurements it should be recalled that there is a very intense plasma discharge (high plasma density) close to the cathode orifice and because of this, only the ion saturation portions of the Langmuir probe characteristics can be collected there. Analysis of such data

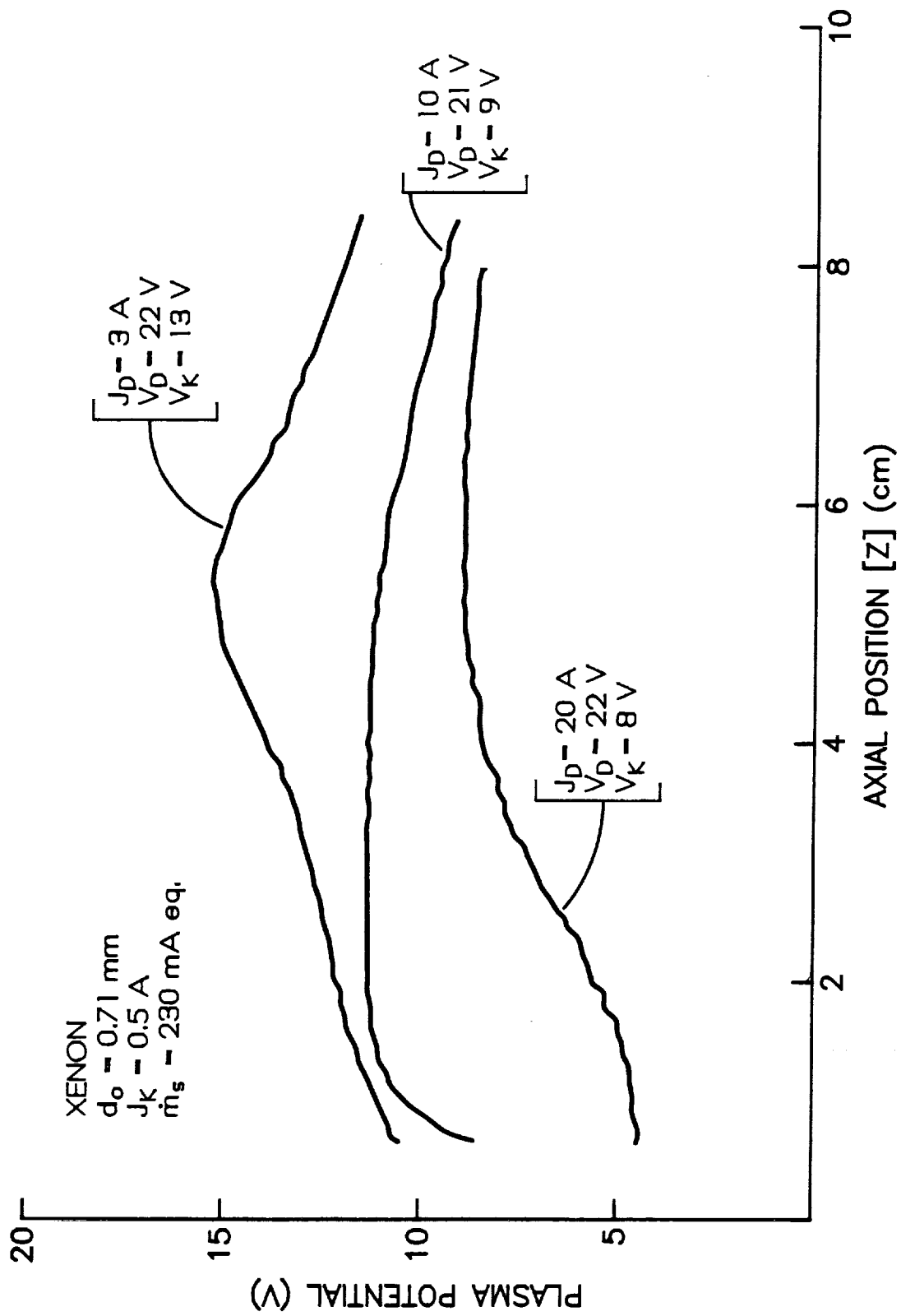


Fig. 10. Plasma Potential Profiles Measured Using an Emissive Probe

probably yields plasma potentials like those shown in Figs. 6 through 8 that are accurate to within $\pm 20\%$ but no better. The emissive probe data are, however, subject to a more pervasive error in the high plasma density environment close to the cathode. This error is associated with the fact that the emissive probe filament must be at a sufficiently high temperature so electrons can be emitted thermionically from it at a rate equal to the arrival rate of random thermal electrons from the plasma. If the filament is not hot enough to satisfy this condition, then the probe will float below the prevailing plasma potential and since it is this floating potential that is measured, the probe will indicate a plasma potential that drops progressively further below the true value as plasma density is increased. The currents emitted (J_e) and collected (J_c) by a probe are described by the equations:

$$J_e = A \epsilon(T) \quad (1)$$

and

$$J_c = \frac{1}{4} e n_e A \sqrt{\frac{8kT_e}{\pi m_e}} \quad (2)$$

where A is the area of the probe filament wire exposed to the plasma, $\epsilon(T)$ is the temperature-dependent electron emission current density of the probe (A/m^2)¹⁶, e is the electronic charge, n_e is the density of plasma in which the probe is located, T_e is the electron temperature and m_e is the electron mass. Applying the requirement for accurate probe operation ($J_e \geq J_c$), limiting plasma densities can be computed as a function of emissive probe temperature by equating Eqs. 1 and 2. Figure 11 shows two values of these limiting densities pertaining to

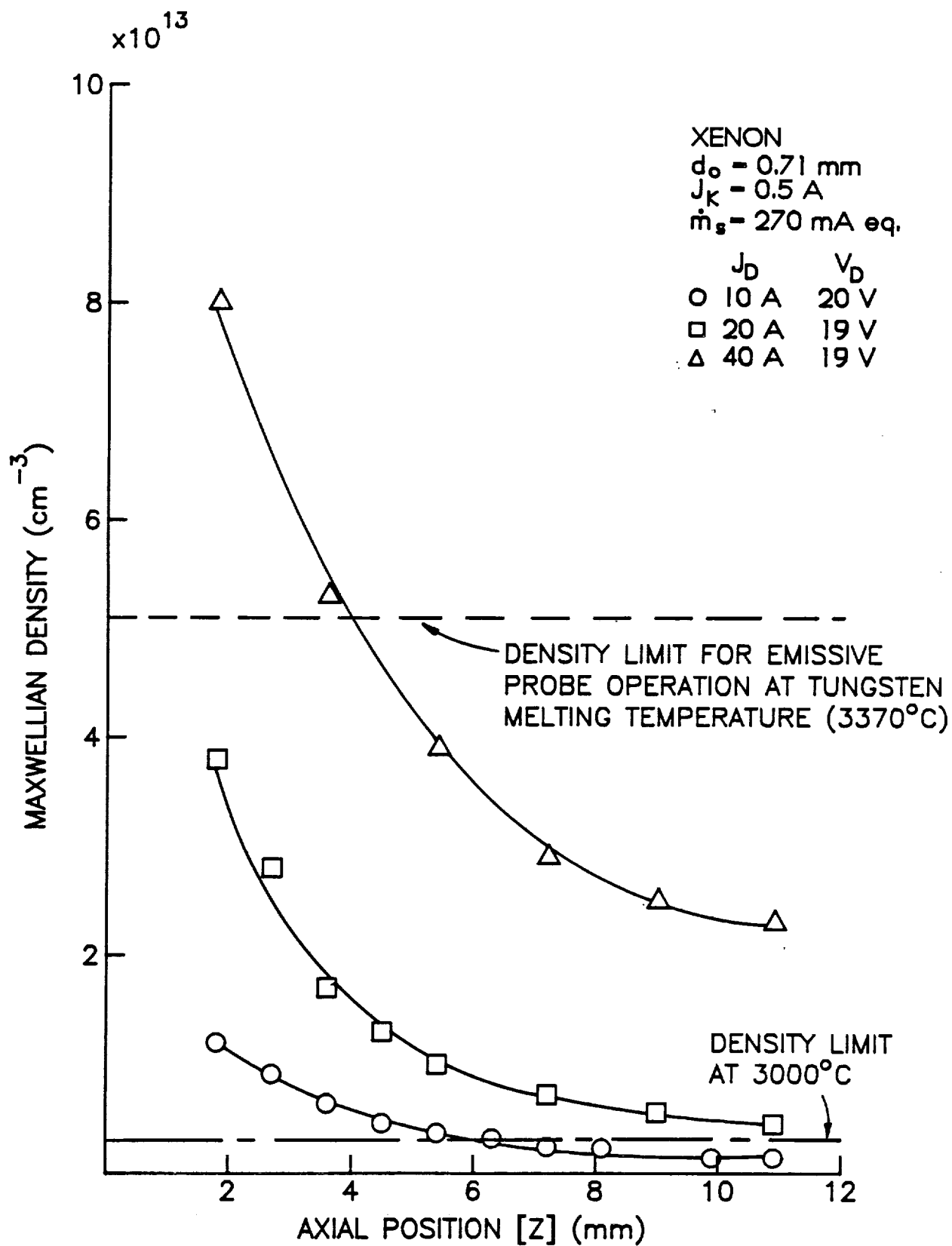


Fig. 11. Plasma Density Profiles and Corresponding Emissive Probe Operating Limits

the maximum temperature at which the ultimate tungsten probe could be operated (3370 °C-its melting temperature) and the maximum temperature at which the present probe can be operated without burning out (estimated to be ~3000 °C). Also plotted in this figure are axial plasma density profiles determined from Langmuir probe measurements (from Fig. 6). It is apparent from the data of Fig. 11 that an emissive probe will indicate plasma potentials that fall progressively further below the true values as the probe is moved closer to the cathode into the progressively higher density plasmas located there. Thus, it may be concluded the plasma potential profiles shown in Fig. 10 are in error. They should probably show a potential peak developing within a centimeter of the cathode as the Langmuir probe data do, but they do not because the probe cannot be maintained at a sufficiently high temperature to indicate properly in the high density plasma that exists there. Further, the departure between these true and measured plasma potentials increases as cathode discharge current is increased.

The Effects of Discharge Current on Cathode Temperature and Pressure

As the discharge current associated with the typical cathode used to obtain the data for Fig. 7 is increased both the temperature of the cathode wall and the cathode interior pressure increase in the manner shown in Fig. 12. As the data in the upper plot indicate, the cathode wall temperature dependence on flowrate is small. The magnitudes of the temperatures shown at discharge currents above about 10 A are considered excessive because they would induce rapid, low work-function material migration from the insert. This would be expected to result in turn, in relatively rapid degradation of the insert and a short cathode lifetime. It is noted, however, that these temperatures

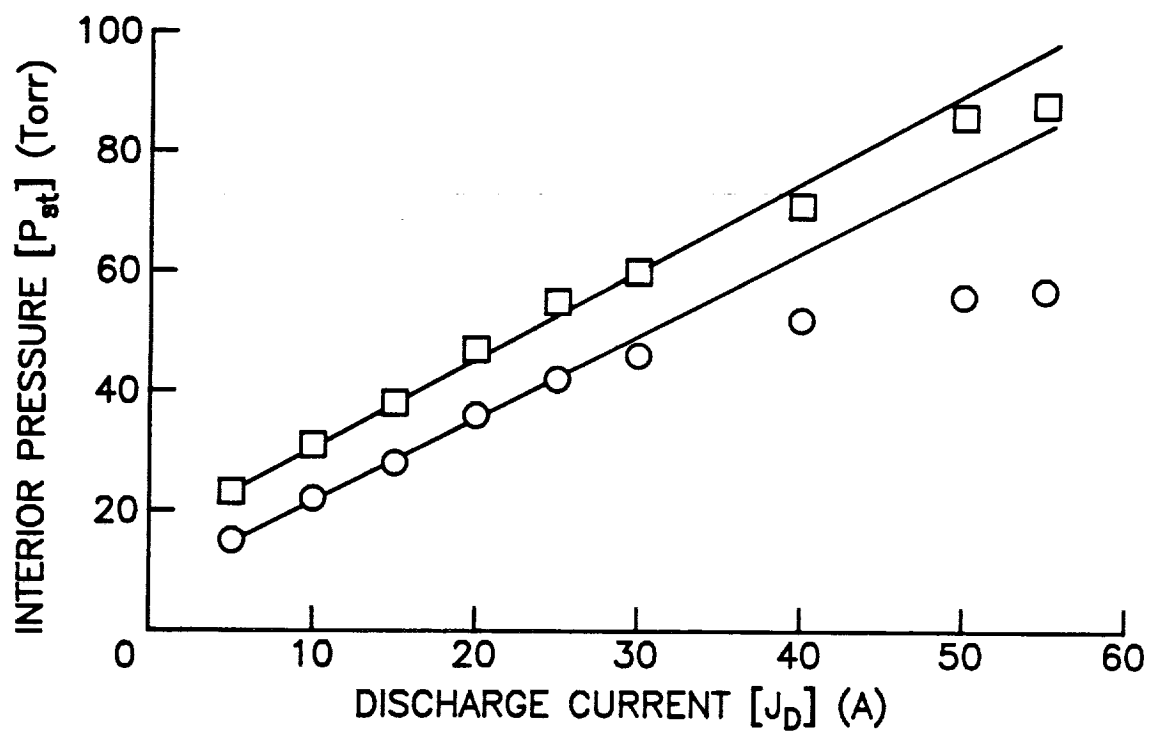
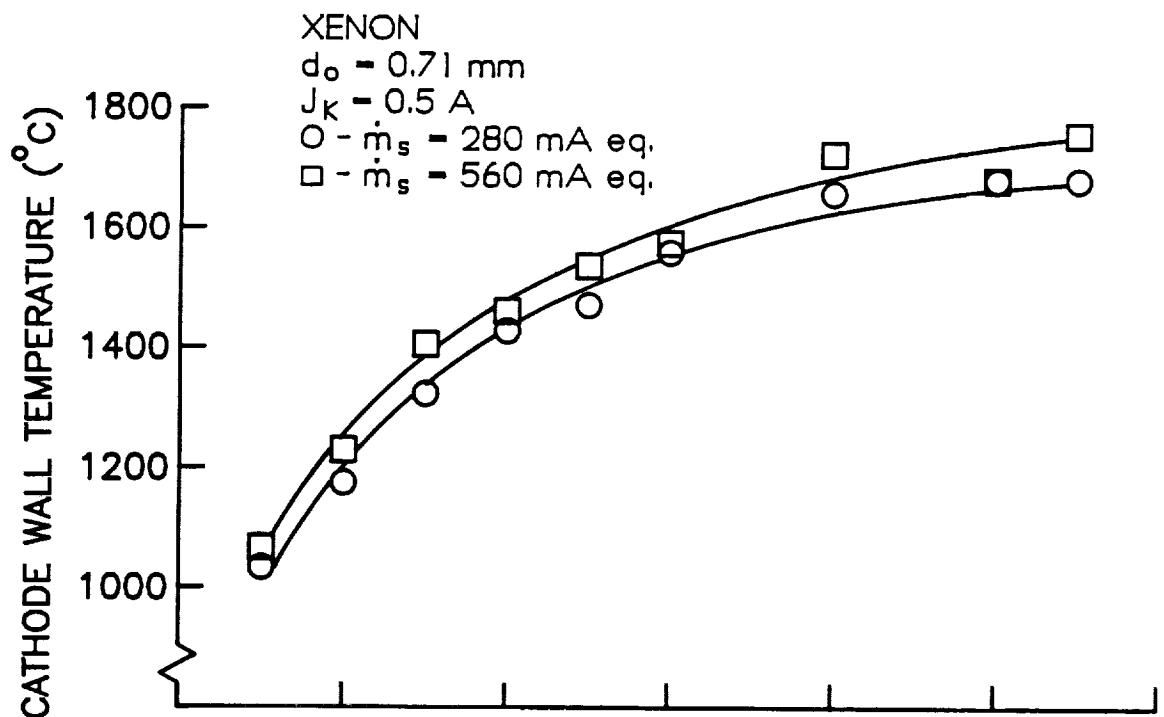


Fig. 12. Effect of Discharge Current and Flowrate on Cathode Temperature and Interior Pressure

could be reduced by redesigning the cathode to enhance radiative and conductive heat transfer from the electron emission zone where much of the heat is deposited.

The cathode interior pressure was expected to increase in direct proportion with discharge current, as the straight lines in the lower graph in Fig. 12 suggest. At low current levels (< 30 A) this variation was observed at both flowrates for which data are shown in this figure, but at higher currents for $\dot{m}_s = 280$ mA eq. the pressure showed less than a linear increase. This departure from linearity is believed to be caused by propellant leakage from the cathode or cathode plenum into the vacuum bell jar through an opening other than the orifice. This leakage problem is one that is still being addressed.

The data of the lower plot of Fig. 12 are striking because they suggest that pressures within this particular cathode, which has not been designed specifically for high current operation, approach 100 Torr at high currents. The calculated length over which electron emission would occur on an insert in a cathode operating at such pressures would only be a few tenths of a millimeter.¹⁴ Such a small emission region length would be expected to result in a high emission region temperature and consequentially rapid degradation of the insert.

In order to apply a model describing the processes occurring within a hollow cathode¹⁴ one must be able to relate the cathode interior pressure to the cathode flowrate and orifice diameter. The basic equation that should relate these quantities is:

$$P_{st} = \frac{C \dot{m} \sqrt{T_{ni}}}{d_o^2} \quad (3)$$

where \dot{m} is the propellant flowrate through the cathode, d_o is the orifice diameter, T_{ni} is the temperature of the neutral atoms inside the cathode and C is a constant that is determined by the extent to which the flow is free molecular or continuum. If one treats the neutral atom temperature as relatively constant, this equation suggests the cathode interior pressure could be normalized to account for the effects of flowrate and orifice diameter using the parameter $P_{st} d_o^2 / \dot{m}_s$. In this expression, P_{st} would represent the cathode interior stagnation pressure and \dot{m}_s the rate at which propellant is being supplied through the cathode. When this correlating parameter is applied to the data of Fig. 12, the correlations shown in the upper plot of Fig. 13 are obtained. If this were a good pressure/flowrate correlating parameter, all of the data would be scattered about a common line and if it also correctly reflected the effects of discharge current on the flow of fluid through the orifice, the line would be horizontal. In this case the data do not correlate particularly well in either sense.

It must also be recognized, however, that the suggestion made earlier that there is a double sheath located at the cathode orifice implies that there is ion backflow through the cathode orifice. While one might expect this back flowrate to be small its effect could be taken into account by applying the equation for the total atom flowrate through the orifice:

$$\dot{m}_T = \dot{m}_s + \dot{m}_i \quad (4)$$

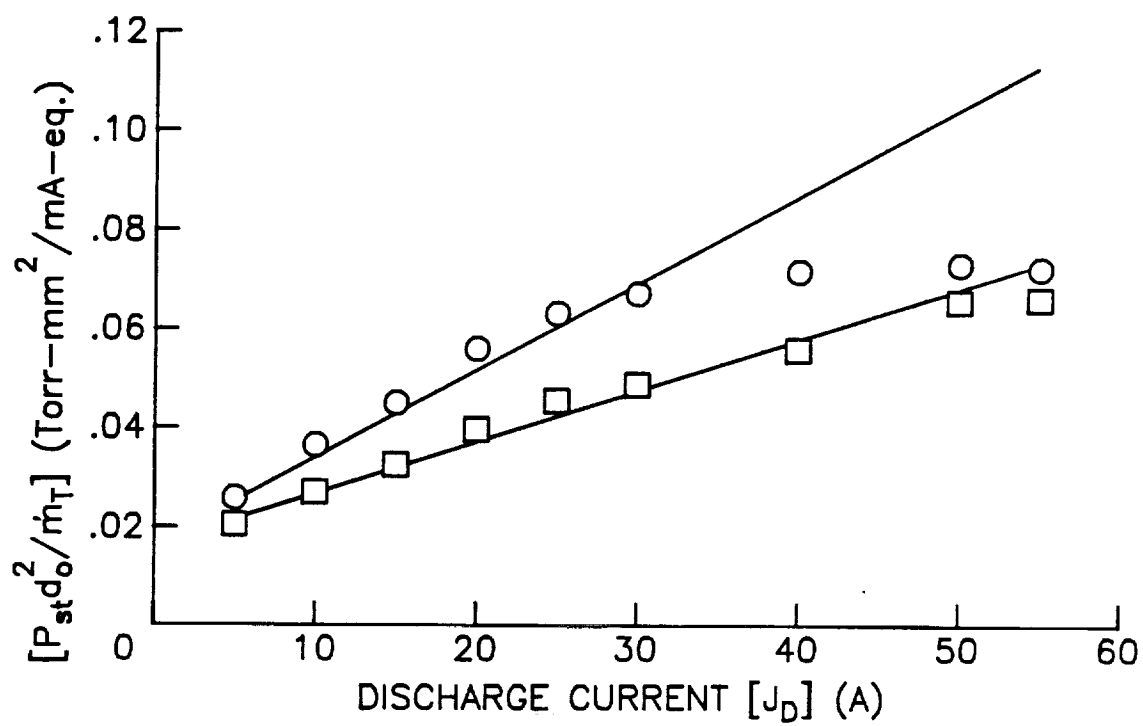
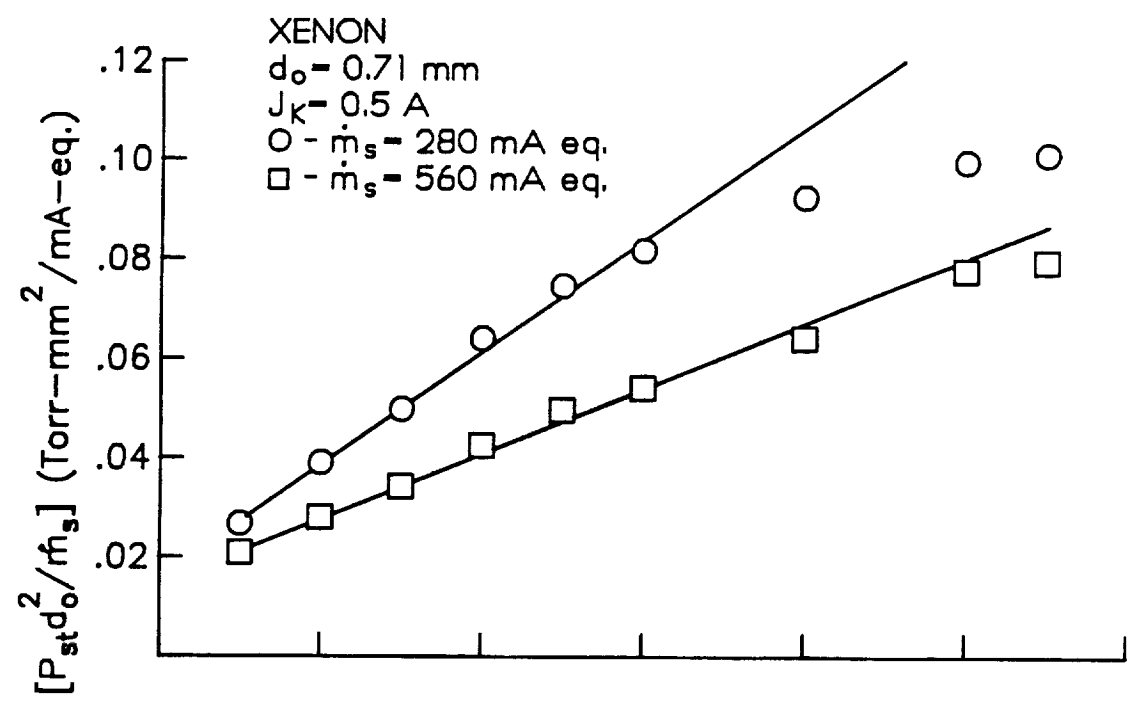


Fig. 13. Interior Pressure Correlations

where \dot{m}_s is the propellant flowrate supplied and \dot{m}_i is the propellant flowrate due to backstreaming ions. The term "backstreaming ions" used here represents ions that enter the cathode from downstream of the orifice and once they have backstreamed through the orifice the only way for them to leave the cathode is as neutrals. Ions that backflow, therefore, contribute to the total mass flowrate through the orifice. To calculate the ion backflow rate into the cathode, the ion current is assumed to be flowing at the space-charge limited condition¹² at which the backflowing ion current (J_i), which is numerically equal to the ion flowrate in mA eq., is given by:

$$J_i = J_e \sqrt{\frac{m_e}{m_i}} \quad (5)$$

In this equation the electron current J_e is assumed to be equal to the discharge current and m_e and m_i are the electron and ion masses respectively. When this total flowrate is used to form the correlating parameter in place of the flowrate of propellant being supplied directly to the cathode, the data plotted in the lower plot of Fig. 13 are obtained. This plot shows better correlation between the data, but the data are still not coincident. More work needs to be done to obtain accurate flowrate and pressure data and possibly to account for changes between continuum and free molecular flows to obtain better correlations. The lines in Fig. 13 are also not horizontal and this means that the effects of discharge current have not been completely taken into account. It is believed that this condition can be corrected by accounting for collisional drag induced by ions that backstream through the cathode orifice and collide with

neutral atoms flowing out of this small passage. Currently a method to account for these collisions is being developed.

CONCLUSIONS

There is significant experimental and theoretical evidence that ions can be created at potentials substantially above anode potential in a region of high plasma potential that develops immediately downstream of the orifice of a hollow cathode. Both Langmuir probe and RPA data suggest that the plasma potential in this region increases with discharge current to the point where ions created there could acquire a high kinetic energy. If they were then allowed to impinge on a cathode potential surface such as a baffle they could erode it rapidly. Emissive probe measurements do not show that such a region of high plasma potential develops as discharge current is increased, but theoretical analysis suggests that the probe does not operate properly near the cathode orifice because plasma densities are too high there.

Langmuir probe measurements made upstream and downstream of the orifice plate of a hollow cathode yield plasma property data that appear to be reasonable in light of data obtained previously at lower discharge current levels. Plasma densities reach very high levels at the cathode orifice, and these densities increase in about direct proportion to the discharge current. Cathode wall temperatures and interior pressures are found to be so high that they would be expected to limit cathode operating lifetimes under the conditions of cathode cooling and orifice size used in these tests. Additional effort is required to obtain a reasonable correlation between cathode flowrate,

discharge current and cathode interior pressure that can be used in mathematical models describing hollow cathode operation.

INVESTIGATION OF A HOLLOW CATHODE FAILURE

John D. Williams

During the grant period, a hollow cathode being used in a plasma contactor experiment failed. Subsequently, it was determined that the failure had occurred because a bellows in the gas supply valve had developed a leak that allowed air to enter the cathode while it was operating. Up until the time of failure it had been operating at a keeper current and voltage of 1.0 A and 8-15 V, respectively, and a net electron emission current to the vacuum chamber plasma of 0.5 A. The failure itself was characterized by a gradual increase in discharge voltage. The failure was reconized when the discharge went out and could not be resarted. The physical arrangement of the cathode throughout the testing period that preceeded failure is illustrated in Fig. 14. As this figure suggests, the cathode axis was pointed down, toward the Earth. Because the cathode utilized a keeper plate with no orifice in it and because the plate was located directly beneath the cathode, at least some and probably most of the material expelled during the failure was collected. The material that came out of the orifice during the period when it failed formed a small (2-3 mm dia.) mound on the keeper plate. This material appeared grey to the naked eye.

When the cathode was removed, the cathode tube was found to have a longitudinal crack in it and the swaged heater wire was also damaged in this same location. The condition of the cathode tube and heater suggested the failure occurred as a result of a high cathode interior pressure. As the cathode was being handled, the tungsten

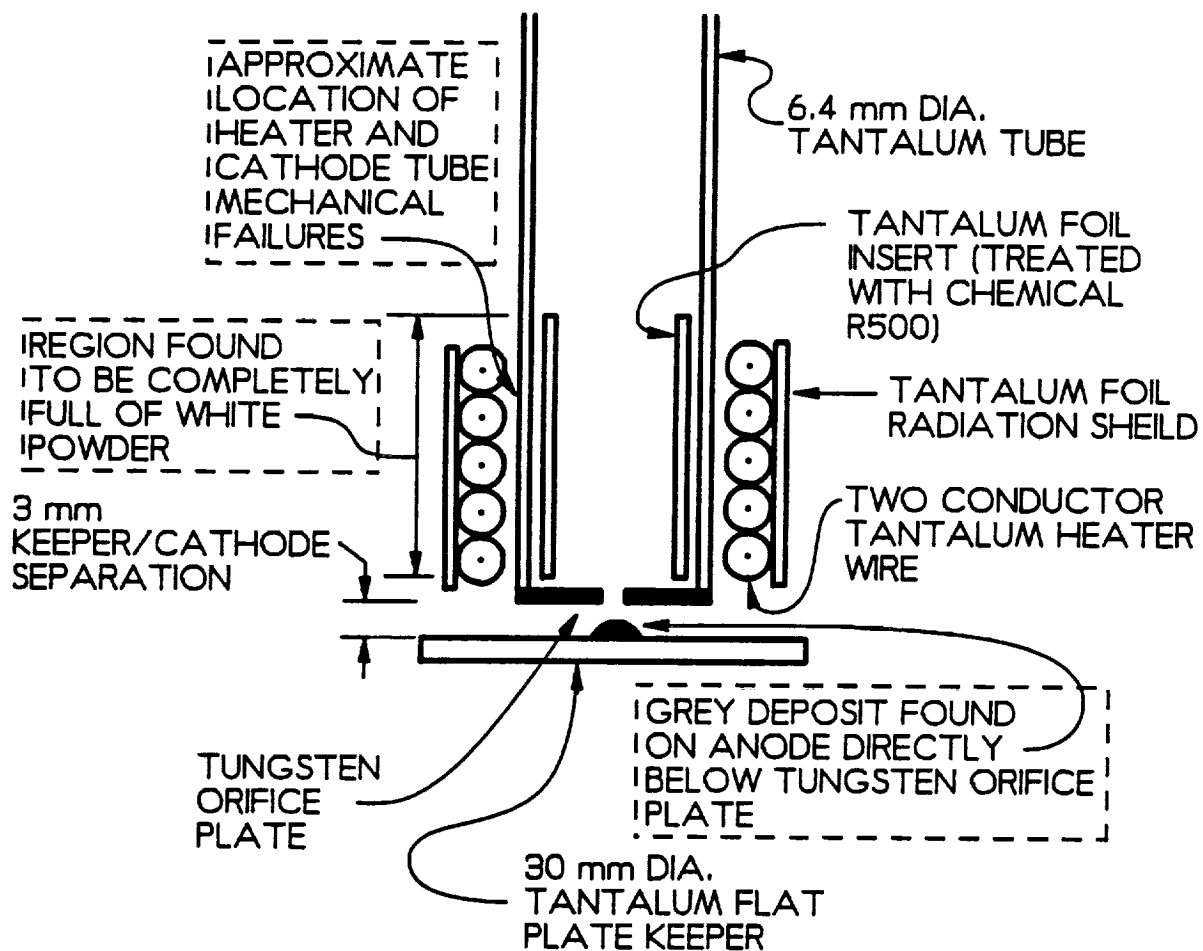


Fig. 14. Failed Hollow Cathode Diagram

orifice plate and part of the hollow cathode tantalum tube fell off and the badly deteriorated tantalum foil insert that had been treated with Chemical R-500 could be viewed. Inspection of the interior of the hollow cathode indicated that it was completely packed with a white powder. This powder was similar in appearance at all locations but there were a few particles with a slight green hue located close to the orifice plate. Inspection of the orifice showed that it had enlarged from an initial diameter of 0.38 mm before the failure to 0.46 mm after it.

The material from inside the cathode and the grey mound found on the keeper plate were all examined under a scanning electron microscope. Figure 15 shows the appearance of the white powder (Fig. 15a), the particles with the light green hue (Fig. 15b) and the hard grey material (Fig. 15c). The black and white bars on these micrographs indicate distances of 0.1 mm, 10 μ m and 10 μ m, respectively. The compositions of each of these materials was analyzed using energy dispersive x-ray analysis and the following results were obtained:

	<u>Element</u>	<u>Atomic %</u>
Hard Grey Material on the Anode	O	88
	W	11
	Ta	1
Particles with Light Green Hue	O	87
	W	4
	Ta	4
	Sr	5
	Ba	1
White Powder	O	70
	Ta	30

It should be noted in evaluating the above data that the apparatus used to make the compositional measurements is relatively



a. White Powder



b. Particles with Light Green Hue



c. Hard Grey Material

Fig. 15. Scanning Electron Micrographs of Materials from Failed Cathode

insensitive to nitrogen, so there could have been significant amounts of nitrogen that were not detected and are therefore not included among the elements listed. However, these data indicate the grey mound found on the keeper directly below the tungsten orifice plate is probably tungsten oxide from the orifice plate. The white powder found within the hollow cathode is most likely tantalum oxide (Ta_2O_3 and TaO_5). Finally, the unusual green-hued particles also found with the hollow cathode may have been produced through a reaction involving barium and strontium that came from the R-500-treated, tantalum foil insert. It is also possible, however, that some tungsten oxides, which are yellow and blue could combine to yield this color.

REFERENCES

1. Vaughn, Jason A., "Characterization of Hollow Cathode, Ring Cusp Discharge Chambers," appears in NASA CR-182255, P.J. Wilbur, Ed., Jan. 1989.
2. Vaughn J.A. and P.J. Wilbur, "Ring Cusp/Hollow Cathode Discharge Chamber Performance Studies," IEPC 88-064, 20th International Electric Propulsion Conference, Garmish-Partenkirchen, West Germany, October 1988.
3. Wilbur, P.J., J.R. Beattie and J. Hyman, "An Approach to the Parametric Design of Ion Thrusters," IEPC 88-064, 20th International Electric Propulsion Conference, Garmish-Partenkirchen, West Germany, October 1988.
4. Rawlin, V.K., "Internal Erosion Rates for a 10 kW Xenon Ion Thruster," AIAA Paper 88-2912, Boston, July 1988
5. Brophy, J.R. and Garner, C.E., "Tests of High Current Hollow Cathodes for Ion Engines," AIAA Paper 88-2913, Boston, July 1988.
6. Mirtich, M.J. and W.R. Keslake, "Long Lifetime Hollow Cathodes for 30 cm Mercury Ion Thrusters," AIAA Paper 76-985, Key Biscayne, FL, Nov. 1976.
7. Siegfried, Daniel E., "Langmuir Probe Sweep Circuitry," appears as Appendix A in NASA CR-165253, P.J. Wilbur, Ed., Dec. 1980.
8. Siegfried, Daniel E., "A Phenomenological Model for Orificed Hollow Cathodes," appears in NASA CR-168026, P.J. Wilbur, Ed., Dec. 1982, pp. 141-148.
9. Beattie, J.R., "Numerical Procedure for Analyzing Langmuir Probe Data," AIAA Journal, v. 13, No. 7, pp. 950-952, 1975.
10. Aston, G., "Ion Extraction From a Plasma," NASA CR-1159849, June 1980, pp. 12-19.
11. Anderson, J.D., Letter from P.J. Wilbur to M.R. Carruth at Marshall Space Flight Center concerning Grant NGT-50370, dated Jan. 1989.
12. Langmuir, I. , "The Interaction of Electron and Positive Ion Space Charges in Cathode Sheaths, " Phys. Rev., v. 33, No. 6, June 1929, pp. 954-989.
13. Williams, J.D. and Wilbur, P.J., "Ground-Based Tests of Hollow Cathode Plasma Contactors," Proceedings of the Third International Conference on Tethers in Space, San Francisco, May 1989.
14. Siegfried, Daniel E., "Xenon and Argon Hollow Cathode Research," appears as Appendix B in NASA CR-168340, P.J. Wilbur, Ed., Jan. 1984.

15. Lanczos, C. Applied Analysis, Prentice Hall, Inc., Englewood Cliffs, NJ, 1964, pp. 219-221.
16. Kohl, W.H., Materials and Techniques for Vacuum Devices, Van Nostrand-Reinhold, Princeton, N.J., 1967

Appendix A

IEPC - 88-064

**Ring Cusp/Hollow Cathode Discharge
Chamber Performance Studies**

J. A. Vaughn and P. J. Wilbur
Colorado State University
Fort Collins, Colorado U.S.A.

**DGLR/AIAA/JSASS 20th International
Electric Propulsion Conference**

October 3-6, 1988 / Garmisch-Partenkirchen, W. Germany

RING CUSP/HOLLOW CATHODE DISCHARGE CHAMBER PERFORMANCE STUDIES*

J. A. Vaughn[†] and P. J. Wilbur[†]
Colorado State University
Fort Collins, Colorado U.S.A.

ABSTRACT

An experimental study performed to determine the effects of hollow cathode position, anode position and ring cusp magnetic field configuration and strength on discharge chamber performance, is described. The results are presented in terms of comparative plasma ion energy cost, extracted ion fraction and beam profile data. Such comparisons are used to demonstrate whether changes in performance are caused by changes in the loss rate of primary electrons to the anode or the loss rate of ions to discharge chamber walls or cathode and anode surfaces. Results show 1) the rate of primary electron loss to the anode decreases as the anode is moved downstream of the ring cusp toward the screen grid, 2) the loss rate of ions to hollow cathode surfaces are excessive if the cathode is located upstream of a point of peak magnetic flux density at the discharge chamber centerline, and 3) the fraction of the ions produced that are lost to discharge chamber walls and ring magnet surfaces is reduced by positioning of the magnet rings so the plasma density is uniform over the grid surface and adjusting their strength to a level where it is sufficient to prevent excessive ion losses by Bohm diffusion.

INTRODUCTION

A study conducted by Hiatt¹ on a specially designed 8 cm dia. ring cusp magnetic field ion source has shown the effects of the positions of a loop filament cathode and loop anode on discharge chamber performance. Based on this work it was concluded that the performance of a ring cusp discharge chamber is best when 1) the surface of revolution of the innermost magnetic field line that intercepts the anode (i.e. the virtual anode surface) also intercepts the outermost ring of holes in the screen grid and 2) the surface of revolution of the outermost field line that intercepts the outer boundary of the electron source (i.e. the virtual cathode surface) is located relative to the virtual anode so that the discharge is on the threshold of extinction at the prevailing discharge voltage. Hiatt used a refractory filament cathode in his study because it was convenient and it could be positioned to control precisely the virtual cathode surface (i.e. the field line surface of revolution on which primary electrons are released into the discharge chamber). The study presented in this paper is similar in focus to the one conducted by Hiatt, but hollow cathodes, which are better suited for long life space applications, are used in place of the refractory filament cathodes used by Hiatt. The objective of this study has been to develop an understanding of the mechanisms whereby the field strength and location of ring cusp fields and the location of the hollow cathode and anode relative to these fields influence discharge chamber performance.

The tests were conducted on a small (7 cm diameter) ion source that utilizes high flux density

magnets. The use of these magnets in such a small source produced fields that penetrated deep into the chamber and as a result the volume of the low magnetic flux density zone in the chamber was small. It is difficult to achieve good performance in such a chamber, but the sensitivity of its performance to changes in such parameters as cathode and anode position is great and it was believed this would make it easier to identify the effects of changes and gain an understanding of the phenomena and mechanisms involved.

APPARATUS AND PROCEDURE

A cross sectional view of the 7.0 cm dia. multiple ring cusp discharge chamber used in the study is shown in Fig. 1. It was designed as a flexible research tool in which the dimensions labeled could be varied to determine their effect on performance. For this study, however, the steel discharge chamber diameter and length L and the beam diameter d_b were all held constant at 9.0 cm, 5.0 cm and 7.0 cm respectively. This short 5.0 cm discharge chamber was used to provide the flexibility necessary to position the hollow cathode both upstream and downstream of the ring cusp magnet reference location shown near the middle of the chamber. The magnetic field in the discharge chamber was produced by two radially facing ring magnets with their mid lines located 0.3 cm and -3.0 cm upstream of the screen grid and one axially facing ring magnet surrounding the hollow cathode and located on the upstream end of the discharge chamber. The central ring magnet, which is located a distance L_1 upstream of the grids, was varied during one test, but the ring magnet nearest the screen grid and the one on the

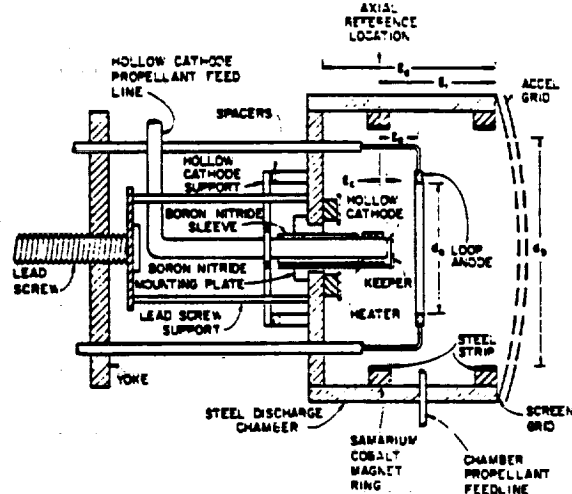


Fig. 1. Cross Sectional View of Ring Cusp Ion Source

*Work Supported by NASA Grant NGR-06-002-112

†Research Assistant, Department of Mechanical Engineering, Student Member

AIAA

†Professor, Department of Mechanical Engineering, Member AIAA

upstream face remained fixed throughout all tests. Note that the positions of the anode l_a and cathode l_c are measured with respect to the axial reference location at the center of the central (radially facing) ring magnet. Each ring magnet is made up of small (1.2 cm by 0.6 cm by 0.5 cm) samarium cobalt magnet segments with a strength of 0.27 T at their surfaces. The rings were formed by placing the magnet segments end-to-end either around the inner circumference of the discharge chamber (radially facing magnets) or in a circular pattern with an approximate diameter of 3.0 cm (upstream magnet). The steel strips and the washer, which are shown covering the radial and axially facing magnets respectively in Fig. 1, were used to distribute the magnetic flux uniformly over each ring surface during a test in which the numbers of magnet segments in each ring were varied and the effects of magnetic flux density on discharge chamber performance were investigated. The tantalum loop anode shown in Fig. 1 has a fixed diameter d_a of 5.2 cm and under the action of the lead screw and yoke it can be moved either upstream or downstream of the axial reference location. Because anode locations upstream of this location resulted in very poor performance and instabilities that prevented data collection, results pertaining only to downstream anode locations (positive values of l_a) will be presented.

A 0.64 cm dia tantalum tube was electron beam welded to a tungsten orifice plate with a 0.76 mm dia orifice to form the hollow cathode shown in Fig. 1. It utilized a R-500 treated rolled tantalum foil insert and was equipped with a swaged heater to facilitate startup. As the figure suggests the cathode is mounted in an electrically insulating boron nitride mounting plate/sleeve assembly, which keeps it isolated electrically but allows it to be moved axially from one test to the next by changing spacers at the cathode supports. This assembly is sufficiently leak tight to prevent significant propellant leakage from the discharge chamber into the vacuum system. The cathode orifice plate can be moved upstream (negative l_c) and downstream (positive l_c) of the axial reference location. The toroidal tantalum keeper shown in Fig. 1 has a 0.16 cm minor diameter and a 0.32 cm major diameter, is positioned 0.8 mm downstream of the hollow cathode orifice plate and is supported by the boron nitride mounting plate.

Xenon propellant which has been used in all tests was supplied through both the hollow cathode and the main propellant feed line. The total flow rate into the chamber, used to compute propellant efficiencies and neutral atom loss rates, reflected both of these measured flows as well as the backflow of xenon from the vacuum chamber through the grids.

The dish small hole accelerator grid (SHAG) optics set has screen and accel hole diameters of 1.9 mm and 1.5 mm, respectively, and these holes are arranged with a 2.2 mm centerline to centerline spacing. The cold grid spacing was 0.6 mm and the grids were maintained at 750 V (screen grid) and -250 V (accel grid) for all tests. The experiments were conducted in a 46 cm dia bell jar which was diffusion pumped to a background pressure in the low 10^{-6} Torr range. Typical operating pressures were in the high 10^{-6} to low 10^{-5} range over the range of xenon flows used in the tests.

A Faraday probe was swept through the beam 4 cm downstream of the accel grid to measure beam current density profiles. The probe consists of a 0.6 cm dia molybdenum ion current sensing disc that is shielded from the beam plasma electrons by a stainless steel screen biased 9 V below ground potential and is enclosed in a stainless steel body. Figure 2 shows a typical beam current density profile; this one was measured at a 100 mA beam current (J_b) and the other conditions defined in the legend by simultaneously inputting the ion current signal from the probe sensor and radial position of the probe to an x-y recorder. Current density profiles were analyzed numerically to determine the beam flatness parameter and total beam current (i.e., the integrated beam current) associated with the profile. Integrated beam currents were always found to agree with directly measured beam currents to within $\pm 10\%$. The beam flatness param-

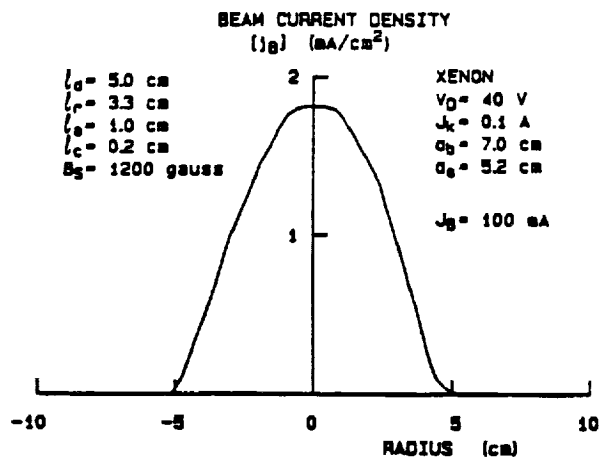


Fig. 2. Typical Beam Current Density Profile

eter is a measure of the uniformity of the beam profile and is defined as the average-to-maximum beam current density ratio measured close to the grids.

The magnetic field configuration of a discharge chamber has been found to have a major influence on the performance of that chamber and it is frequently important that the field prevailing in a chamber during a test be described. This can be accomplished by using iron filings maps and flux density contour maps measured in the actual chamber. During the conduct of this work, however, it was determined that a computer algorithm developed by Arakawa³ could be used to generate both types of maps reliably, quickly and with relative ease so it has been used to generate the maps contained in this paper. The computer algorithm allows the user to enter parameters which describe the discharge chamber geometry, the permanent magnet locations in the discharge chamber and their magnetization levels. The program then solves for the magnetic field vector potential at each element using the finite element method. The magnetic field vector potential can be plotted as a function of position in the discharge chamber to produce a computer-generated (pseudo) iron filings map like the one shown in Fig. 3. This particular map was produced for a flux density measured at the surface of the steel strips B_z of 1200 gauss and the geometric data shown in the legend. Because the computer program generates an axis-symmetric view, only half of the map is plotted. By taking the gradient of the vector potential map the program can also be used to generate a constant flux density contour map. Figure 4 is a typical example of such a computer-generated magnetic flux density contour map for the same discharge chamber and magnet configuration that produced the filings map shown in Fig. 3. It should be noted that the contours shown decrease logarithmically with distance from the discharge

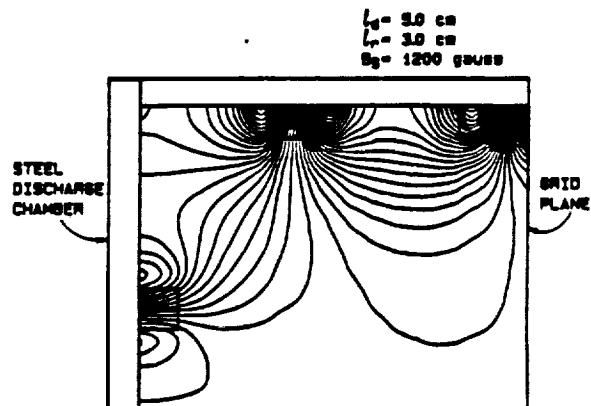


Fig. 3. Pseudo Iron Filings Map (Computer Generated)

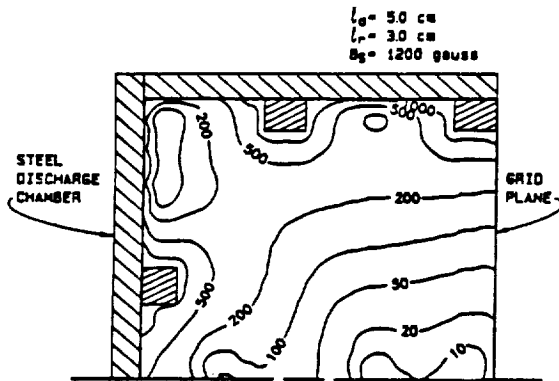


Fig. 4. Magnetic Flux Density Contour Map (Computer Generated)

chamber walls. Maps like those shown in Figs. 3 and 4 can be used to explain the effects of magnetic field changes on discharge chamber performance. They make it possible to view the effects of changing ring magnet positions and strengths on magnetic field line patterns and flux densities in the discharge chamber.

Tests were initiated by flooding the hot hollow cathode with xenon propellant and then applying a sufficiently high keeper voltage (~200 V) to start a keeper discharge. After startup the keeper voltage was varied as required to maintain a 0.1 A keeper current for all testing. The cathode flowrate was reduced once the keeper discharge had started and a discharge to the anode, which was held at a 40 V potential, was established. The current being drawn to the anode was maintained at approximately an ampere by controlling the main and/or cathode flowrates until thruster operation had stabilized. After a period of stabilization, tests were typically conducted by setting the xenon flowrate through the hollow cathode to ~20 mA eq (Xe) and that into the discharge chamber to ~95 mA eq (Xe) while maintaining the discharge voltage V_d at 40 V. The cathode and discharge chamber flowrates m_c and m_d , the vacuum chamber background pressure P_0 , the keeper voltage V_k , the discharge current J_d , beam current J_b , and total ion production rate expressed as a current J_p , corresponding to this operating condition were all measured and recorded. Measurement of the total ion production current was accomplished by biasing the discharge chamber walls and screen grid 30 V negative of the hollow cathode to repel all electrons from these surfaces and sensing the ion current arriving at the discharge chamber magnet and wall surfaces J_w and the screen grid J_g . These two surfaces were isolated from each other so the currents of ions to each surface could be separated. The sum of these two currents plus the beam current is the total ion production current.

$$J_p = J_w + J_g + J_b \quad (1)$$

Knowing the total ion production current the plasma ion energy cost ϵ_p (the energy cost of producing an ion in the plasma) and the extracted ion fraction f_b (the fraction of the total ions produced in the discharge chamber that are being extracted into the beam) could be computed using the expressions

$$\epsilon_p = \frac{V_d(J_d - J_p)}{J_p} \quad (2)$$

and,

$$f_b = \frac{J_b}{J_p} \quad (3)$$

The loss rate of neutral atoms through the grids, which is proportional to the discharge chamber atomic

density and is therefore called the neutral density parameter, was also computed using

$$\dot{n}(1 - \eta_u) = \dot{n}_c + \dot{n}_d + \frac{P_0 A_b \phi e}{\sqrt{2\pi} m_i k T_0} - J_b \quad (4)$$

In this equation, A_b the area of the beam, ϕ the transparency of the grids to neutral atom back flow, m_i the atom/ion mass, k Boltzmann's constant, e the electronic charge and T_0 the ambient (vacuum chamber) neutral atom temperature are all known.

After all the currents (J_d , J_b and J_p), the voltage (V_d) and other data had been recorded at the initial flow condition, the discharge chamber flowrate was increased while the hollow cathode flowrate and discharge voltage were held constant. This caused the discharge current and hence the other currents and keeper voltage to change and their new values were recorded. This process of increasing discharge chamber flowrate and recording data was continued until the accel grid impingement current increased to ~10 mA. The hollow cathode and discharge chamber flowrates were then both reduced and the process of recording data, as the discharge chamber flowrate was increased incrementally and the cathode flowrate and discharge voltage were held constant, was continued. This process of reducing the hollow cathode flowrate and increasing the discharge chamber flowrate incrementally continued until data had been recorded over a wide range of discharge chamber neutral atom density levels (and therefore a wide range of discharge currents) at the prescribed 40 V discharge voltage. Typically, the hollow cathode flowrate had to be decreased from 20 to 10 mA eq (Xe) while the discharge chamber flowrate had to be increased from 95 to 460 mA eq (Xe) to cover an adequate range of neutral atom densities.

The effects of varying the position of the anode and the hollow cathode were investigated by first placing the cathode at a particular location in the discharge chamber and then moving the anode downstream in increments (i.e. onto field lines located progressively further from the virtual cathode). At each anode position, plasma ion energy cost and extracted ion fraction data were recorded as a function of neutral density parameter using the procedure described in the preceding paragraph. This process continued until the anode was so far downstream of the cathode that the discharge currents drawn to the anode were small. The cathode was then repositioned and the process of moving the anode and varying the flowrates was repeated. The range of cathode positions investigated was from 0.6 cm upstream ($l_c = -0.6$ cm) to 0.5 cm downstream ($l_c = 0.5$ cm) of the reference location.

A second set of experiments was conducted in which the effects of varying the magnetic flux density B_0 at the surfaces of both the steel strips and the washer covering the ring magnets was investigated. The magnetic flux density was varied by removing individual samarium cobalt magnet segments from each ring magnet and placing a steel strip or washer of sufficient thickness to produce a common, uniform surface magnetic flux density over the entire surface of each ring magnet. This required that the thickness of the strips and the washer be increased as the surface magnetic flux density was decreased in increments from 2700 gauss to 350 gauss. At each magnetic flux density condition plasma ion energy cost and extracted ion fraction data were recorded as a function of discharge chamber neutral density parameter using the experimental procedure described previously.

A final experiment was conducted in which the upstream ring magnet position (l_r) was varied from 2.7 to 3.6 cm in increments of 0.3 cm to determine the effects of such changes on discharge chamber performance. The positions of the anode and hollow cathode were held constant relative to the reference location on this magnet during the test, so magnet ring, anode and cathode were all moved in unison. The procedures used to measure plasma ion energy cost data as a function of discharge chamber neutral density parameter were as described previously.

EXPERIMENTAL RESULTS

Experimentally measured discharge chamber performance can be described in terms of plasma ion energy cost ϵ_p vs. discharge chamber neutral density parameter $m(1 - \eta_u)$ plots like the example shown in Fig. 5. These particular data were recorded using the discharge chamber having the configuration described by the parameters listed in the legend when the flux density B_s at the surface of each magnet was 1200 gauss.

The theory developed by Brophy⁴ suggests the experimental data of Fig. 5 should be fitted by the equation

$$\epsilon_p = \epsilon_p^* (1 - \exp[-C_0 m(1 - \eta_u)])^{-1} \quad (5)$$

when the parameters ϵ_p^* (the baseline plasma ion energy cost) and C_0 (the primary electron utilization factor) are selected properly. In the case of the data shown in Fig. 5 a non-linear least-squares curve fit of the data yields the values of those parameters given on the figure. The data and the curve show a good correlation between the data and the model that is typical of all of the results obtained in this study.

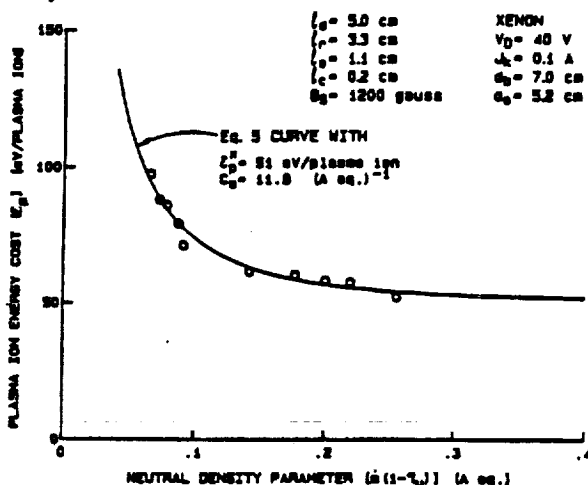


Fig. 5. Typical Discharge Chamber Performance Data

The primary electron utilization factor C_0 like the one computed from the data of Fig. 5 describes the probability that primary electrons coming from the cathode will have inelastic collisions and lose the bulk of their energy before they reach an anode potential surface. The baseline plasma ion energy cost ϵ_p^* is the average energy cost of producing an ion in the discharge chamber when the neutral density is sufficiently high so that all primary electrons have inelastic collisions before they reach the anode. Ideally, the baseline plasma ion energy cost assumes a nominal value determined by the type of propellant, the discharge voltage V_0 , and the potential from which electrons are drawn into the chamber V_c (i.e. the electron source potential). However, if all of the ions produced in the chamber are not measured (e.g. some escape to the hollow cathode or to the anode), or if Maxwellian electrons carry substantial amounts of energy to the anode, the baseline plasma ion energy cost ϵ_p^* will increase above its nominal value. The particular discharge chamber used in these tests was designed so ion losses to the hollow cathode and anode could be made small to minimize the effects of these ion losses on ϵ_p .

The other parameter needed to describe discharge chamber performance is the extracted ion fraction f_b (i.e. the fraction of the ions produced in the discharge chamber that are extracted into the beam). This parameter is a measure of the effectiveness of the magnetic field in preventing the ions from reaching discharge chamber surfaces and directing them toward the grids.

The advantage of describing discharge chamber performance in terms of the energy cost of a plasma ion (i.e. C_0 and ϵ_p^*) and the extracted ion fraction f_b is that they make it possible to identify the mechanisms responsible for changes in discharge chamber performance. For example one can determine if changing the location of the anode causes a detrimental change in performance and if this change is due to increased losses of primary electrons (a decrease in C_0), increased losses of ions to hollow cathode or anode surfaces or an increase in the average energy of Maxwellian electrons being collected by the anode (an increase in ϵ_p^*) or increased losses of ions to some other discharge chamber surface (a decrease in f_b).

It should be noted that a knowledge of the values of ϵ_p^* , C_0 and f_b is sufficient to enable one to compute the associated beam ion energy costs of a chamber as a function of propellant utilization efficiency.

Effects of Anode Position

The results of the study conducted by Hiatt¹ showed that discharge chamber performance improves when the anode is moved downstream of the axial reference location up to the point where the discharge is on the verge of extinction. It was suggested that the downstream movement of the anode improved performance because it reduced the loss rates of higher energy Maxwellian and primary electrons, to the anode up to the point where the orthogonal line integral of the magnetic field between the virtual cathode and anode surfaces became too great and the discharge would go out. Similar results were also observed in the present study where a hollow cathode was used in place of the filament cathode. However, in the case of the hollow cathode experiments, an actual extinction of the discharge was not observed. Rather the discharge current would decrease until it became too small to produce significant numbers of ions as the anode was moved downstream and the discharge voltage and propellant flowrate were held constant. The higher the discharge voltage and propellant flowrate the further downstream the anode could be moved before this situation developed.

Typical experimental results obtained during a test to investigate the effects of moving the anode on discharge chamber performance are presented in Fig. 6. These results are qualitatively similar to those obtained by Hiatt¹ in a similar discharge chamber equipped with a filament cathode. The data were recorded using a chamber with the dimensions shown in the legend when the magnetic surface flux density B_s was 1200 gauss. The data points shown at $l = 0.96$ cm were recorded with the anode just upstream of the operating point where the maximum discharge current that could be drawn dropped precipitously at nominal discharge voltage and total flow conditions (40 V and 150 mA eq (Xe)). It is noted that low values of ϵ_p and high values of C_0 and f_b are desirable so operation with l far downstream (large values of l) is preferred.

Because the propellant, discharge voltage and electron source potential (keeper voltage) were constant for these tests it is argued that the decrease in baseline plasma ion energy cost with downstream anode movement is caused by the decrease in the average energy of Maxwellian electrons being collected at the anode that has been observed previously.^{4,5} This preferential collection of progressively lower energy electrons as the anode is moved downstream occurs because the momentum transfer collision cross section for electrons with atoms and ions increases as electron energy decreases. Hence as the virtual anode is moved further from the virtual cathode (i.e. the anode is moved downstream) electrons which have the lowest energies (and therefore have many collisions) are most likely to migrate across magnetic field lines and reach the anode. Thus, downstream movement of the anode reduces the average energy of the Maxwellian electrons reaching the anode and this induces the decrease in ϵ_p as l is increased.

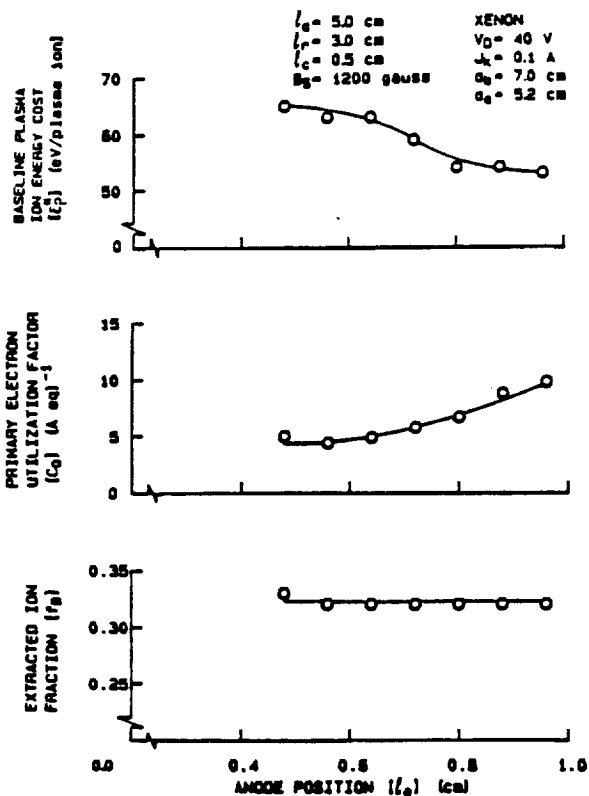


Fig. 6. Effect of Anode Position on Discharge Chamber Performance Parameters

The primary electron utilization factor (C_0) is observed to increase as the anode was moved downstream. Because the primary electrons have an energy that is high compared to that of the Maxwellian electrons, they have low collision probabilities and therefore cannot cross field lines easily. As the anode is positioned further downstream the number of field lines that must be crossed to reach the anode increases, therefore the primary electron loss rate decreases and the primary electron utilization factor increases to reflect this.

Figure 6 shows the extracted ion fraction remains constant as the anode is moved downstream. This indicates that the total ion production rate and the beam current are changing at the same rate. During typical experiments the beam current was observed to increase as the anode was moved downstream and the discharge voltage, current and total flowrate were held constant (accomplished by adjusting the flow distribution). It is obvious from looking at Fig. 6 that this increase in beam current occurred because downstream anode movement induces an increase in C_0 , a decrease in e_p and no change in f_g . Physically this occurs because the energy in both the primary and Maxwellian electron groups is being better utilized to make ions and the fraction of these ions that escape the discharge chamber into the beam remains constant as the anode is moved downstream.

The Comparative Behavior of Refractory Filament and Hollow Cathodes on Performance

When a filament cathode electron source is used one can control the shape and location of the region from which primary electrons are supplied to the discharge, but with a conventional hollow cathode one is limited to electron emission from a point on the discharge chamber centerline. A question that arises is whether a filament cathode emitting electrons from the same point on a discharge chamber centerline would give the same performance as a hollow cathode. In order to address this question an experiment was

conducted in which a discharge chamber was operated using a hollow cathode and then a small diameter (2 mm) coiled filament positioned at the axial location previously occupied by the hollow cathode orifice. The discharge chamber remained unchanged except for the cathode substitution.

Figure 7 shows the comparative plasma ion energy cost vs. neutral density parameter and extracted ion fraction data measured with the cathodes positioned downstream of the cusp at $l_c = 0.2$ cm and the rest of the discharge chamber parameters as listed in the legend. The data show no difference in either the extracted ion fraction or the primary electron utilization factor, however, the baseline plasma ion energy cost for the hollow cathode is approximately twice that of the filament cathode. These large differences in baseline plasma ion energy cost can be accounted for by recognizing that the primary electrons acquire an energy approximately equal to the difference between the anode and electron source potentials. In the case of the filament cathode this would be the potential difference between the filament surface and the anode (i.e. the discharge voltage). For the hollow cathode, where it might be assumed the electron source potential is about equal to the keeper potential (V_k) the appropriate potential difference would be the difference between the discharge and keeper voltages. In this case the plasma ion energy cost would be given by

$$e_p = \frac{(V_D - V_k)(J_D - J_P)}{J_P} \quad (6)$$

The difference in plasma ion energy costs given by this equation and by Eq. 2 represents the energy cost per plasma ion being used to operate the hollow cathode.

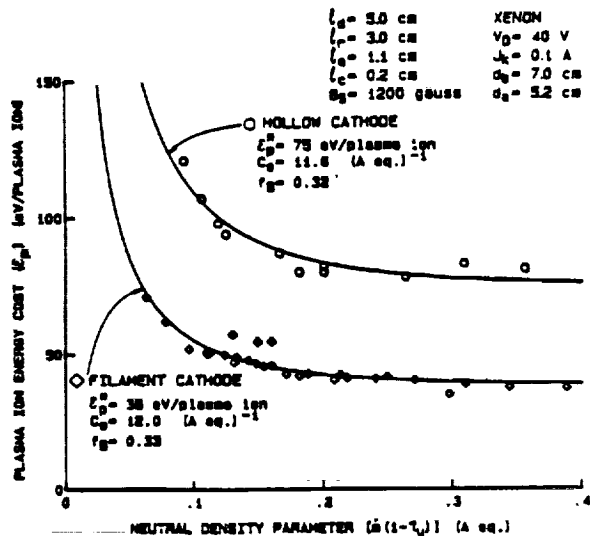


Fig. 7. Hollow Cathode/Filament Cathode Performance Comparison

During the conduct of the test with the hollow cathode, the keeper voltage generally varied from 12 V at low neutral densities (high cathode flows) to 20 V at high neutral densities (low cathode flows). If the electron source potential was assumed to be equal to that of the keeper at high neutral densities (~20 V) and Eq. 6 was used to calculate the plasma ion energy cost, the hollow cathode data (circular symbols) shown in Fig. 8 were computed. These data show good agreement between all parameters (e_p , C_0 and f_g) for the filament and hollow cathode cases thereby suggesting the hollow cathode operating power has been properly removed from baseline plasma ion energy cost. This suggests that discharge chamber performance with a hollow cathode and with a filament cathode are comparable if hollow cathode operating power is accounted for properly. It is noted that using the keeper voltages measured at each discharge

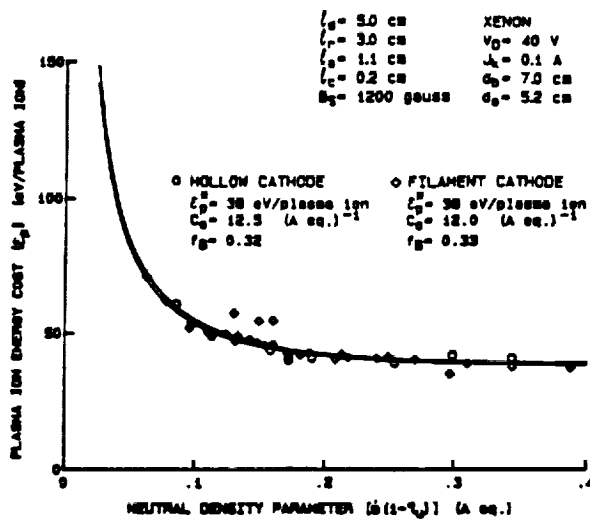


Fig. 8. Hollow Cathode/Filament Cathode Performance Comparison (with Keeper Potential Correction)

current condition rather than the constant (20 V) value did not result in the same degree of agreement as that shown in Fig. 8. When the variable keeper voltage values were used in Eq. 6 the values of both ϵ_p and C_0 determined by the least squares fitting of the data for the hollow cathode departed from those for the filament cathode. While it may be that electrons are being supplied from this higher potential as keeper voltage changes, more research into the subject of hollow cathode vs. filament cathode effects on discharge chamber performance to enhance understanding of the phenomena that are occurring is considered desirable.

Effects of Hollow Cathode Axial Position

Tests were conducted in which the anode position and magnetic field configuration were fixed and the effect of hollow cathode movement along the thruster centerline was examined. Discharge chamber performance plots like those in Fig. 5 were generated at each cathode position and discharge chamber performance parameters (ϵ_p , C_0 and f_p) were determined from these data using Eqs. 3 and 5. Figure 9 shows the variation in these parameters as a function of hollow cathode position over the range $-0.6 \leq l_c \leq 0.5$ cm. These data suggest the primary electron utilization factor is not affected by cathode position but both baseline plasma ion energy cost and extracted ion fraction increase as the cathode is moved upstream of the reference (central ring cusp) location. One of these effects is beneficial (increased extracted ion fraction) and the other is detrimental (increased baseline plasma ion energy cost). The fact that these curves show similar behavior suggests both parameters are being affected by a common phenomenon. The behavior shown in Fig. 9 could be explained qualitatively if upstream movement of the hollow cathode causes a fraction of the ions that were being lost to the chamber walls to be lost to the hollow cathode itself. This effect would cause both parameters to increase with upstream cathode movement because ions lost to the cathode are not measured and this therefore causes a decrease in the measured ion production J_p which appears in the denominator of the expressions from which these parameters (Eqs. 2 and 3) are computed. A development in Appendix A shows in fact that the values of these parameters are related by the equation

$$f_p = \frac{\hat{f}_p}{\hat{\epsilon}_p} \quad (7)$$

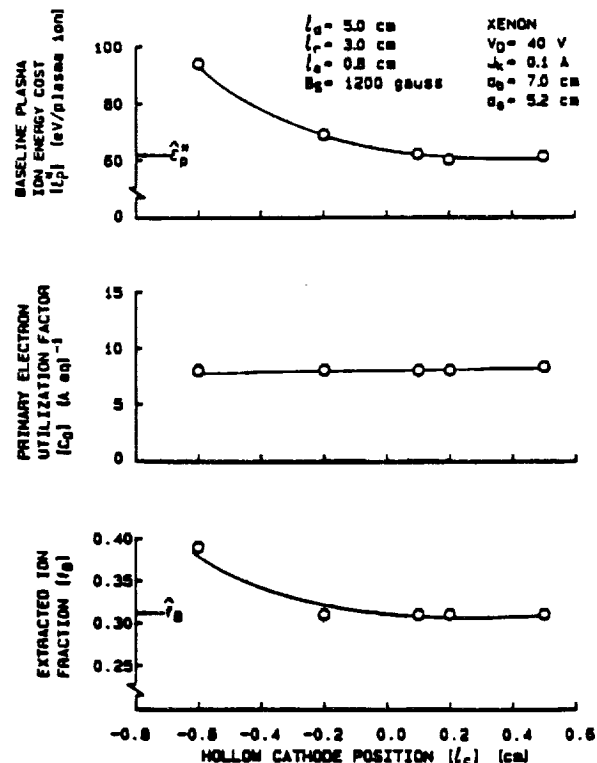


Fig. 9. Effect of Centerline Hollow Cathode Axial Position on Discharge Chamber Performance Parameters

where \hat{f}_p and $\hat{\epsilon}_p$ (identified in Fig. 9) are the values of the parameters associated with the cathode positioned in the downstream region where the ions lost to the hollow cathode are low. Finally, it is noted that the use of Eq. 6 rather than Eq. 2 to determine values of ϵ_p from which values of $\hat{\epsilon}_p$ are computed as a function of cathode position (i.e. to account for losses associated with the electron source potential) causes the data from these tests to fall into even better quantitative agreement with Eq. 7. All of these results taken together suggest that the increase in extracted ion fraction induced by upstream cathode movement is artificial and is compensated by a corresponding increase in baseline plasma ion energy cost to the point where no substantial net effect on beam ion energy cost is realized.

The reason why ion losses to the cathode increase as it is moved upstream can be understood by considering the centerline magnetic flux density profile shown in Fig. 10. These measurements, which

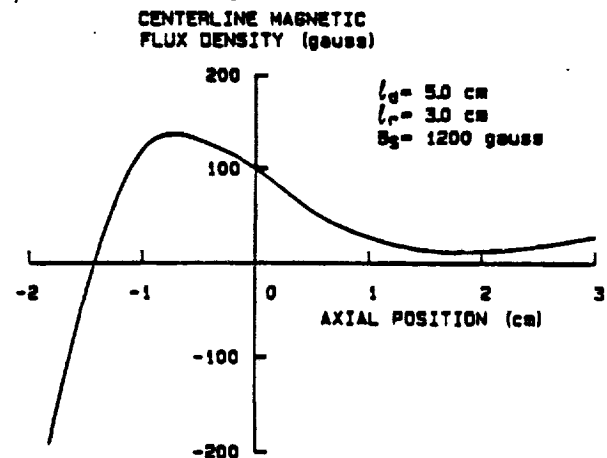


Fig. 10. Centerline Magnetic Flux Density Profile

were made using a gaussmeter, show the cathode is moving into a progressively higher magnetic flux density environment as it is moved upstream. This would be expected to confine electrons (and therefore ions) progressively closer to the cathode and would promote ion losses to cathode surfaces at the expense of ion losses to the chamber walls.

It is noted that the data of Fig. 9 are limited to upstream cathode positions greater than -0.6 cm and Fig. 10 shows this is a region of negative flux density gradient. Movement of the hollow cathode upstream of the point of maximum flux density (~ -0.8 cm), however, caused the performance of the ion source to degrade rapidly because of what appeared to be a dramatic increase in the baseline plasma ion energy cost that overshadowed corresponding modest changes in extracted ion fraction. Thus test results obtained by moving the hollow cathode axially suggest overall discharge chamber performance as reflected in beam ion energy costs, which vary to first order as e_p/f_p , is unaffected by cathode position as long as it is downstream of the extreme, centerline flux density point. As the cathode is moved into regions of higher flux density, however, a greater fraction of the ions produced near the cathode appear to go to the cathode rather than to the chamber walls.

Magnetic Field Effects

The magnetic field configuration in a discharge chamber is important because it must contain the ions away from the chamber walls and near the screen grid where they can be extracted into the beam. Two criteria associated with the magnetic field that should be met for a good design are: 1) a sufficiently high magnetic flux density near the surface of the discharge chamber walls to ensure proper ion containment and 2) proper positioning of the ring magnet so the virtual anode field line will intersect the outer most ring of holes in the screen grid. These criteria were difficult to meet simultaneously with the small diameter discharge chamber used in

these tests because fringing fields tended to penetrate deep into the chamber and reduce the low field strength volume in it. However, effects associated with these criteria were investigated by changing the flux density of the magnets and the axial location of the central ring magnet (i.e. varying l_c shown in Fig. 1).

When the magnetic flux density measured at the surface of the steel strips and washer on the magnets (Fig. 1) was varied from 350 gauss to 2700 gauss the discharge chamber performance parameters varied in the manner shown in Fig. 11. These data suggest that increased magnetic flux density induces 1) slightly reduced energy losses through Maxwellian electron losses to the anode (e_p decreases with B_0), 2) improved primary electron containment (C_0 increases with B_0) and 3) improved ion containment (f_p increases with B_0). All of these trends improve performance and they are most significant over the magnetic flux density range from 350 to 1200 gauss. Beyond 1200 gauss the improvements in all of the parameters appear to be small.

Some insight into these trends can be gained by considering a typical pseudo iron filings map (Fig. 3 - the shape of the lines in this figure do not change significantly with flux density) and pertinent magnetic flux density contour maps (Fig. 12) associated with the discharge chamber. In viewing Fig. 3 it should be recognized that ions and electrons can diffuse readily along field lines and with difficulty across them. They can therefore diffuse readily (at the ambipolar diffusion rate) to cusps where electrons will generally be reflected because the pole pieces do not serve as anodes in this thruster and significant numbers of ions will be lost to the ring magnet surface. This ion loss rate is believed to have a relatively weak dependency on magnet strength. Ions and electrons can also be lost by diffusing more slowly (at the Bohm diffusion rate) across field lines; electrons being lost to the anode

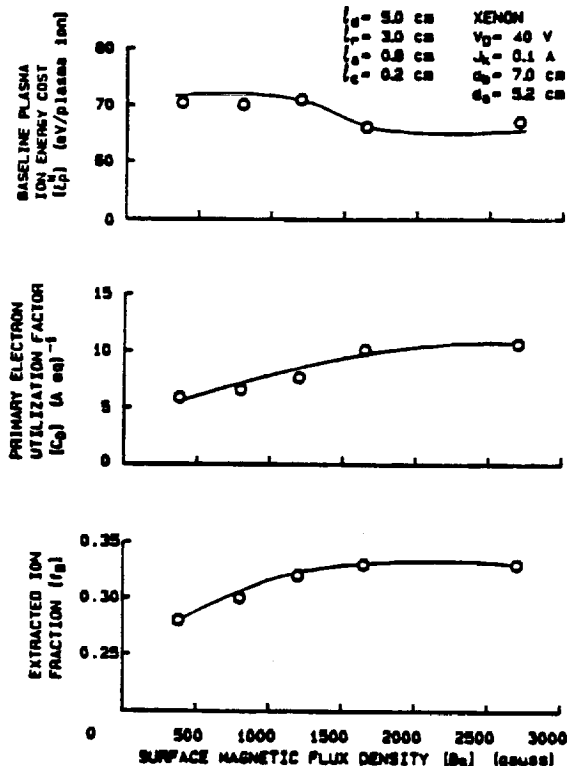


Fig. 11. Effect of Magnet Strength on Discharge Chamber Performance Parameters

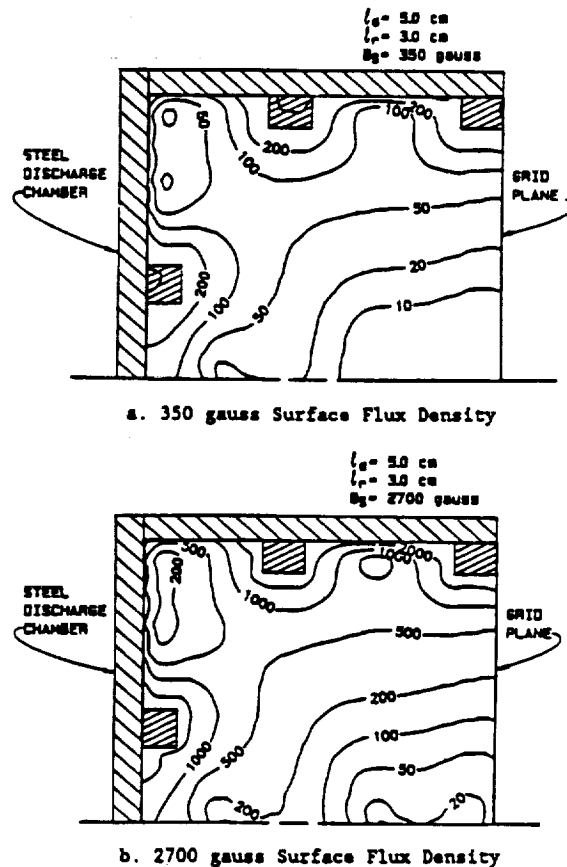


Fig. 12. Magnetic Flux Density Contour Maps

once they reach the field line which intersects the anode and ions being lost to the discharge chamber walls. This ion loss mechanism (Bohm diffusion) decreases as the magnetic flux density increases but at some magnetic field strength (presumably near 1200 gauss in the case of the chamber configuration associated with the data of Fig. 11) the ion loss rate to the walls becomes small compared to the ion loss rate through the cusps.

Figure 12 contains magnetic flux density contour maps which show the effects of surface flux density B_s on magnetic flux density in the discharge chamber. Comparison of Figs. 12a and 12b shows considerably higher flux densities develop throughout the chamber when the surface flux density B_s is increased from 350 to 2700 gauss. Because the Bohm diffusion coefficient varies inversely with flux density, electron and ion flow across field lines to the anode and to the chamber wall will be substantially less in the high flux density case.

Positioning of the ring magnet so that the virtual anode field line intersects the outermost ring of holes in the screen grid is also important in determining the overall performance of an ion thruster. When the virtual anode field line intersects these outer holes, a larger fraction of the neutrals are utilized because they cannot escape the chamber without passing through a zone where they can be ionized. Utilization of these additional neutrals increases the beam current which can be extracted from the discharge plasma and increases the uniformity of the beam current density profile. The parameter that describes the uniformity of the beam current density and thereby infers the proximity of the virtual anode field line surface of revolution to the surface of revolution of the field line passing through the outermost ring of holes is the beam flatness parameter (the ratio of average-to-peak beam current density measured near the grids).

In this study the central ring magnet was moved axially (l_r of Fig. 1 was varied) in order to induce some degree of movement in the virtual anode field line and the beam flatness parameter and discharge chamber performance parameters were measured as a function of this movement. The effects of varying l_r from 2.6 to 3.6 cm on beam flatness parameter and the discharge chamber performance parameters ϵ_p , C_0 and f_e are shown in Figs. 13 and 14 for the case where the anode and cathode positions (l_a and l_c in Fig. 1) were held constant relative to the ring magnet being moved. The test was conducted in this way because earlier test had suggested that holding l_a and l_c constant should tend to hold baseline plasma ion energy cost ϵ_p and primary electron utilization factor C_0 relatively constant. The tests were conducted using a ring magnet surface flux density of 1200 gauss because lesser values yielded poor performance parameters (Fig. 11) and higher values tended to reduce the volume of the low magnetic flux density volume in the chamber (Fig. 12b). The data presented in Fig. 13 show an increase in the flatness parameter as the ring magnet position is moved

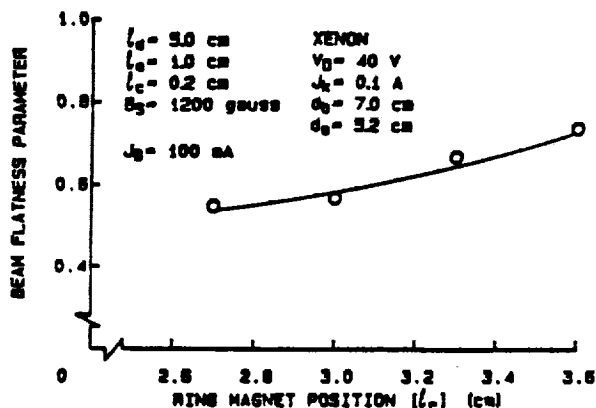


Fig. 13. Effect of Ring Magnet Position on Beam Flatness Parameter

upstream, presumably because more of the screen grid is exposed to the uniform density discharge chamber plasma. This suggests the optics system is being used more effectively and less unionized propellant is being lost because of a non-uniform ionizing plasma across the grids (a fact that was also confirmed by independent propellant utilization efficiency measurements).

If the rate at which ions are being extracted into the beam increases then one might also assume that a similar increase in the extracted ion fraction should occur. However, the discharge chamber performance data contained in Fig. 14 (bottom plot) show that the opposite has occurred; that the extracted ion fraction decreases as the ring magnet is moved upstream. Examination of the data suggests this occurs because of increased losses to discharge chamber walls. The other performance data in Fig. 14 suggest the baseline plasma ion energy cost goes through a slight minimum and taken together the data suggest there is an optimum ring magnet position near 3.0 cm.

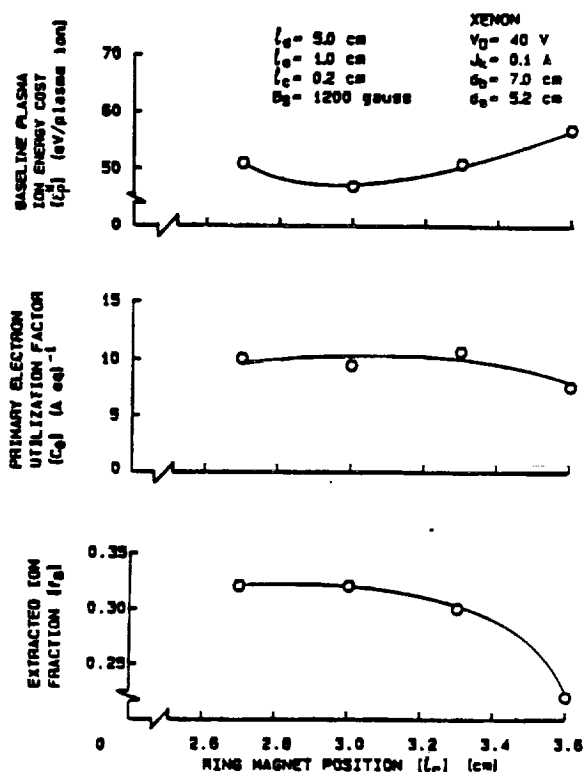


Fig. 14. Effect of Ring Magnet Position on Discharge Chamber Performance Parameters

The reason the extracted ion fraction decreases while the beam flatness parameter increases when the ring cusp is moved upstream to a position 3.6 cm from the grid plane can be seen by comparing the flux density contour map in Fig. 15 with the one in Fig. 4 (which pertains to $l_r = 3.0$ cm). This comparison shows the magnetic flux density near the discharge chamber wall between the two radially facing ring magnets decreases as the central magnet is moved upstream and this would be expected to facilitate diffusion of ions across field lines to the wall. In fact increasing the value of l_r from 3.0 to 3.6 cm causes the measured ion current going to the discharge chamber wall to increase 30% and this causes the corresponding 30% decrease in the extracted ion fraction shown in Fig. 14. Comparison of Figs. 4 and 15 also indicates the diameter of the lower flux density region near the grids tends to increase as l_r is increased. It is believed that it is this effect that causes the beam flatness parameter to increase with l_r .

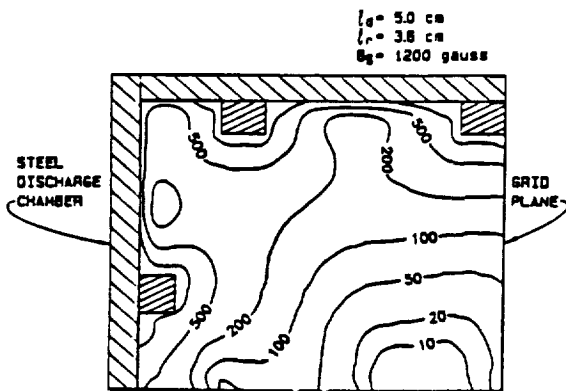


Fig. 15. Magnetic Flux Density Contour Map for $I_r = 3.6$ cm

In order to produce a magnetic field configuration that would produce good discharge chamber performance and a flat ion beam, the magnetic flux density near the wall should be large enough to prevent ion losses through Bohm diffusion, yet allow the primary electron plasma to occupy a large fraction of the discharge chamber volume adjacent to the grids. In tests conducted with a filament cathode, small diameter ion source, this condition was approached by using a high flux density ring magnet and setting the diameter of the annular zone of electron emission from the cathode to a substantial fraction of the source diameter. This made it possible to achieve relatively high primary electron (and therefore plasma) densities over a rather large volume in the discharge chamber and still limit ion diffusion to the chamber walls. For the present study where a hollow cathode was being used, on the other hand, the point of electron injection remained on the chamber centerline and altering the magnetic field so the volume occupied by the high density plasma could expand also enhanced the rate of ion diffusion to the chamber walls. It is argued therefore, that the simultaneous requirements for low ion diffusion losses and substantial plasma densities near the outermost grid holes tend to be mutually exclusive in small diameter, hollow cathode discharge chambers of the type investigated in this study.

CONCLUSIONS

By examining the effects of changes in hollow cathode discharge chamber performance parameters induced by changes in discharge chamber dimensions and magnetic field strengths it is possible to examine specific physical phenomena that induce changes in discharge chamber performance. This technique has been used to identify the effects induced by changes in anode and hollow cathode position and magnetic field strength and geometry on the performance of a ring cusp discharge chamber with a hollow cathode electron source, three magnet rings, and a 7 cm dia beam.

Results obtained with the anode positioned downstream of a ring cusp in a hollow cathode equipped discharge chamber, are qualitatively similar to those obtained by Hiatt¹ using a discharge chamber with a similar beam diameter and a refractory filament cathode. Movement of the anode downstream of the ring cusp toward the grids reduces the primary electron losses to the anode and causes the primary electron utilization factor C_0 to increase continuously up to the point where the discharge impedance becomes so great that significant discharge currents can no longer be drawn without increasing the discharge voltage. When the hollow cathode is moved along the chamber centerline the extracted ion fraction and baseline plasma ion energy cost change in such a way that their combined effect on performance is almost nil provided the cathode is not moved upstream of the peak centerline magnetic flux

density. Movement upstream of this peak causes a rapid degradation in performance as a result of ion recombination on hollow cathode surfaces.

An increase in the surface flux density of the ring magnets improves the confinement of both primary electrons and ions up to a surface flux density of ~ 1200 gauss. Increases in surface flux density beyond this value induce negligible additional improvement in the confinement of each species. Upstream movement of the central ring magnet in the discharge chamber introduces competing performance effects. It causes the volume of the ionizing plasma adjacent to the grids to increase while at the same time allowing increased ion losses to the discharge chamber walls in the region between the downstream and central magnet rings.

When a small diameter filament electron source is substituted for a hollow cathode the primary electron confinement and the extracted ion fraction characteristics of the ion source are unaffected but the baseline energy cost of producing plasma ions decreases by an amount equal approximately to the keeper voltage.

REFERENCES

1. Hiatt, J. M. and Wilbur, P. J., "Ring Cusp Discharge Chamber Performance Optimization," *Journal of Propulsion and Power*, Vol. 2, No. 5, Sept.-Oct. 1986, pp. 390-397.
2. Vaughn, J. A., "8 cm Dia. Ring Cusp Discharge Chamber Research," appears in "Advanced Electric Propulsion Research," NASA CR-182130, P. J. Wilbur, ed., pp. 1-52, Jan. 1988.
3. Arakawa, Y. and Wilbur, P. J., "Discharge Plasma Calculations in Cusped Ion Thrusters Using the Finite Element Method," Paper 88-079, 20th International Electric Propulsion Conference, Garmisch-Partenkirchen, West Germany, Oct. 3-6, 1988.
4. Brophy, J. R., "Ion Thruster Performance Model," NASA CR-174810, December, 1984.

APPENDIX A

The Effects of Ion Losses to Cathode or Anode Surfaces on Discharge Chamber Performance Parameters

When ions produced in a discharge chamber are lost to an anode or cathode surface, they cannot be measured because they cannot be distinguished from electrons that must flow to and from these surfaces to sustain the plasma discharge. Because of this a discharge chamber alteration that causes ions, which had been going to a chamber wall where they could be measured, to go instead to a cathode or anode surface would cause an apparent increase in both the extracted ion fraction f_p and the baseline plasma ion energy cost ϵ_p . In order to establish a relationship between the apparent and true values of these parameters the following definitions are offered:

ϵ_p • The true plasma ion energy cost (based on all ions produced whether they can be measured or not),

ϵ_p • The apparent or measured plasma ion energy cost (based only on the ion currents going to surfaces where measurements can be made),

J_B, J_W, J_S • Measured beam current, wall current, and screen current, respectively,

J_L • Ion loss current that cannot be measured (i.e. going to a cathode or anode surface),

f_p • The true extracted ion fraction (based on all ions produced),

f_B - The apparent or measured extracted ion fraction (based only on the ion current that can be measured).

Since the power being used to create the plasma ions is the same regardless of the accounting scheme used one can write

$$P = (J_B + J_S + J_W) e_P = (J_B + J_S + J_W + J_L) \hat{e}_P. \quad (A1)$$

Further, the true and apparent extracted ion fractions are given by:

$$\hat{f}_B = \frac{J_B}{(J_B + J_S + J_W + J_L)} \quad (A2)$$

and

$$f_B = \frac{J_B}{(J_B + J_S + J_W)}. \quad (A3)$$

Combining Eqs. A1, A2 and A3 to eliminate the currents one obtains

$$\frac{\hat{e}_P}{e_P} = \frac{\hat{f}_B}{f_B} \quad (A4)$$

This equation can be written in terms of the baseline plasma ion energy cost (e_P) using Eq. 5 and since the primary electron utilization factor C_0 is not affected by ion losses to the anode or cathode (see Fig. 9), the resulting equation can be simplified further to obtain

$$f_B = \frac{\hat{f}_B}{\hat{e}_P} e_P^*. \quad (A5)$$

Hence plasma ion losses to anode or cathode surfaces will induce increases in apparent extracted ion fraction and apparent baseline plasma ion energy cost that are proportional to each other.

Appendix B

IEPC-88-080

**An Approach to the Parametric Design
of Ion Thrusters**

Paul J. Wilbur

Colorado State Univ., Fort Collins, Colo., USA

John R. Beattie & Jay Hyman, Jr.

Hughes Research Labs, Malibu, Calif., USA

**DGLR/AIAA/JSASS 20th International
Electric Propulsion Conference**

October 3-6, 1988 / Garmisch-Partenkirchen, W. Germany

AN APPROACH TO THE PARAMETRIC DESIGN OF ION THRUSTERS[†]

Paul J. Wilbur^{††}
Colorado State University
Fort Collins, Colorado 80523, U.S.A.

and

John R. Beattie* and Jay Hyman, Jr.**
Hughes Research Laboratories
Malibu, California 90263, U.S.A.

ABSTRACT

A methodology that can be used to determine which of several physical constraints can limit ion thruster power and thrust, under various design and operating conditions, is presented. The methodology is exercised to demonstrate typical limitations imposed by grid system span-to-gap ratio, intragrid electric field, discharge chamber power per unit beam area, screen grid lifetime and accelerator grid lifetime constraints. Limitations on power and thrust for a thruster defined by typical discharge chamber and grid system parameters when it is operated at maximum thrust-to-power are discussed. It is pointed out that other operational objectives such as optimization of payload fraction or mission duration can be substituted readily for the thrust-to-power objective and that the methodology can be used as a tool for mission analysis.

INTRODUCTION

Ion thrusters are very attractive propulsion devices not only because of their high efficiency and high specific impulse capabilities but also because they afford designers and potential users a great deal of design and operational flexibility. It is generally recognized, however, that operational flexibility (e.g. throttleability) carries with it a price of a greater system complexity that may not be justifiable for many missions and it should be noted that design flexibility also has its unattractive aspects. It can for example conjure up impressions, particularly in the minds of those who do not work directly with ion thrusters, that they are too complex. In order to overcome this concern, the work described herein has been undertaken and a framework within which ion thruster performance and design information can be presented in a simple, easily understood way has been sought. It is hoped that this methodology can be used to facilitate communication, teaching, and an identification of the most productive areas for research and development in support of a variety of propulsion system objectives.

The development of this methodology might be pursued in terms of empirical relationships following the techniques used by Byers and Rawlin¹ and by Byers² but the desire to use it for teaching purposes coupled with the fact that basic models describing ion thrusters have become available since their work was published, has prompted us instead to base the development on basic physical models. Where parameters are required in this development to accommodate non-ideal behavior, every attempt has been made to use parameters that are physically meaningful, commonly used and theoretically based. The objective of this paper is to present a methodology that can be used to establish a link between thruster design, operational and mission

parameters in order to determine which of many possible performance-limiting phenomena will dominate in a particular situation. A second objective is to establish a technique that can be used to present information on this subject in a manner that is both easy to visualize and understand.

THEORY

The canonical design variables associated with an ion thruster are the specific impulse at which it operates (I_{sp}), its beam area (A_b) and its beam power (P_b). Generally, one would want to prescribe the specific impulse and beam area of a device and then determine the beam power at which it could be operated under a given set of design, operational and mission constraints, so in this development specific impulse and beam area will be treated as independent variables and beam power will be treated as the dependent variable.

Examples of physical constraints which have been found to limit the beam power at which a thruster can operate include:

Grid system span-to-gap ratio. This constraint is determined by ones ability to hold grids close together in an environment of thermally induced distortion and in some situations significant electrostatic attraction. It is influenced greatly by mechanical design and fabrication considerations and while a value of 600 might be considered a reasonable limit for conventional circular grids, the use of intragrid supports or non-circular (e.g. annular or rectangular grids) could facilitate substantial increases above 600.

Intragrid electric field. Excessively high electric fields between the screen and accelerator grids of a thruster result in electrical breakdown and an inability to extract an ion beam. This limit is influenced by such factors as the surface finish and uniformity of the intragrid spacing and typical values in operating thrusters have generally been about 2 kV/mm although much higher values have been reported.⁴

Discharge power per unit beam area. This is actually a heat transfer limit that is imposed because components such as magnets, anodes or grids can overheat if the heat removal rate is inadequate. This constraint could be formulated in terms of specific heat transfer limitations for particular components but for the illustrative purposes of this paper, it will be assumed that the allowable discharge power scales directly with beam area and that a limit in the range 15 to 30 kW/m² is reasonable.

[†]Work supported in part by NASA Grant NGR-06-002-112.

^{††}Professor, Dept. of Mechanical Engg., Member AIAA.

*Head, Plasma Sources Section, Ion Physics Dept., Member AIAA.

**Manager, Ion Physics Dept., Member AIAA.

Screen grid lifetime. The lifetime of the screen grid as well as other components exposed to the discharge plasma is limited by the process of ion-induced sputter erosion. Typically grids and other components have been designed to have lifetimes in the range of 10^4 to 2×10^4 hours. These lifetimes are influenced by the materials and ions involved and by the discharge voltage.

Accelerator grid lifetime. The accelerator grid is exposed to small currents of high energy, charge-exchange ions that limit its lifetime through sputter erosion. This grid is typically designed to have a lifetime in the same 10^4 to 2×10^4 hr range that the screen grid has.

The above list of constraints on ion thruster design is not exhaustive, but they represent constraints that have been encountered and they can be used for purposes of illustration.

A trade-off exists between the propellant and power requirements for an ion thruster and for this reason a preferred operating point or operational objective exists. The one selected influences the severity of each of the design constraints identified above. Once an objective that requires operation, for example, at the point where the thruster will produce maximum thrust per unit input power or maximum payload fraction on a prescribed mission has been identified, one can define the extent of the power limits cited in the preceding paragraphs. For the purposes of this study it will be assumed that the thruster is to be operated at the point of maximum thrust-to-power, but it should be recognized that this additional input, which could be much more complex, might come for example from an algorithm that optimizes a mission objective.

Mathematical Development

The beam power (P_B) produced by an ion thruster is expressed most simply as the product of beam current (J_B) and beam (or net accelerating) voltage (V_B).

$$P_B = J_B V_B \quad (1)$$

The beam current in this equation is related to the peak current density being extracted through the grids (j_{max}) and the beam area (A_B) through the beam flatness parameter (BF) which is defined as the ratio of average-to-peak ion beam current density.

$$BF = J_B / (j_{max} A_B) \quad (2)$$

It is noted that the flatness parameter can be calculated for a given discharge chamber using the finite element technique developed by Arakawa.

The maximum current density capability of a grid set is determined by space-charge limitations which may be described approximately using the one-dimensionally based Child-Langmuir law.

$$j_{max} = \frac{4\epsilon_0}{9} \left(\frac{2e}{m_i} \right)^{1/2} \frac{V_T^{3/2}}{d^2} \phi_s \psi_e \quad (3)$$

The permittivity of free space (ϵ_0), the electron charge (e) and the ion mass (m_i) appearing in this equation are known constants and the total accelerating voltage (V_T) and the screen grid transparency to ions (ϕ_s) are at the control of the designer and/or operator. The ion current density enhancement factor (ψ_e) is a factor that will be set equal to unity for the purposes of this paper, but it could take on values greater than unity to account for the increased current density capabilities of grids when ions approach the screen grid plasma sheath at non-zero velocities or high energy electrons are injected into the sheath to mitigate

the space-charge limitations that develop there. The final factor in Eq. 3, the effective ion acceleration length (l), is the one that is limited by span-to-gap and electric field considerations and the imposition of these constraints will be considered in detail next. It will be assumed that the value of l is the same for each aperture set over the entire grid surface for this development.

The total accelerating voltage that appears in Eq. 3 can be eliminated in favor of the beam voltage by introducing the net-to-total accelerating voltage ratio (R)

$$R = V_B / V_T \quad (4)$$

The beam voltage can be related to the specific impulse (I_{sp}) by recognizing that the specific impulse is defined as the thrust (F) per unit weight flowrate of propellant (\dot{m}_{g0})

$$I_{sp} = F / \dot{m}_{g0} \quad (5)$$

that the thrust is given by the momentum equation

$$F = [\dot{m}_{g0}] [U F_c a] \quad (6)$$

and that the ion exhaust velocity (U) is related to the beam voltage through the conservation of energy expression

$$V_B a = m_i U^2 / 2 \quad (7)$$

In Eq. 6 the product of propellant mass flowrate (\dot{m}) and propellant utilization efficiency (η_u), which is the first bracketed term, represents the flowrate of thrust producing (high velocity) propellant and the second bracketed term represents the effective jet velocity of the beam ions along the thruster axis. This second term includes two thrust correction factors, one (F_c) that reflects the fact that many ions will emerge from the grid system on divergent trajectories and a second (a) that accounts for the fact that Eq. 7 describes the velocity of singly charged ions only when in fact some multiply charged ions will generally be produced and extracted.

Combining Eqs. 5, 6 and 7 the desired expression for beam voltage in terms of specific impulse is obtained

$$V_B = \frac{m_i}{2a} \left(\frac{I_{sp} \dot{m}_{g0}}{\eta_u F_c a} \right)^2 \quad (8)$$

and this may be combined with Eqs. 1 through 4 to obtain

$$P_B = \frac{\epsilon_0 BF A_B \phi_s \psi_e}{9 l^2 R^{3/2}} \left(\frac{m_i}{a} \right)^2 \left(\frac{I_{sp} \dot{m}_{g0}}{\eta_u F_c a} \right)^5 \quad (9)$$

Equation 9 defines the maximum power constraint associated with the ion extraction process for an ion thruster as a function of its beam area and the specific impulse at which it is to operate. Two physical constraints, one associated with the allowable span-to-gap ratio and the other with the maximum allowable electric field between the grids, actually evolve from this equation through the effective ion acceleration length (l). The fact that propellant utilization appears in the equation also serves as a reminder that an operational objective must be defined before unique limiting values of beam power can be computed as a function of specific impulse and beam area for these two physical constraints.

Span-to-Gap Ratio Constraint

The allowable span-to-gap ratio (N) associated with traditional grid sets is the grid diameter-to-spacing ratio. In order to accommodate non-circular beam cross sections, however, this ratio will be

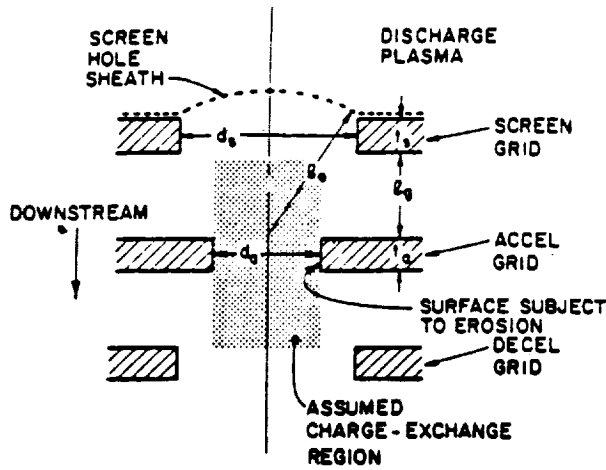


Fig. 1. Aperture System Geometry

defined here using an equivalent beam diameter and the grid separation will be given by the expression

$$l_g = \frac{\sqrt{A_B/\pi}}{N} \quad (10)$$

The preferred ion acceleration length for use in Eq. 9 (which is based on one-dimensional theory) would be the one that would yield the beam current density actually extracted from screen/accel grid aperture pairs in what is really a two-dimensional process. One value of l that should come close to doing this is illustrated in Fig. 1 and examination of the geometry of this figure suggests l is related to the grid separation distance given by Eq. 10 through the expression

$$l_g = \sqrt{(t_s + l_g)^2 + d_s^2/4} \quad (11)$$

It should be noted here that Eq. 11 differs from the traditional equation for l used to compute perveances in that it accounts for the screen grid thickness (t_s). If the screen grid thickness is left out of this expression, the implication is that the screen hole sheath positions itself close to the downstream edge of the screen grid. Aston¹⁰ has shown, however, that this sheath tends to position itself near the upstream edge of the hole under normal operating conditions and Eq. 11 is therefore considered correct.

Equations 9, 10 and 11 can be combined to define the maximum beam power at which a thruster with a beam area A_B and a span-to-gap ratio N can be operated at prescribed specific impulses provided an operational objective, a screen grid thickness (t_s) and a screen hole diameter (d_s) are specified. For this illustrative study these latter two parameters have been defined by specifying a grid separation-to-screen hole diameter ratio (l/d_s) and screen grid thickness of unity and 0.0065 μ respectively.

Electric Field Constraint

In order to prevent electrical breakdown between grids it is presumed that a limiting electric field E cannot be exceeded. Assuming a uniform grid spacing, this may be expressed mathematically using the expression

$$l_g = \frac{V_T}{E} = \frac{V_B}{E} \quad (12)$$

Combining this with Eqs. 9 and 11, an operational objective, a screen grid thickness and a screen hole diameter, the beam power/beam area/specific impulse surface limited by electrical breakdown considerations is defined.

Discharge Chamber Thermal Constraint

If the power required to operate a discharge chamber becomes too great, such failures as those associated with magnet, screen grid or anode overheating could occur. Of course the allowable discharge power would scale with thruster size and a review of limiting discharge powers on thrusters having various diameters has suggested that it is probably the discharge power per unit beam area (P_D/A_B) that defines this constraint.

The discharge power can be expressed in terms of the energy cost of a beam ion (ϵ_B) through the equation

$$\frac{P_D}{A_B} = \frac{\epsilon_B J_B}{A_B} \quad (13)$$

Combining Eqs. 1, 8 and 13 one can obtain

$$P_B = \left(\frac{P_D}{A_B} \right) \left(\frac{A_B}{\epsilon_B} \right) \left(\frac{m_i}{2e} \right) \left[\frac{I_{sp} \epsilon_{so}}{\eta_u F_c a} \right]^2 \quad (14)$$

The beam ion energy cost appearing in this equation can be computed using Brophy's model¹¹ in the form

$$\epsilon_B = \frac{\epsilon_p^*}{f_B} \left[1 - \exp(-B_0(1-\eta_u)) \right]^{-1} + \frac{f_c V_D}{f_B} \quad (15)$$

where the baseline plasma ion energy cost (ϵ_p^*) can be computed when the propellant and discharge voltage (V_D) are prescribed¹¹ and the extracted ion fraction (f_B) and the fraction of the ions produced that go to cathode potential surfaces (f_c) can be determined when the magnetic field and electron source location are specified. The parameter B_0 is given by

$$B_0 = \frac{1}{2} C_0 = \frac{A_B \sigma' l}{m_i V_0 \phi_0} \left(\frac{m_i}{A_B} \right) \quad (16)$$

where the primary electron utilization factor (C_0), the primary electron/propellant atom total inelastic collision cross section (σ'), the primary electron containment length (l), the propellant atom thermal velocity (V_0) and the transparency of the grids to neutral atoms (ϕ_0) may be assumed constant for a particular propellant and discharge voltage. An expression for the propellant flowrate per unit beam area needed in Eq. 16 can be obtained by combining the definition of propellant utilization efficiency

$$\eta_u = \frac{J_B m_i}{\dot{m} e} \quad (17)$$

with Eqs. 2 through 7 to obtain

$$\frac{\dot{m}}{A_B} = \frac{2 \epsilon_p^* F_c \phi_0 \eta_u}{9 \eta_u^2 l^2 R^{3/2}} \left(\frac{m_i}{e} \right)^2 \left(\frac{I_{sp} \epsilon_{so}}{F_c a} \right)^3 \quad (18)$$

Equations 14, 15, 16 and 18 when combined with an operational objective yield the beam power/beam area/specific impulse surface that defines the discharge power per unit beam area constraint.

Screen Grid Lifetime Constraint

Although the screen grid is assumed to be the life limiting component subjected to sputter erosion in this paper, additional constraints pertaining to other components that are subjected to ion bombardment could impose similar constraints. They would be incorporated into the analysis in the same way as the one developed here for the screen grid. If the screen grid lifetime is considered to have expired when a fraction γ of its initial thickness t_s has been sputtered away then this lifetime will be given by

$$r_s = \frac{\rho N_A \tau_s c_s}{\left[j_+ s_s^+(V_D) + 0.5 j_{++} s_s^{++}(2V_D) \right] M} \quad (19)$$

where ρ and M are the density and molecular weight of the grid material, N_A is Avagadro's number, j_+ and j_{++} are the singly and doubly charged ion current densities striking the grid and $s_s^+(V_D)$ and $s_s^{++}(2V_D)$ are the sputtering yields of the grid material for singly and doubly charged ions evaluated respectively for ions with energies equal to the discharge voltage and twice the discharge voltage. Recognizing that the grid will sputter most rapidly at the point of maximum current density ($j_+ = j_{++}$) Eqs. 1, 2 and 8 can be combined with Eq. 19 to obtain

$$P_B = \frac{n_i \rho N_A \tau_s c_s I F A_B}{2 r_s M \left[s_s^+(V_D) + 0.5 \frac{j_{++}}{j_+} s_s^{++}(2V_D) \right]} \left[\frac{I_{sp} E_{so}}{\eta_u F c a} \right]^2 \quad (20)$$

The doubly-to-singly charged ion current density ratio (j_{++}/j_+) appearing in this equation is a strong function of discharge operating conditions and is given by

$$\frac{j_{++}}{j_+} = \frac{2 \left[\frac{Q_0^{++} + \frac{n_D}{n_H} P_0^{++}}{Q_0^+ + \frac{n_D}{n_H} P_0^+} \right] + 0.83 \left(\frac{v_D}{v_B} \right) \left(\frac{\phi}{\phi_s} \right)}{\left[\frac{Q_0^{++} + \frac{n_D}{n_H} P_0^{++}}{Q_0^+ + \frac{n_D}{n_H} P_0^+} \right] \frac{\eta_u}{1-\eta_u}} \quad (21)$$

Some simplification of this equation is generally possible because the first term is negligible at typical discharge chamber electron temperatures and energies. In Eq. 21 v_D and v_B are the Bohm and neutral atom thermal velocities, ϕ_s and ϕ are the transparencies of the grids to ions and neutral atoms and Q_0^+ , P_0^+ and etc. are the rate factors associated with production of the various ionic species. The primary-to-Maxwellian electron density ratio (n_p/n_H) appearing in Eq. 21 is given by

$$\frac{n_p}{n_H} = \left[\left[\frac{0.13 e \frac{v_D}{v_B} \phi_s \phi}{v_p v_D f_B \sigma'_0} \right] \left(\frac{A_B}{A} \right) \left(\frac{A_B}{A} \right) \frac{1}{1-\eta_u} \right]^{-1} \quad (22)$$

In this equation, the primary electron velocity (v_p) is determined by its energy which is assumed in turn to be equal to the discharge voltage. The discharge chamber volume-to-beam area ratio (V/A_B) is simply the discharge chamber length which may be assumed to be relatively insensitive to beam area (e.g. $V/A_B = 0.1 + 0.1 [1 - \exp(-10A_B)]$ has been used for the examples presented here). The final expression needed to define the screen grid lifetime constraint is one for the propellant mass flowrate per unit beam area. It is obtained by combining Eqs. 1, 8 and 17.

$$\frac{\dot{m}}{A_B} = \frac{2 P_B \eta_u}{A_B} \left[\frac{F c a}{I_{sp} E_{so}} \right]^2 \quad (23)$$

Equations 20 through 23 can be solved for the beam power/beam area/specific impulse surface that defines the screen grid lifetime constraint when an operational constraint is specified and design definitions associated with the chamber (e.g., propellant, discharge voltage, etc.) have been made.

Accel Grid Lifetime Constraint

For a three-grid ion optics system where sputtering on the barrel (interior surface) region of the accel grid holes dominates the erosion of the grid, the change in accel hole diameter (d_a) per unit time is given by

$$\frac{d(d_a)}{dt} = \frac{S_a j_{max} n_o \sigma_{ce} \psi_{ca} f_a M}{\rho N_A \rho \pi d_a c_s} \quad (24)$$

In this equation S_a is the sputter yield of the accelerator grid material at the prevailing charge exchange ion kinetic energy, n_o is the neutral atom density in the charge exchange reaction region, ψ_{ca} is the volume of this region, f_a is a factor that describes the extent to which these ions are focused or distributed along the barrel region and c_s is the accelerator grid thickness. For a two-grid optics set where sputtering on the downstream surface of the accel grid dominates, a similar equation is used but for the example being considered here, the three-grid equation (Eq. 24) will be used exclusively.

The neutral atom density in the charge exchange region is given approximately by the expression

$$n_o = \frac{\Delta j_B (1-\eta_u)}{A_B \phi_o v_o s} \quad (25)$$

If the allowable change in diameter is Δd and r_a is the desired lifetime then the integrated form of Eq. 24 may be combined with Eqs. 1, 2, 8 and 25 to obtain

$$P_B = \frac{A_B n_i}{A} \left[\frac{I F \phi_o v_o N_A \rho c_s (\Delta d/d_a)}{r_a s_a (1-\eta_u) \sigma_{ce} f_a M I_{sp}} \right]^{1/2} \left[\frac{I_{sp} E_{so}}{\eta_u F c a} \right]^2 \quad (26)$$

In order to compute beam power as a function of beam area and specific impulse using this equation the volume of the charge exchange region has been assumed to be equal to that of the cylinder shown in Fig. 1 with a diameter equal to that of the accel grid aperture (d_a) and a length twice the grid separation distance (l). In addition the ratio of accel grid thickness to grid separation distance (c_s/l) has been assumed to be constant.

Operational Objective

It is necessary to define an operational objective for a thruster in addition to the various physical constraints imposed on it in order to define the thruster discharge chamber operating point, i.e., the propellant utilization efficiency and discharge power at which the thruster should be operated. This can be done for example by defining a mission of interest, which might be characterized by a mission time and characteristic velocity or a complex mission algorithm; computing the masses of the system elements (power plant, propellant, payload, etc.) and determining the propellant utilization efficiency operating point at which the associated payload fraction is maximized. The optimum propellant utilization operating point has been selected in this study so the thruster operates at the maximum thrust-to-power condition. This condition is defined by combining Eqs. 1, 5, 6, 7, and 17 with the expression for thruster electrical efficiency which is given by

$$\eta_e = \frac{P_B}{P_T} = \frac{j_B v_B}{j_B v_B + \Sigma P} \quad (27)$$

In this equation P_T is the total thruster power and ΣP is the sum of the powers needed to generate ions and to sustain thruster temperatures, propellant flow-rates and neutralizer operation (i.e., the power loss term). Frequently the dominant power loss is the discharge power required to produce the

ions and it can be expressed in terms of the energy cost of a beam ion ($P_D = J_B e_B$). Assuming the discharge power does dominate the losses, Eq. 27 can be rewritten as

$$\eta_e = \frac{V_B}{V_B + e_B} \quad (28)$$

and this equation can be combined with those identified above to obtain the expression for thrust-to-total power.

$$\frac{F}{P_T} = \frac{I_{sp} g_{00}}{\eta_u} \left[\frac{1}{\frac{1}{2} \left(\frac{I_{sp} g_{00}}{\eta_u F_c a} \right)^2 + \frac{e_B e}{m_i}} \right] \quad (29)$$

By seeking the propellant utilization that maximizes this equation at each specific impulse, operation at maximum thrust-to-power is realized for each thruster beam area and physical constraint condition.

RESULTS

The analysis technique outlined in the preceding section can be used to investigate the effects of a wide variety of design and operational parameters on the power and thrust capabilities of ion thrusters. Because the purpose of this paper is to demonstrate the capability of the methodology involved rather than to draw conclusions based on an exhaustive study conducted using it, one set of typical values of thruster parameters has been selected for use in the analysis. The values used are listed in Table I and while they are considered to be typical of ion thrusters in general, they do not represent any particular thruster. The rate factors used in the analysis are based on an assumed Maxwellian electron temperature of 5 eV and a primary electron energy, which is consistent with the discharge voltage (30 eV).

Table I. Thruster Parameters Used in Example Study in the Order of Their Appearance

Parameter/Property	Symbol	Value Used
Ion Beam Flatness	IF	0.5
Ion Current Density Enhancement Factor	ψ_e	1.0
Screen Grid Transparency to Ions	ϕ_s	0.7
Grid System Transparency to Neutral Atoms	ϕ_o	0.16
Ion Mass (Xenon)	m_i	2.2×10^{-25} kg
Net-to-Total Accelerating Voltage Ratio	R	0.5
Beamlet Divergence Thrust Factor	F_c	1.0
Multiply Charged Ion Thrust Factor	α	1.0
Screen Grid Thickness	t_s	5×10^{-4} m
Grid Separation to Screen Hole Diameter Ratio	l_g/d_s	1.0
Baseline Plasma Ion Energy Cost	e_p	50 eV/ion
Extracted Ion Fraction	f_B	0.5
Fraction of Plasma Ions Going to Cathode Potential Surfaces	f_c	0.3

Table I (continued).

Parameter/Property	Symbol	Value Used
Discharge Voltage	V_D	30 V
Total Electron-Atom Inelastic Collision Cross Section ^{14, 16}	σ'_o	7.4×10^{-20} m ²
Primary Electron Containment Length	l^*	3.5 m
Neutral Atom Thermal Velocity	v_o	290 m/sec
Allowable Screen Grid Erosion Fraction	γ_s	0.5
Ionization Rate Factors for 5 eV Temperature Maxwellian Electrons ¹⁸	Q_o^+	7.1×10^{-15} m ³ /sec
	Q_o^{++}	5.1×10^{-16} m ³ /sec
Ionization Rate Factors for 30 eV Energy Primary Electrons ¹⁸	P_o^+	1.3×10^{-13} m ³ /sec
	P_o^{++}	2.5×10^{-14} m ³ /sec
Sputter Yields for Molybdenum Screen Grid for Singly and Doubly Charged Ions ¹⁷	S_s^+	2×10^{-6}
	S_s^{++}	1.5×10^{-3}
Sputter Yield for Accel Grid ¹⁷	S_a	1.0
Charge Exchange Cross Section ¹⁴	σ_{ce}	3×10^{-19} m ²
Accel Grid Thickness-to-Grid Separation Ratio	t_a/l_g	0.3
Allowable Accel Grid Erosion	$\Delta d_a/d_a$	0.5
Charge Exchange Ion Focusing Factor	f_a	0.25

If one prescribes a thruster with a beam area of 0.2 m² and calculates the beam power limits for each of the physical constraints described in the preceding section with the objective of operation at maximum thrust-to-power, the curves of Fig. 2 are obtained for the values of the constraints cited in the figure. For each constraint, operation below and to the right of the associated curve assures operation that does not violate the constraint. Hence in the case of Fig. 2 the 600 span-to-gap constraint limits the power that can be extracted up to a specific impulse of ~3000 sec and then the

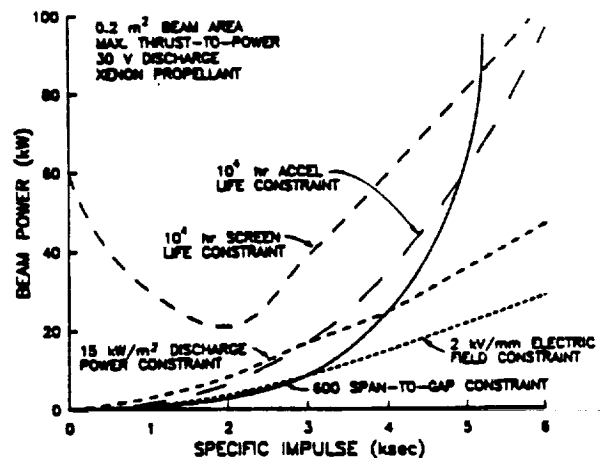


Fig. 2. Typical Power Constraint Curves - 0.2 m² Beam Area (Span-to-Gap and Intragrid Electric Field Limiting)

2 kV/mm electric field constraint becomes limiting. For the particular parameters associated with the other constraints, Fig. 2 indicates none of the other constraints (discharge power, screen grid life, or accel grid life) become limiting at any specific impulse up to 6000 sec. The fact that span-to-gap is limiting at low specific impulses while electric field becomes limiting at higher ones is in qualitative agreement with experimental observations.

If the grids were designed so the electric field limit could be increased to 4 kV/mm and the other constraints were held fixed at the values of Fig. 2, then the data of Fig. 3 are generated. They suggest the 600 span-to-gap limit would prevail to ~4000 sec. specific impulse and the discharge power per unit beam area limit of 15 kW/m² would become constraining beyond that point. Increasing the electric field limit has in this case allowed the beam power at 4000 sec I_{sp} to increase from ~15 kW (Fig. 2) to ~25 kW (Fig. 3) and at 6000 sec from ~27 kW (Fig. 2) to ~45 kW (Fig. 3). If, on the other hand, it were necessary to have screen and accel grid lifetimes of 2×10^4 hr then the accelerator grid lifetime would become limiting over the I_{sp} range from about 3500 sec to 4500 sec as the data of Fig. 4 show. In this case the power at 4000 sec I_{sp} would be limited by accel grid lifetime considerations to ~21 kW.

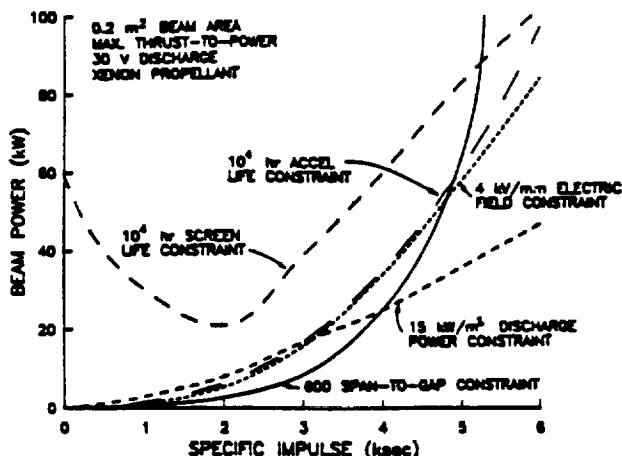


Fig. 3. Typical Power Constraint Curves - 0.2 m² Beam Area (Span-to-Gap and Discharge Power Limiting)

If the beam power limits imposed by the constraints being considered as functions of both beam area and specific impulse are sought rather than holding beam area constant, then beam power/beam area/specific impulse surfaces like those shown in Fig. 5 are generated. These surfaces define power limits associated with each constraint indicated and they are all plotted on the same scale, namely the one defined in Fig. 5a. Operation is permitted at any point beneath the surface associated with a particular constraint, but not above it. All of these surfaces behave as one would expect with the beam powers being lowest for low beam areas and low specific impulses except the one associated with screen grid lifetime. The high allowable power observed at low specific impulses for the screen life constraint seems unusual. It is a consequence of operation at maximum thrust-to-power which implies a low propellant utilization at low specific impulses (Eq. 29). Low propellant utilizations in turn imply low doubly-to-singly charged ion current densities (Eq. 21) and hence high allowable beam powers (Eq. 20).

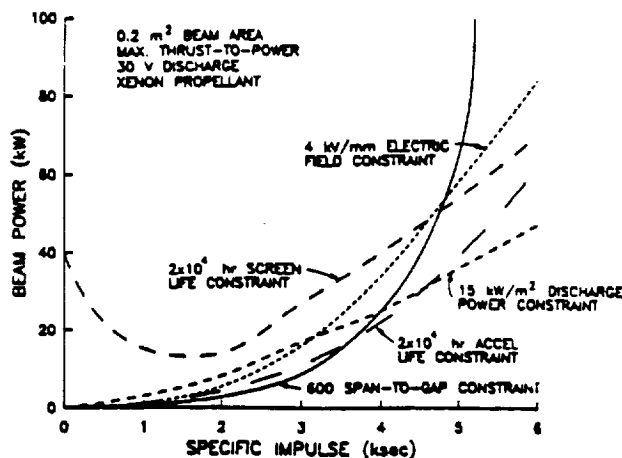


Fig. 4. Typical Power Constraint Curves - 0.2 m² Beam Area (Span-to-Gap, Discharge Power and Accel Grid Lifetime Limiting)

When all constraints shown in Fig. 5 are applied and the overall limiting surface is identified, the one shown in Fig. 6 is obtained. As the labels on this surface indicate, the span-to-gap and electric field constraints represent the most restrictive limitations (span-to-gap at low specific impulses and electric field at higher ones) over the beam area range from zero to 1 m².

If one defines a mission along with powerplant and power processor specific mass parameters and then imposes the power limits defined by all of the constraints associated with the data in Fig. 5, payload fractions can be computed as a function of beam area and specific impulse. Figure 7 shows the payload fraction surface computed when the most restrictive of these constraints are applied for a 10⁴ m/sec mission to be accomplished in 0.67 year when the powerplant and power conditioner are characterized by the specific masses and the power conditioner efficiency values cited on the figure. The payload fraction reaches a relatively flat peak at a value of 55 percent when the specific impulse is near 4500 sec for all but the smallest beam areas. The payload fraction peak in Fig. 7 is seen to be very broad, so the thruster could be operated at specific impulses ranging from ~3000 to 6000 sec and deliver about the same payload fraction.

The thrust at which the ion thruster operates can also be computed as a function of beam area and specific impulse by using Eqs. 28 and 29 in conjunction with the most restrictive beam power constraining surface data (Fig. 6). Figure 8 shows how the thrust associated with the constraints defined in Fig. 5 would vary as a function of beam area and specific impulse.

If the electric field constraint is increased to 4 kV/mm, the results of Fig. 3 showed that the discharge power per unit beam area became the power-limiting surfaces at high specific impulses when the beam area was 0.2 m². The effect of introducing this new electric field constraint for beam areas ranging from zero to 1.0 m² is shown in Fig. 9. Comparison of the data in Figs. 6 and 9 shows that increasing the electric field limit facilitates a substantial increase in beam power at high beam area and specific impulse values (250 kw vs. 150 kw).

If the grid lifetime constraints are tightened by requiring 20,000 hr operating times, then the accel grid lifetime constraint identified in Fig. 10 limits the beam power in the moderate specific impulse-low beam area regime. Away from this region

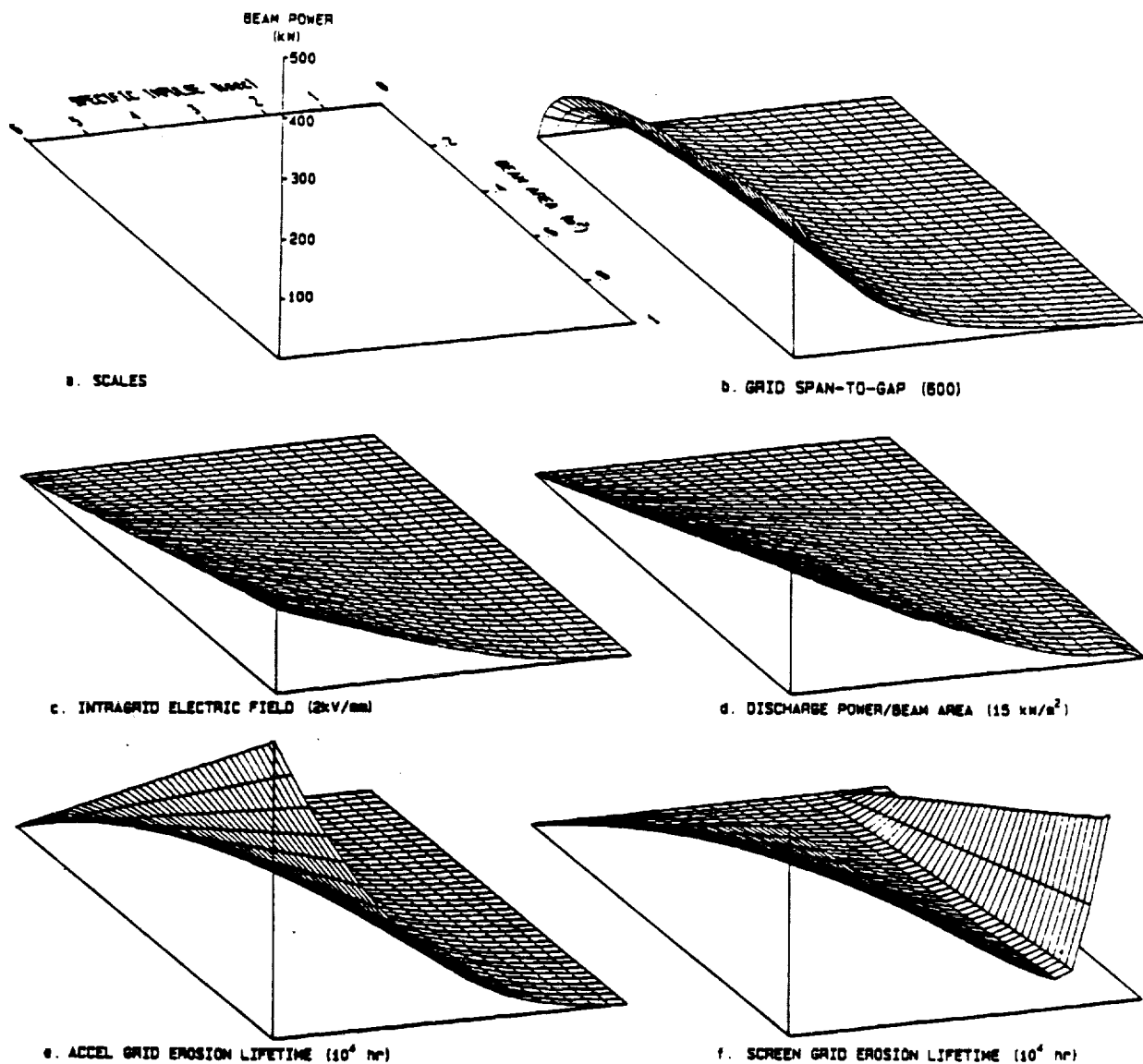


Fig. 5. Typical Power Constraining Surfaces

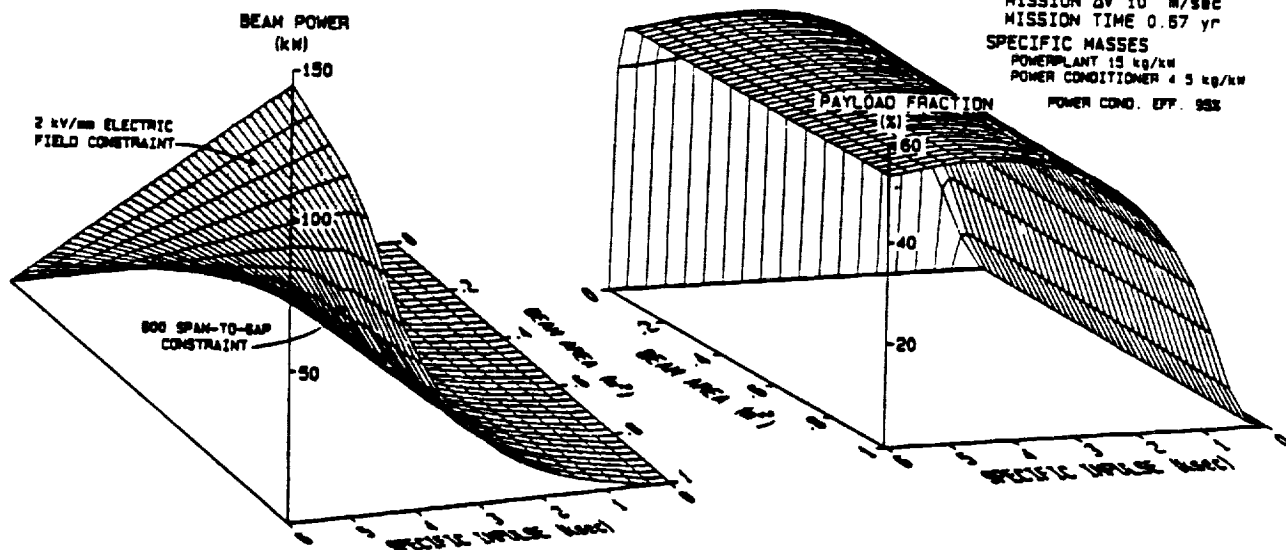


Fig. 6. Typical Overall Power Constraining Surface (Span-to-Gap and Intragrid Electric Field Limiting)

Fig. 7. Typical Payload Fraction Surface

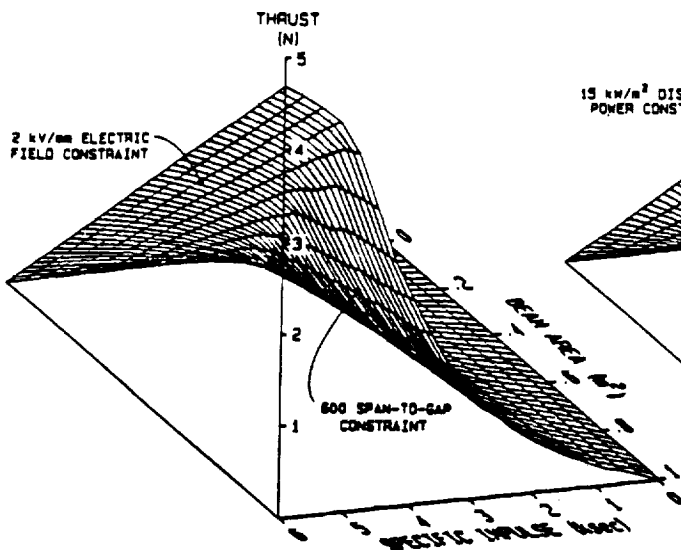


Fig. 8. Typical Thrust Surface

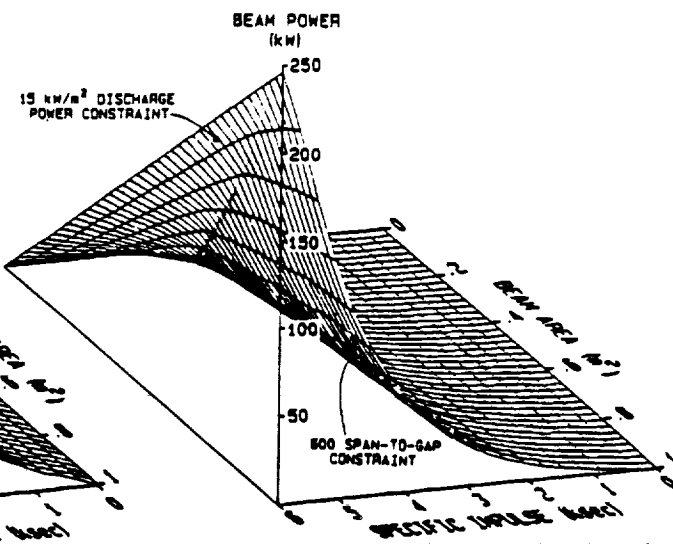


Fig. 9. Typical Overall Power Constraining Surface (Span-to-Gap and Discharge Power Limiting)

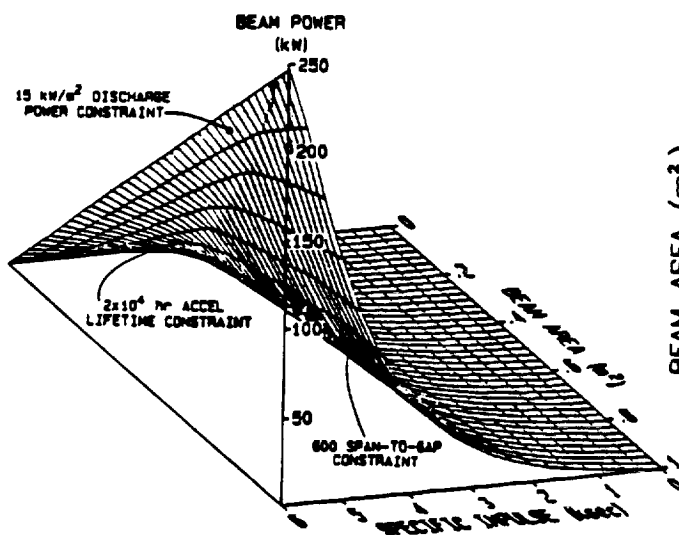


Fig. 10. Typical Overall Power Constraining Surface (Span-to-Gap, Discharge Power and Accel Grid Life Limiting)

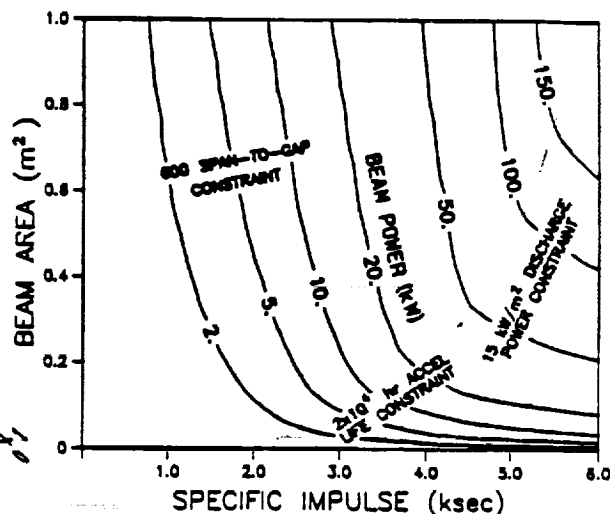


Fig. 11. Constant Power Contour Diagram (Span-to-Gap, Discharge Power and Accel Grid Life Limiting)

the power limit is unchanged from the values presented in Fig. 9.

The three-dimensional plots shown in Figs. 5 through 10 are useful to illustrate qualitative behavior, but they are difficult to use as a source of quantitative information. Quantitative information can be presented better in the form of an equal beam power contour plot like the one in Fig. 11. This figure, which presents the same data as that in Fig. 10, clearly indicates the beam power limit at any beam area and specific impulse point. It also shows the constraint that is preventing operation at higher power levels at each beam area and specific impulse. Similar figures could, of course, also be generated to show the limiting values of thrust and payload fraction as a function of thruster beam area and specific impulse.

FUTURE DIRECTIONS

The intent of the preceding discussion has been 1) to present a methodology and framework within which gross parameters describing ion thruster behavior could be used to predict ion thruster per-

formance limits, 2) to cite references that describe how these gross parameters can be computed, and 3) to suggest how results obtained from the analysis might be presented in a readily understood format. The analysis should, however, not be considered fully developed. The following statements describe changes that might be introduced to improve the analysis.

1) The beamlet divergence (thrust) factor (F_c), the grid separation-to-screen hole diameter ratio (l/d) and the net-to-total acceleration voltage ratio (R) have all been treated as constants in the cases presented. These quantities are, however, variable and they are related to each other. One could therefore use data like those in Ref. 19 to determine values of F_c for prescribed values of l/d and R or one could incorporate additional operational objectives that would assure the parameters are selected to maximize a thruster parameter of interest.

2) The screen and accel grid thicknesses (t_s and t_a respectively) have been treated as constants, and depending on the beam geometrical cross section

it may be that they would be better represented as functions of beam area. For example, a functional relationship between these thicknesses and the beam area based on mechanical deformation considerations might be desirable.

3) Although some variation in discharge chamber plasma properties has been allowed in the development of the screen life constraint, more can be done in modeling the other constraints to reflect the effects of changes in Maxwellian electron temperature, primary and Maxwellian electron densities, the baseline plasma ion energy cost (ϵ_0) and the doubly-charged ion thrust factor (α) induced by changes in propellant utilization and discharge voltage. It is noted that the physically based models needed to do this are available.

4) The grid spacing has been assumed constant across the entire intragrid region. The effects of variable spacing induced by grid thermal distortion and electric field induced deflection forces may cause this spacing to change as a function of location on the grids. This in turn will influence the ion extraction and electrical breakdown capabilities of the grids.

Finally, it is noted that many of the parameters needed to model the plasma discharge and ion extraction phenomena involved in this analysis can be computed from basic principles. The noteworthy exception to this is the primary electron containment factor f . It can be inferred from discharge chamber tests, but a model that can be used to calculate it for a discharge chamber having prescribed dimensions and magnetic field characteristics is needed. Additional work may also be needed to describe more accurately the energy of primary electrons extracted from a hollow cathode as a function of discharge voltage.

CONCLUSIONS

A methodology that can be used to determine the maximum power level at which an ion thruster can be operated and a framework within which the resultant data can be presented has been developed. Physical constraints associated with the allowable grid span-to-gap ratio, the intragrid electric field, the discharge power per unit beam area and the screen and accel grid lifetimes have been identified as power (or thrust) limiting and relationships that quantify each of the constraints have been presented. When the methodology is exercised for a thruster operating on xenon at propellant utilization efficiencies that induce maximum thrust-to-power with constraints of 600 span-to-gap ratio, 2 kV/mm electric field, 15 kW/m² discharge power per unit beam area and 10⁴ hr screen and accel grid lifetime requirements, the span-to-gap constraint is shown to be limiting at low specific impulses and the electric field is shown to be limiting at higher ones. If the electric field limit is increased to 4 kV/mm, the discharge power becomes limiting at high specific impulses and if the grid lifetime requirement is increased to 2 x 10⁴ hr then accel grid erosion can become limiting at intermediate specific impulses. Although the input data have not been selected so results predicted in the analysis can be compared to experimental observations, the general trends appear to be consistent with generally observed experimental trends.

REFERENCES

1. Byers, D. C. and V. K. Rawlin, "Critical Elements of Electron-Bombardment Propulsion for Large Space Systems," *Jour. of Spacecraft and Rockets*, V. 14, Nov. 1977, pp. 648-654.
2. Byers, D. C., "Characteristics of Primary Electric Propulsion System," AIAA Paper 79-2041, Oct. 31-Nov. 2, 1979.
3. Kaufman, H. R., "Technology of Electron-Bombardment Ion Thrusters," *Advances in Electronics and Electron Physics*, V. 36, Ed. L. Marton, Academic Press, New York, 1974, pp. 265-373.
4. Lovang, D. C., "Ion Extraction Capabilities of Two-Grid Accelerator Systems," NASA Contractor Report CR-174621, Feb. 1984.
5. Arakawa, Y. and P. J. Wilbur, "Discharge Plasma Calculations in Cusped Ion Thrusters Using the Finite Element Method," Paper 88-079, 20th AIAA/DGLR/JSAS International Electric Propulsion Conference, Oct. 3-6, 1988, Garmisch-Partenkirchen, W. Germany.
6. Langmuir, I., "The Interaction of Electron and Positive Ion Space Charges in Cathode Sheaths," *Phys. Rev.*, V. 33, 1929, p. 954.
7. Feng, Y. and P. J. Wilbur, "Enhancement of Ion Beam Currents through Space-Charge Compensation," *J. Appl. Phys.*, V. 54, No. 11, Nov. 1983, pp. 6113-6118.
8. Poeschel, R. L. and J. R. Beattie, "Primary Electric Propulsion Technology Study," Final Report on Contract NAS 3-21040, pp. 127-154.
9. Kaufman, H. R., "Accelerator-System Solutions for Broad-Beam Ion Sources," *AIAA Jour.*, V. 15, July 1977, pp. 1025-1034.
10. Aston, G. and P. J. Wilbur, "Ion Extraction from a Plasma," *J. Appl. Phys.*, V. 52, April 1981, pp. 2614-2626.
11. Brophy, J. R., "Ion Thruster Performance Model," NASA CR-174810, Dec. 1984.
12. Bohm, D., "Minimum Ionic Kinetic Energy for a Stable Sheath," in *Characteristics of Electrical Discharges in Magnetic Fields*, A. Guthrie and R. K. Wakerling, eds., McGraw-Hill, Inc., New York.
13. Wilbur, P. J. and H. R. Kaufman, "Double Ion Production in Argon and Xenon Ion Thrusters," *Jour. of Spacecraft and Rockets*, V. 16, July-Aug. 1979, pp. 264-267.
14. Beattie, J. R. et al., "Xenon Ion Propulsion Subsystem," AIAA Paper 85-2012, Sept.-Oct. 1985.
15. Hayashi, M., "Determination of Electron-Xenon Total Excitation Cross Sections, from Threshold to 100 eV, from Experimental Values of Townsend's α ," *Journal of Physics D: Applied Physics*, V. 16, 1983, pp. 581-589.
16. Rapp, D. and P. Englander-Golden, "Total Cross Sections for Ionization and Attachment in Gases by Electron Impact. I. Positive Ionization," *Journal of Chemical Physics*, V. 34, No. 5, 1965, pp. 1464-1479.
17. Bahdinsky, J., J. Roth and H. L. Bay, "An Analytical Formula and Important Parameters for Low-Energy Ion Sputtering," *J. Appl. Phys.*, V. 51, May 1980, pp. 2861-2865.
18. Rapp, D. and W. E. Francis, "Charge Exchange between Gaseous Ions and Atoms," *J. of Chem. Phys.*, V. 37, Dec. 1962, pp. 2631-2645.
19. Aston, G. and H. R. Kaufman, "Ion Beam Divergence Characteristics of Three-Grid Accelerator Systems," *AIAA Jour.*, V. 17, No. 1, Jan. 1979, pp. 64-70.
20. Brophy, J. R. and P. J. Wilbur, "Calculation of Plasma Properties in Ion Sources," *AIAA Jour.*, V. 24, No. 9, Sept. 1986, pp. 1516-1523.

Appendix C

A FOURIER SERIES TECHNIQUE FOR DIFFERENTIATING EXPERIMENTAL DATA

John R. Anderson

This paper develops a general procedure for applying Fourier series to obtain derivatives of experimental data. The mathematics described can be used in any application requiring differentiation of experimental data; however, Retarding Potential Analyzer (RPA) data will be used to demonstrate the usefulness of the technique.

In experimental work one often obtains discrete data pairs of the form $[\epsilon, I(\epsilon)]$ over some range $\epsilon = \epsilon_0$ to $\epsilon = \epsilon_0 + E$. For example, Retarding Potential Analyzer (RPA) data are collected in the form of a plot of positive ion current to a probe (I) as a function of retarding potential applied to the probe (ϵ). Numerically the value of applied retarding potential in volts is equal to the kinetic energy of the ions in eV, assuming singly-charged ions are collected and that ions have this kinetic energy at the reference potential (i.e. at 0 V). An example of a retarding potential analyzer trace, obtained by digitizing an X-Y plotter trace to obtain $[\epsilon, I(\epsilon)]$ data is shown in Fig. C1. The raw data for this RPA trace were obtained by measuring the ion current flowing through a hole of known area onto a current sensing plate as a function of the voltage applied to the plate. For RPA traces the ion energy distribution function is obtained from such data using

$$\frac{dn}{d\epsilon} = - \sqrt{\frac{m}{2\epsilon}} \frac{1}{eA} \left(\frac{dI}{d\epsilon} \right) \quad (C1)$$

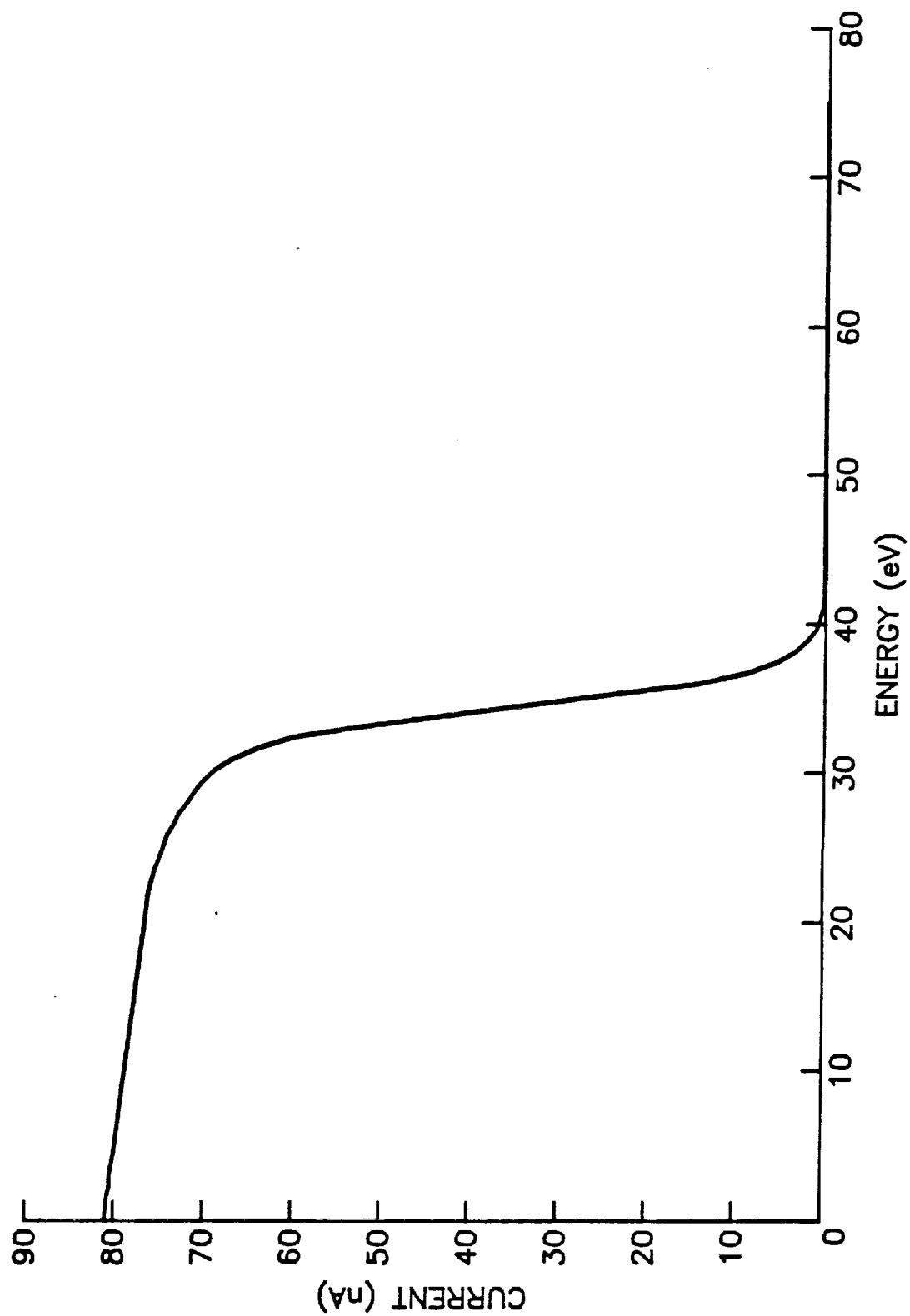


Fig. C1. Idealized Retarding Potential Analyzer Trace

where n is the ion number density (in m^{-3}), m is the ion mass (in kg), ϵ is the ion energy (in J), e is the electronic charge (in Coulombs) and A is the area (in m^2) through which current flows to the plate. Obviously, the function $I(\epsilon)$ must be differentiated to determine the energy distribution function. The method being proposed here to obtain this derivative, is to use a finite Fourier series to fit the original data and to then differentiate this series term by term. In order to ensure that this differentiated series converges, the Lanczos¹⁵ convergence factor should be used. Before discussing this factor, it is appropriate to discuss some of the drawbacks of Fourier series techniques. The Lanczos convergence factor will then be presented and an example demonstrating how this factor improves the convergence of Fourier series will be given.

The standard finite Fourier series representation of a function $I(\epsilon)$ on the open interval $(\epsilon_0, \epsilon_0 + E)$ is given by

$$I(\epsilon) = a_0 + \sum_{n=1}^N [a_n \cos(2\pi n\epsilon/E) + b_n \sin(2\pi n\epsilon/E)] \quad (C2)$$

where

$$a_0 = \frac{1}{E} \int_{\epsilon_0}^{\epsilon_0+E} I(\epsilon) d\epsilon, \quad (C3)$$

$$a_n = \frac{2}{E} \int_{\epsilon_0}^{\epsilon_0+E} I(\epsilon) \cos(2\pi n\epsilon/E) d\epsilon, \text{ and} \quad (C4)$$

$$b_n = \frac{2}{E} \int_{\epsilon_0}^{\epsilon_0+E} I(\epsilon) \sin(2\pi n\epsilon/E) d\epsilon. \quad (C5)$$

The Fourier series is periodic with period E and converges to $I(\epsilon)$ in the open interval $(\epsilon_0, \epsilon_0 + E)$, but the series converges to the average value $1/2[I(\epsilon_0) + I(\epsilon_0 + E)]$ at the interval endpoints ϵ_0 and $\epsilon_0 + E$. Therefore, unless $I(\epsilon_0) = I(\epsilon_0 + E)$, the Fourier series will not converge to $I(\epsilon)$ at the interval endpoints. If the Fourier series is discontinuous at any point including the interval endpoints, the Gibbs phenomenon is observed when a finite number of terms is used to approximate $I(\epsilon)$. The Gibbs phenomenon manifests itself as an overshoot of the finite Fourier series and this makes it difficult to estimate $I(\epsilon)$ near points of discontinuity. Another problem that arises if $I(\epsilon)$ has discontinuities, is that the derivative of the Fourier series does not converge. Because of these problems, the standard Fourier series has limited usefulness in many applications. These problems can however, be overcome by using the Lanczos convergence factor. The main idea behind this factor is to modify the standard Fourier series so that the derivative will converge by applying a finite difference operator D_N to the finite Fourier series. D_N is defined by

$$D_N F(\epsilon) = \frac{F(\epsilon + E/2N) - F(\epsilon - E/2N)}{E/N} \quad (C6)$$

From this definition it is seen that,

$$\lim_{N \rightarrow \infty} D_N F(\epsilon) = \frac{dF(\epsilon)}{d\epsilon} ; \quad (C7)$$

therefore,

$$\lim_{N \rightarrow \infty} D_N = \frac{d}{d\epsilon} \quad (C8)$$

Thus, it is seen that for large N , D_N provides a reasonable approximation of the derivative operator $\frac{d}{d\epsilon}$. Applying D_N to $I(\epsilon)$ gives

$$D_N I(\epsilon) = \frac{I(\epsilon + E/2N) - I(\epsilon - E/2N)}{E/N} \quad (C9a)$$

$$\begin{aligned} &= \frac{N}{E} \left\{ a_0 + \sum_{n=1}^N \left[a_n \cos((2\pi n/E)(\epsilon + E/2N)) \right. \right. \\ &\quad \left. \left. + b_n \sin((2\pi n/E)(\epsilon + E/2N)) \right] \right. \\ &\quad \left. - a_0 - \sum_{n=1}^N \left[a_n \cos((2\pi n/E)(\epsilon - E/2N)) \right. \right. \\ &\quad \left. \left. + b_n \sin((2\pi n/E)(\epsilon - E/2N)) \right] \right\} \quad (C9b) \end{aligned}$$

Using trigonometric identities and performing straight forward algebra, the following is obtained

$$\begin{aligned} D_N I(\epsilon) = \frac{d}{dx} \left\{ a_0 + \sum_{n=1}^N \frac{\sin(n\pi/N)}{(n\pi/N)} \left[a_n \cos(2\pi n\epsilon/E) \right. \right. \\ \left. \left. + b_n \sin(2\pi n\epsilon/E) \right] \right\} \quad (C10) \end{aligned}$$

From this it is evident that the finite Fourier series should be written as,

$$I(\epsilon) = a_0 + \sum_{n=1}^{N-1} \frac{\sin(n\pi/N)}{(n\pi/N)} [a_n \cos(2\pi n\epsilon/E) + b_n \sin(2\pi n\epsilon/E)]. \quad (C11)$$

Note that this series is summed from $n = 1$ to $N-1$ because $\sin(n\pi/N) = 0$ when $n = N$. The factor $\sin(n\pi/N)/(n\pi/N)$ is called the Lanczos convergence factor; it causes the finite Fourier series to converge to $I(\epsilon)$ faster because it attenuates the high frequency terms which cause the Gibbs phenomenon. Consequently, the derivative of $I(\epsilon)$ will converge even if $I(\epsilon)$ is discontinuous at any point including the end points $I(\epsilon_0)$ and $I(\epsilon_0 + E)$. (However, in general, the derivative will not converge to the correct value at the interval end points because of the discontinuity introduced by the Fourier series.) The derivative of $I(\epsilon)$ will converge, if the first power of the Lanczos convergence factor is inserted into the standard Fourier series before differentiation; however, better convergence is achieved if the square of this factor is inserted before differentiation. In general, the best convergence is achieved if the Lanczos convergence factor is raised to the $m+1$ power before the m^{th} derivative of the Fourier series is taken.

Although many of the convergence problems of Fourier series are ameliorated by using the Lanczos convergence factor, convergence problems can still be encountered near the interval end points when $I(\epsilon_0) \neq I(\epsilon_0 + E)$; therefore, as a general rule, data should be taken so that the region of interest is in the middle 90% of the interval $(\epsilon_0, \epsilon_0 + E)$.

When the technique is to be applied to experimental data, Fourier coefficients must be computed and this can be accomplished using the integral expressions for the coefficients given in Eqs. C3, C4 and C5.

Any standard numerical integration technique, such as the trapezoidal rule or Simpson's rule, can be used to do this; various integration techniques have been tried on RPA data and the best results were obtained using Simpson's rule when all of the data were spaced evenly on ϵ .

A further practical concern is the number of Fourier coefficients needed to achieve a reasonable approximation to the function $I(\epsilon)$. For RPA data, the first 50 Fourier series terms gives satisfactory results. Other applications may require more terms; however, this consideration is left to the discretion of the reader. The minimum number of data points needed to compute N Fourier coefficients is dictated by the digitizing theorem, which states that the sampling frequency must be at least twice as high as the highest frequency to be measured. This means that at least $2N$ data points are needed (assuming the data are all evenly spaced) to compute the first N Fourier coefficients. If Simpson's rule is used to compute the first 50 Fourier coefficients, at least 101 data points are required because Simpson's rule requires using an odd number of data points.

Now that the pertinent mathematics has been discussed, an example illustrating the improved convergence achieved by using the Lanczos convergence factor will be given. Figure C1 shows an experimentally obtained RPA trace. Figure C2 shows the standard (no Lanczos convergence factor used) Fourier series approximation to $I(\epsilon)$ using the first 25 Fourier series terms. Note that the Fourier series converges to the average value of the function at the interval end points and there is evidence of the Gibbs phenomenon. Figure C3 shows the same Fourier series used in Fig. C2, except that the first 50 terms were used and the Lanczos convergence factor has been applied.

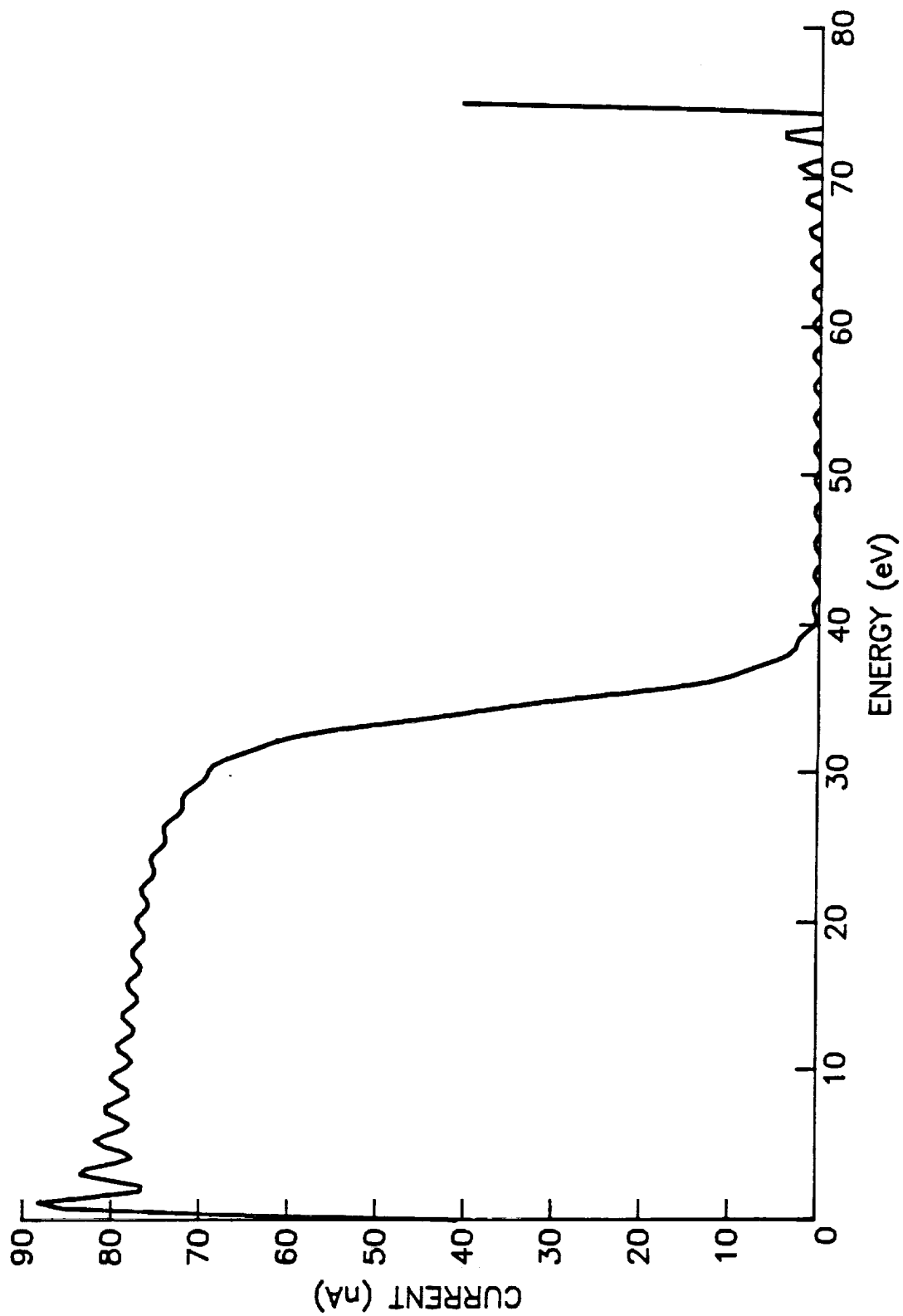


Fig. C2. Standard Fourier Series Approximation of RPA Trace with No Convergence Factor

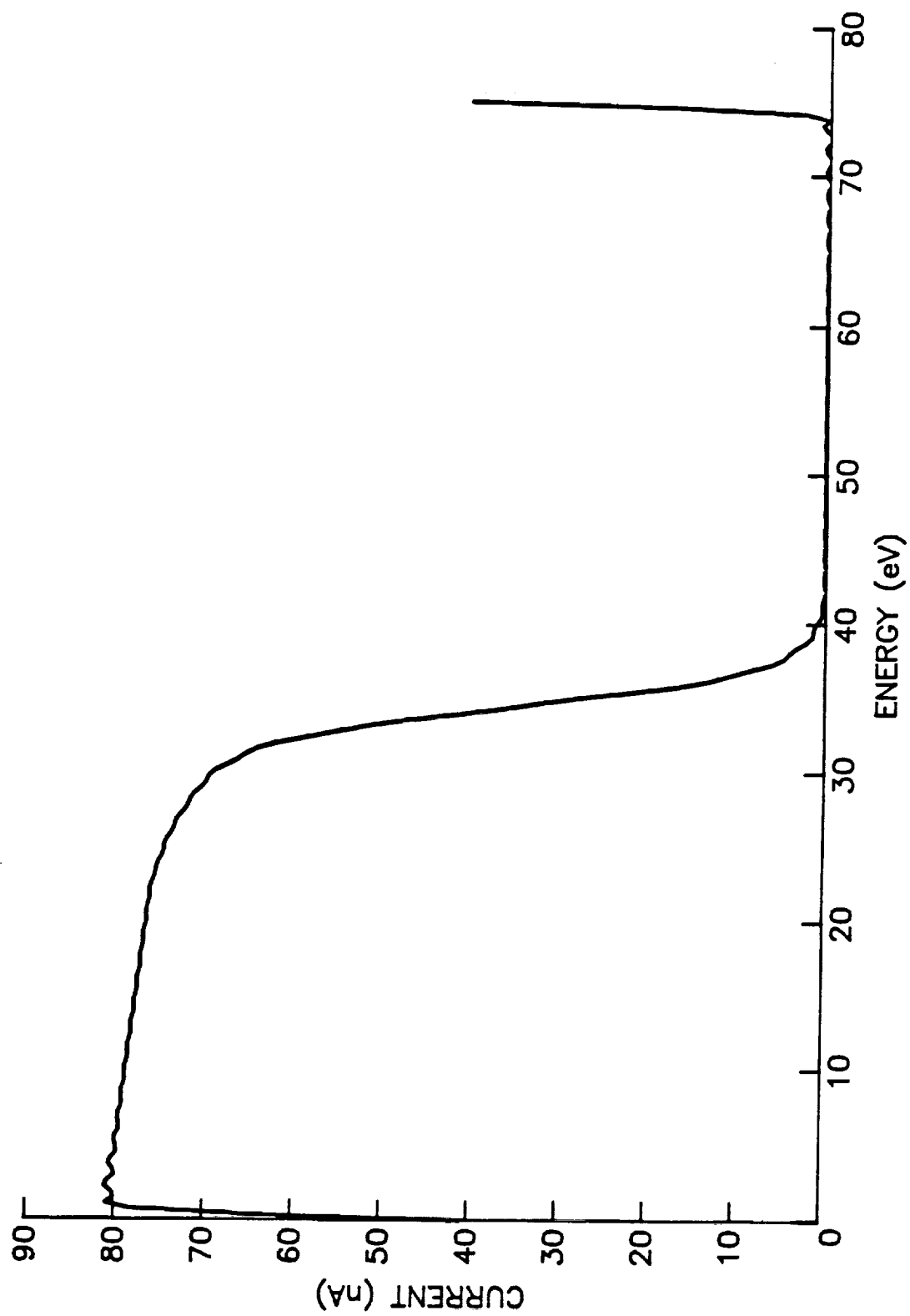


Fig. C3. Fourier Series Approximation of RPA Trace with Lanczos Convergence Factor

If the first 50 terms had been used in Fig. C2, the curve would have been even noisier because of numerical errors encountered when estimating the high frequency Fourier coefficients. The Lanczos convergence factor damps the high frequency Fourier terms; therefore, errors in estimating the high frequency coefficients do not significantly affect the results. Again, in Fig. C3, the Fourier series converges to the average value at the interval end points; however, evidence of the Gibbs phenomenon has almost disappeared. Figures C4, C5 and C6 show, respectively, the energy distributions given by Eq. C1, when no convergence factor, the first power of the Lanczos factor, and the square of the Lanczos factor, are used before differentiating. The first 25 Fourier terms are used in Figs. C4 and C5, and 50 Fourier terms are used in Fig. C6. From these figures it is evident that reasonable results are only obtained when the square of the Lanczos convergence factor is inserted before taking the first derivative. It is also noted that the derivative is large near the interval end points due to the discontinuity in the Fourier series representation of $I(\epsilon)$; the derivative has not been drawn to the interval end points so this is not seen.

From this example it is evident that the standard Fourier series is not a useful tool for analyzing experimental data; however, use of the Fourier series in conjunction with the correctly applied Lanczos convergence factor does provide a useful technique for analyzing such data.

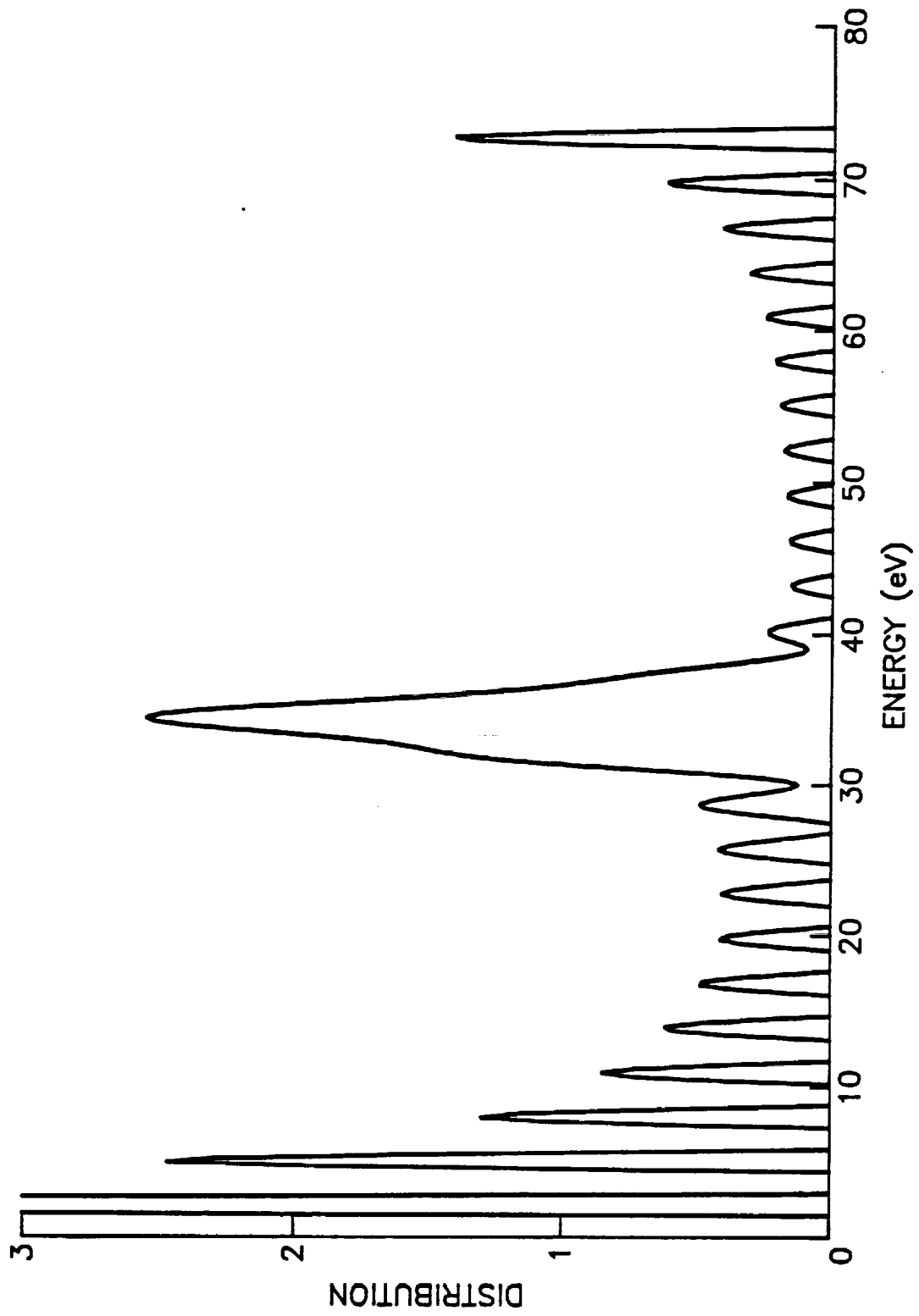


Fig. C4. Fourier Series Representation of Beam Ion Energy Distribution with No Convergence Factor

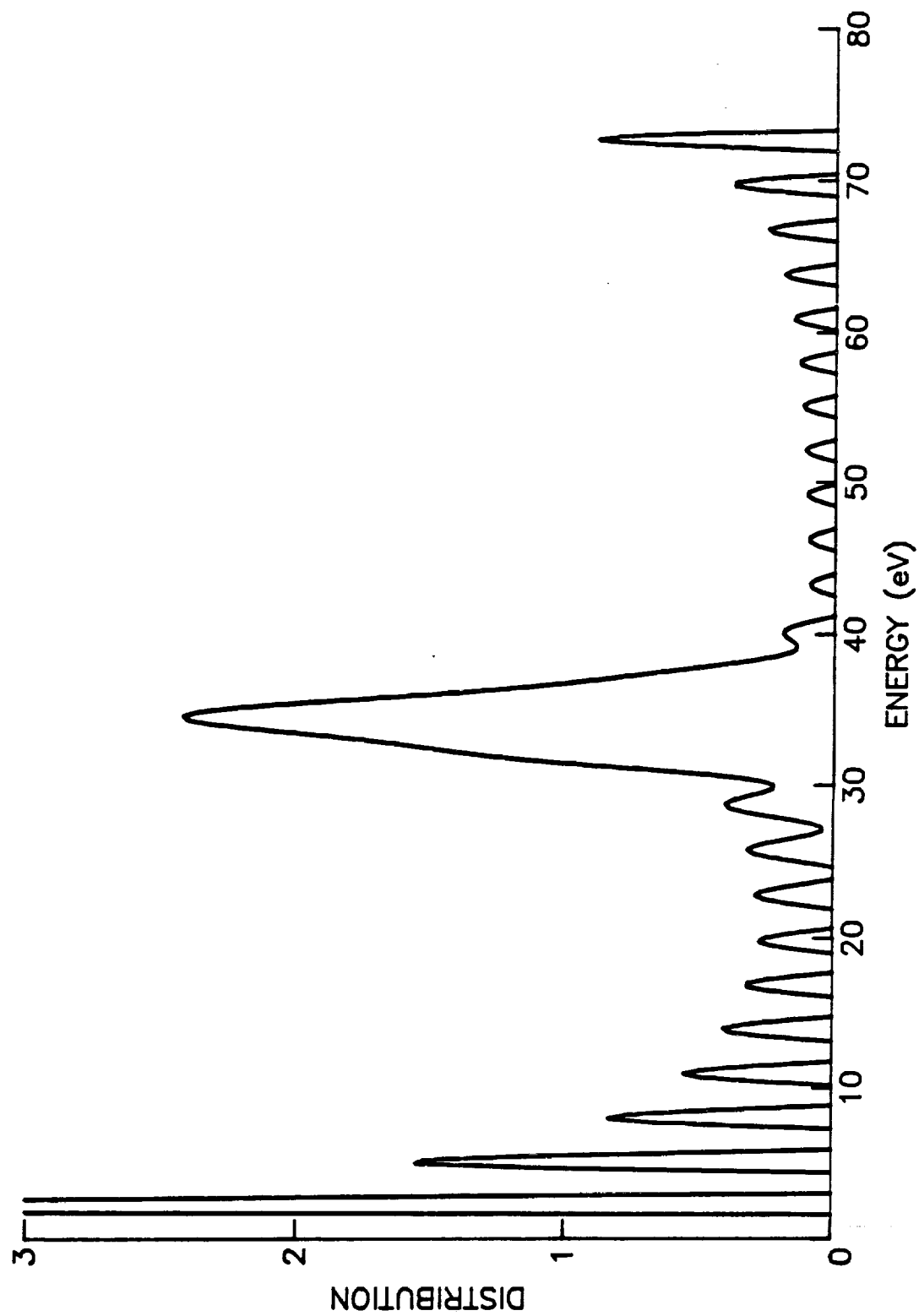


Fig. C5. Fourier Series Representation of Beam Ion Energy Distribution
Using First Power of Lanczos Convergence Factor

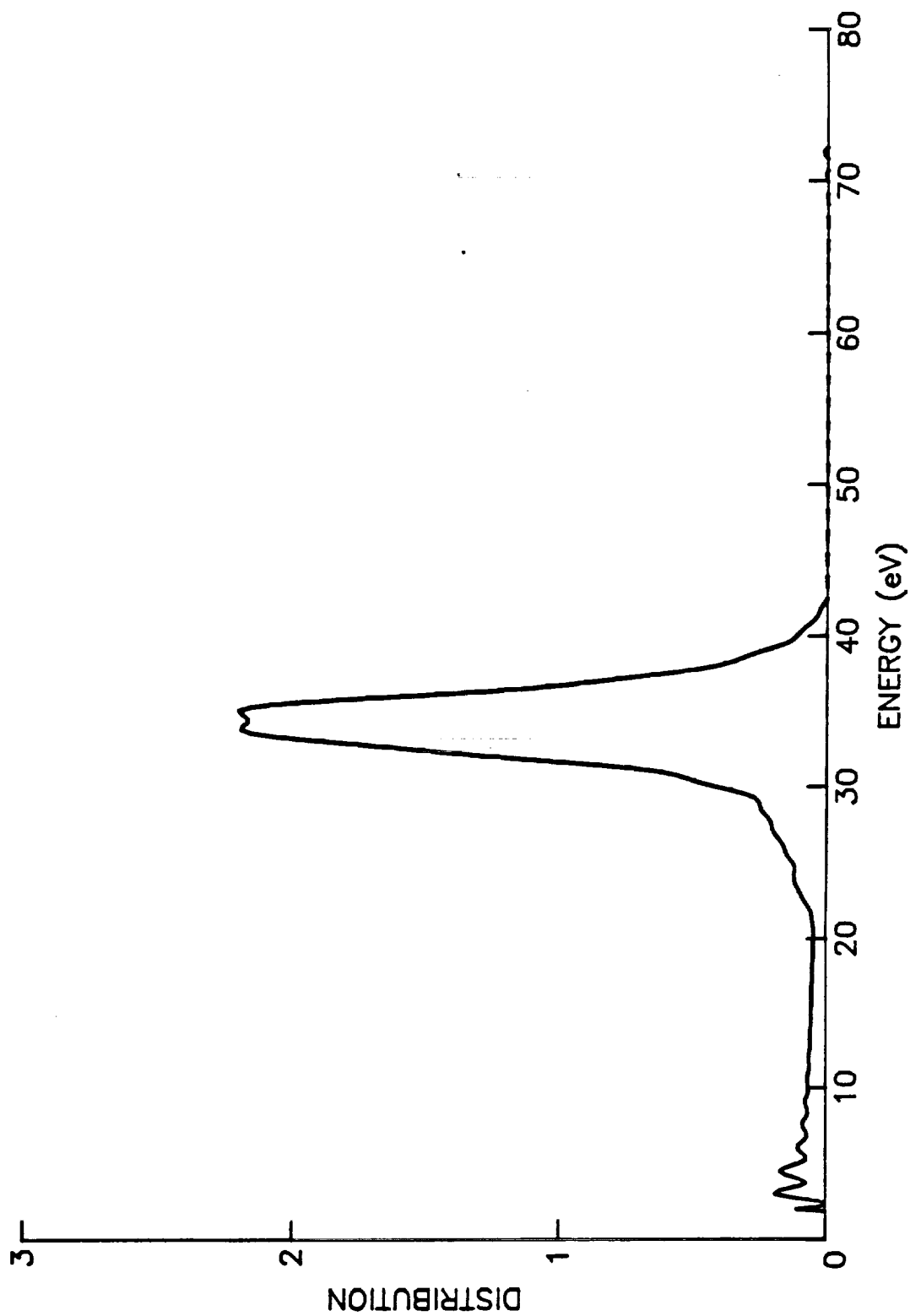


Fig. C6. Fourier Series Representation of Beam Ion Energy Distribution Using the Square of the Lanczos Convergence Factor

DISTRIBUTION LIST

Copies

National Aeronautics and Space Administration
Washington, DC 20546

Attn:

RP/Mr. Earl E. VanLaningham, MS B600

1

National Aeronautics and Space Administration
Lewis Research Center
21000 Brookpark Road
Cleveland, OH 44135

Attn:

Technology Utilization Office, MS 7-3

1

Report Control Office, MS 60-1

1

Library, MS 60-3

2

Dr. M. Goldstein, Chief Scientist, MS 5-9

1

Mr. Dave Byers, MS 500-219

1

Mr. Jim Stone, MS 500-219

1

Mr. Vincent Rawlin, MS 500-220

10

Mr. Bruce Banks, MS 302-1

1

Mr. Michael Patterson, MS 500-220

1

Mr. Tim Verhey, MS 500-220

1

National Aeronautics and Space Administration
Lyndon B. Johnson Space Center
Houston, TX 77058

Attn:

Dr. James E. McCoy, Mail Code SN3

1

National Aeronautics and Space Administration
Marshall Space Flight Center
Huntsville, AL 35812

Attn:

Mr. Ralph Carruth, Mail Code ES 53

1

Mr. Jason Vaughn, Mail Code ES 53

1

NASA Scientific and Technical
Information Facility
P.O. Box 8757
Baltimore, MD 21240

Attn:

Accessioning Dept.

1

Dept. of the Navy
Office of Naval Research
University of New Mexico
Bandolier Hall West
Albuquerque, NM 87131

Attn:

G. Max Irving

1

Copies

Case Western Reserve University
10900 Euclid Avenue
Cleveland, OH 44106
Attn:

Dr. Eli Reshotko

1

Procurement Executive, Ministry of Defense
Royal Aircraft Establishment
Farnborough, Hants GU14 6TD
ENGLAND
Attn:

Dr. D. G. Fearn

1

United Kingdom Atomic Energy Authority
Culham Laboratory
Abingdon, Oxfordshire OX143DB
ENGLAND
Attn:

Dr. A. R. Martin (Rm F4/135)

1

Intelsat
3400 International Dr. N.W.
Washington D.C. 20008-3098
Attn:

Dr. John Stevenson, MS 33

1

Air Force Astronautics Lab
Edwards AFB, CA 93523
Attn:

LKDH/Lt. Robert D. Meya, MS 24

1

LKDH/Lt. Phil Roberts, MS 24

1

Giessen University
1st Institute of Physics
Giessen, West Germany
Attn:

Professor H. W. Loeb

1

Jet Propulsion Laboratory
4800 Oak Grove Laboratory
Pasadena, CA 91109
Attn:

Technical Library

1

Mr. James Graf

1

Dr. Dave King, MS 125-224

1

Dr. Charles Garner, MS 125-224

1

TRW Inc.
TRW Systems
One Space Park
Redondo Beach, CA 90278
Attn:

Mr. Sid Zafran

1

Copies

National Aeronautics and Space Administration
Ames Research Center
Moffett Field, CA 94035

Attn:

Technical Library

1

National Aeronautics and Space Administration
Langley Research Center
Langley Field Station
Hampton, VA 23365

Attn:

Technical Library

1

Hughes Research Laboratories
3011 Malibu Canyon Road
Malibu, CA 90265

Attn:

Mr. J. H. Molitor

1

Dr. Jay Hyman, MS RL 57

1

Dr. J. R. Beattie, MS RL 57

1

Dr. J. N. Matossian, MS RL 57

1

Engineering Quadrangle
Princeton University
Princeton, NJ 08540

Attn:

Prof R. G. Jahn

1

Dr. Arnold Kelly

1

Boeing Aerospace Co.
P. O. Box 3999
Seattle, WA 98124-2499

Attn:

Mr. Donald Grim, MS 8K31

1

Lockheed Missiles and Space Co.
Sunnyvale, CA 94088

Attn:

Dr. William L. Owens, Dept. 57-24

1

Rocket Research Co.
P.O. Box 97009
Redmond, WA 98073-9709

Attn:

Mr. William W. Smith

1

Mr. Paul Lichon

1

Electrotechnical Laboratory
1-1-4, Umezono, Tsukuba-Shi
Ibaraki, 305 JAPAN

Attn:

Dr. Isao Kudo

1

Copies

Sandia Laboratories
P. O. Box 5800
Albuquerque, NM 87185

Attn:

Mr. Ralph R. Peters, Mail Code 4537

1

Mr. Dean Rovang, Mail Code 1251

1

Ion Tech Inc.
2330 E. Prospect Road
Fort Collins, CO 80525

Attn:

Dr. Gerald C. Isaacson

1

Dr. Dan Siegfried

1

Mr. Larry Daniels

1

EG & G Idaho
P. O. Box 1625
Idaho Falls, ID 83401

Attn:

Dr. G. R. Longhurst, TSA-104

1

Michigan State University
East Lansing, MI 48824

Attn:

Dr. J. Asmussen

1

Dr. M.C. Hawley

1

Aerospace Engineering Department
Faculty of Engineering
Tokai University
Kitakanome, Hiratsuka-shi,
Kanagawa-ken, JAPAN 259

Attn:

Prof. Itsuro Kimura

1

Department of Electronics
Tokyo National Technical College
No. 1220-2
Kunugida-cha, Hachioji 193
Tokyo, JAPAN

Attn:

Mr. Susumu Masaki

1

Tuskegee Institute
School of Engineering
Tuskegee Institute, AL 36088

Attn:

Dr. Pradosh Ray

1

Mr. Lee Parker
252 Lexington Road
Concord, MA 01741

1

Copies

Physics Department
Naval Postgraduate School
Monterey, CA 93943-5000

Attn:

Dr. Chris Olson, Mail Code 61-0S

1

Martin Marietta Aerospace
P. O. Box 179
Denver, CO 80201

Attn:

Dr. Kevin Rudolph, MS M0482

1

S-Cubed
P. O. Box 1620
LaJolla, CA 92038

Attn:

Dr. Ira Katz

1

G-T Devices, Inc.
5705 A General Washington Dr.
Alexandria, VA 22312

Attn:

Dr. Rodney Burton

1

Instituto de Pesquisas Espaciais - INPE
Library and Documentation Division
C.P. 515
Sao Jose dos Campos - SP
12200 - BRAZIL

1

Teletronix Inc.
P.O. Box 500
Beaverton, OR 97077

Attn:

Mr. Curtis Haynes, MS 50-324

1

Dr. Robert Vondra
P.O. Box 596
Wrightwood, CA 92397

1

Electric Propulsion Laboratory, Inc.
43423 N. Division St., Suite 205
Lancaster, CA 93535

Attn:

Dr. Graeme Aston

1

Dr. John R. Brophy

1

Department of Aeronautics
University of Tokyo
7-3-1 Hongo, Bunko-ku
Tokyo 113, Japan

Attn:

Prof. Yoshihiro Arakawa

1

-

-

-

-

